2005-11-21

MPSA Effects on Copper Electrodeposition: Understanding Molecular Behavior at the Electrochemical Interface

Clint Gordon Guymon
Brigham Young University - Provo

MPSA EFFECTS ON COPPER ELECTRODEPOSITION: UNDERSTANDING MOLECULAR BEHAVIOR AT THE ELECTROCHEMICAL INTERFACE

by

Clint Guymon

A dissertation submitted to the faculty of

Brigham Young University

in partial fulfillment of the requirements for the degree of

Doctor of Philosophy

Department of Chemical Engineering

Brigham Young University

April 2006

BRIGHAM YOUNG UNIVERSITY

GRADUATE COMMITTEE APPROVAL

of a dissertation submitted by

Clint Guymon

This dissertation has been read by each member of the following graduate committee and by majority vote has been found to be satisfactory.

Date	Dean R. Wheeler, Chair
Date	Richard L. Rowley
Date	John N. Harb
Date	Ronald E. Terry
Date	William G. Pitt

BRIGHAM YOUNG UNIVERSITY

As chair of the candidate's graduate committee, I have read the dissertation of Clint Guymon in its final form and have found that (1) its format, citations, and bibliographical style are consistent and acceptable and fulfill university and department style requirements; (2) its illustrative materials including figures, tables, and charts are in place; and (3) the final manuscript is satisfactory to the graduate committee and is ready for submission to the university library.

Date

Dean R. Wheeler
Chair, Graduate Committee

Accepted for the Department

William G. Pitt
Graduate Coordinator

Accepted for the College

Alan R. Parkinson
Dean, Ira A. Fulton College of Engineering and Technology

ABSTRACT

MPSA EFFECTS ON COPPER ELECTRODEPOSITION:

UNDERSTANDING MOLECULAR BEHAVIOR AT

THE ELECTROCHEMICAL INTERFACE

Clint Guymon

Department of Chemical Engineering

Doctor of Philosophy

In this work the structure of the electrochemical metal-liquid interface is determined through use of quantum mechanics, molecular simulation, and experiment. Herein are profiled the molecular dynamics details and results of solid-liquid interfaces at flat non-specific solid surfaces and copper metal electrodes. *Ab initio* quantum-mechanical calculations are reported and define the interatomic potentials in the simulations. Some of the quantum-mechanical calculations involve small copper clusters interacting with 3-mercaptopropanesulfonic acid (MPSA), sodium, chloride, bisulfate and cuprous ions. In connection with these I develop the electrode charge dynamics (ECD) routine to treat the charge mobility in a metal. ECD bridges the gap between small-scale metal-cluster *ab initio* calculations and large-scale simulations of metal surfaces of arbitrary geometry.

As water is the most abundant surface species in aqueous systems, water determines much of the interfacial dynamics. In contrast to prior simulation work,

simulations in this work show the presence of a dense 2D ice-like rhombus structure of water on the surface that is relatively impervious to perturbation by typical electrode charges. I also find that chloride ions are adsorbed at both positive and negative electrode potentials, in agreement with experimental findings. Including internal modes of vibration in the water model enhances the ion contact adsorption at the solid surface.

In superconformal filling of copper chip interconnects, organic additives are used to bottom-up fill high-aspect ratio trenches or vias. I use molecular dynamics and rotating-disk-electrode experiments to provide insight into the function of MPSA, one such additive. It is concluded that the thiol head group of MPSA inhibits copper deposition by preferentially occupying the active surface sites. The sulfonate head group participates in binding the copper ions and facilitating their transfer to the surface. Chloride ions reduce the work function of the copper electrode, reduce the binding energy of MPSA to the copper surface, and attenuate the binding of copper ions to the sulfonate head group of MPSA.

ACKNOWLEDGMENTS

I acknowledge the sustenance, mercy, longsuffering, and goodness of God. I acknowledge those same divine qualities that my dear bride, Nanci, has exuded in our enriching stay here at Brigham Young University. I'm grateful for the support of my immediate and extended family. I'm also grateful for Dr. Richard Rowley who mentored me as I began my studies. Dr. Wheeler has helped me be a better writer and researcher for which I am very grateful. The associations I've had while at BYU have bolstered my belief in humanity and heightened my awareness of the burden and opportunity I bear to "go forth and serve."

I am and will be grateful for the untold and intangible consequences that will flow to my family and I as a recipient of a doctorate degree from Brigham Young University.

This work was supported by a grant from the National Science Foundation (No. CTS-0215786), by donors to the Petroleum Research Fund, and by Brigham Young University.

Contents

Acknowledgments **vii**

List of Tables **xiii**

List of Figures **xvii**

List of Symbols **xx**

1 Introduction **1**
1.1 Modeling an Electrochemical Interface 2
1.2 Molecular Dynamics Approach 6
1.3 Scope of Work 7

2 Molecular Models of the Aqueous Species **11**
2.1 Introduction 11
2.2 Molecular Dynamics Introduction 11
2.2.1 Molecular Interactions 12
2.2.2 Pair-wise Additivity 12
2.2.3 Combining Rules 14
2.2.4 Simulation of Slab Geometries Using the Ewald Sum 15
2.3 Interaction Potentials for Species in Solution 16
2.3.1 H_2O, Na^+, Cl^-, Cu^+, and Cu^{2+} Models 19
2.3.2 $MPSA^-$ Model 20
2.3.3 TPT and $SSPSS^{2-}$ Models 26
2.3.4 Divalent Sulfate Ion Model 28
2.3.5 Bisulfate Ion Model 29
2.3.6 Summary 33

3 Solvent Vibrational Mode Effects **39**
3.1 Introduction 39
3.2 Simulation Specifics 41
3.3 Results and Discussion 43
3.3.1 Bulk Property Comparisons for the Three Models 43
3.3.2 Ion Hydration Results in the Absence of a Solid-Liquid Interface 44
3.3.3 Ion Hydration in Proximity to the Solid Surface 48

3.3.4 Electrical Properties of the Double Layer 52
3.4 Conclusions 60

4 An Electrode Charge Dynamics Routine 63
4.1 Introduction 63
4.2 Methodology 66
4.2.1 ECD and the Ewald Sum 71
4.3 ECD Parameter Fit to Cu_{10} *Ab Initio* Data 73
4.4 Conclusion 78

5 ECD Validation, Predictions, and Interfacial Simulations 79
5.1 Introduction 79
5.2 ECD Validation 80
5.2.1 ECD and Image Charges 80
5.2.2 Cluster-Size Results with ECD 81
5.2.3 ECD and *Ab Initio* Results for Hydrated Na^+ Clusters Near Cu 82
5.3 ECD Predictions 84
5.3.1 ECD Large-Cluster Predictions 85
5.3.2 MD Simulation Details and Results 89
5.4 Conclusion 98

6 Simulated $MPSA^-$ Behavior Near a Copper Surface 101
6.1 Introduction 101
6.2 Simulated Species Adsorption at a Copper Surface 103
6.2.1 Additional Surface-Interaction Potentials 105
6.2.2 Simulation Details 112
6.3 Simulation Results 115
6.3.1 Ionic and Water Profiles and Potential of Mean Force 115
6.3.2 Adsorption and Desorption Energies 122
6.3.3 Simulated Electrode Work Function 132
6.3.4 Copper-Ion Distributions about MPSA 135
6.4 Conclusions 137

7 Chronoamperometry Studies of MPSA, SSPSS, and TPT 141
7.1 Introduction 141
7.2 Review of Copper Deposition in the Presence of Thiols 142
7.3 Experimental RDE Study 144
7.3.1 Experimental Details 144
7.3.2 Chronoamperometry Results 145
7.4 Conclusions 147

8 Summary **149**
8.1 Molecular Models Summary 149
8.2 Simulation Summary 150
8.3 Mechanism of MPSA Inhibition and Acceleration 151
8.4 Summary and Future Prospects 153

Bibliography **157**

A Example Ewald Calculation **173**

List of Tables

2.1 Lennard-Jones parameters and charges for each of the monatomic ions in the simulated solution 20
2.2 $MPSA^-$ dihedral potential parameters around the bonds indicated in Figure 2.2, in units of K. 26
2.3 Charge and model coordinates for the simulated organic additives: $MPSA^-$, TPT, and $SSPSS^{2-}$ 27
2.4 Charge and model coordinates for the bisulfate ion. The charges and model geometry were found in the same way as previous models. . . . 33
2.5 Solution Lennard-Jones parameters of organic species. 34
3.1 Molecular models of water 42
3.2 Comparison of bulk properties obtained from SPC/E and various models of water that include flexibility. 45
3.3 Electric field at the center of the cell for the unpolarizable surface simulations. 60
4.1 Interaction parameters with Cu metal 75
6.1 Additional modified-Morse Cu-metal interaction parameters 112
6.2 Adsorption energies of thiol or sulfonate sites 124
6.3 Proposed surface function of sodium chloride, thiol, and sulfonate in an electrodeposition bath. 138

List of Figures

1.1 Depiction of the relative length and time scales of several modeling techniques 4
2.1 2-D slab geometry representation of a single particle system. 15
2.2 Pictorial representation of $MPSA^-$. 21
2.3 *Ab initio* potential scans of MPSA for water and sodium. 23
2.4 *Ab initio* potential scans of MPSA for chloride and cuprous ion. . . . 24
2.5 *Ab initio* and model potential energy scans of the divalent sulfate ion. 30
2.6 *Ab initio* and model potential energy of bisulfate-bisulfate scans. . . . 31
2.7 *Ab initio* and model potential energy of water-bisulfate scans. 32
3.1 Ion-O radial distribution functions for a (a) cation and (b) anion using the SPC/E, SPC/E-F, and SPC/E-Fd models. 46
3.2 Ion-H radial distribution functions for a (a) cation and (b) anion using the SPC/E, SPC/E-F, and SPC/E-Fd models. 47
3.3 1 M Ion density profiles for ions of same size. 49
3.4 0.5 M Ion density profiles for ions of same size. 51
3.5 SPC/E water dipole orientation surface at a surface charge of 0.0 C/m^2 and 0 M ions. 53
3.6 SPC/E water dipole orientation surface at a surface charge of ± 0.1 C/m^2 and 0 M ions. 54
3.7 SPC/E water dipole orientation surface at a surface charge of ± 0.1 C/m^2 and 1 M ions. 55
3.8 Average electric field deviations from the uniformly charged plate value. 57
3.9 Potential drop profile for SPC/E water with ions at an unpolarizable surface 58
3.10 Half-cell potential drop as a function of surface charge for 0.5 and 1 M ion concentrations as obtained from the SPC/E-F model. 59
4.1 Representation of a fictitious image charge in a metal 64
4.2 Charge on each metal atom 66
4.3 Graphic of the splitting of diffuse-charge interactions in the electrode into real and reciprocal space portions. 71
4.4 ECD and *ab initio* potential energy as a function of distance from the Cu_{10} (111) plane for Cl^-. 76
4.5 Interaction energy of several water approaches toward a 10 atom copper cluster. 77

5.1 Comparison of ECD with image-charge method for a spherical copper cluster of effective radius $a = 7.27$ Å. 82
5.2 Interaction energy of water (hydrogens up), chloride, and sodium ion approaching the on-top site of a Cu_{18} cluster. 83
5.3 MP2 *ab initio* and ECD energies of a hydrated Na^+ atom near copper clusters. 85
5.4 Interaction energy of chloride and sodium ion with copper clusters of differing size. 86
5.5 Interaction energy of water with copper clusters for water approaching the *top site*. 87
5.6 Interaction energy of water with copper clusters for water approaching the *bridge site*. 88
5.7 Interaction energy of water with copper clusters for water approaching the *hollow site*. 89
5.8 3D representation of simulation cell. 90
5.9 Average charge on the copper layers with layer 1 and 10 being the layers exposed to the respective solutions. 92
5.10 Average species density profiles for (a) water sites and (b) ions versus cell position for zero potential difference between the electrodes. . . . 93
5.11 Probability of the cosine of the angle between the surface normal and the surface adsorbed (within 3.5 Å of the surface) water dipole moment. 94
5.12 Snapshot of the first two water layers on the copper surface for a simulation of neat water. 95
5.13 Snapshot of the water orientation on the copper surface with ions present. 96
5.14 Electrostatic potential in the fluid for NaCl solution and water only. . 97
6.1 Drawings representing trench cross-sections after deposition of copper. 102
6.2 Potential energy and representation of bisulfate ion approaching a Cu_{10} cluster. 107
6.3 Potential energy and representation of sulfate ion approaching a Cu_{10} cluster. 108
6.4 Potential energy and representations of $MPSA^-$ and derivatives approaching a Cu_{10} cluster. 110
6.5 Potential energy of cuprous ion approaching a Cu_{10} cluster 111
6.6 3D representation of simulation cell with sawtooth surface. 113
6.7 Density of water and ions near charged Cu(111) surfaces. 117
6.8 Electrostatic potential profile and electric-field gradient profile of the system with charged copper surfaces 119
6.9 Potential of mean force and integrated mean force of water at a flat copper (111) surface in the presence of sodium, chloride, copper, and bisulfate ions. 123
6.10 Representative integrated mean force profiles of organic adsorption/desorption events. 126
6.11 Snapshot of $MPSA^-$ near the sawtooth copper surface 128
6.12 Integrated-mean-force raw data for water, ions and two organic adsorption and desorption events. 131

6.13 Electrostatic potential of the negative electrode relative to the SSE reference when the metal interface is perturbed 133
6.14 Copper-ion distribution about the sulfonate and thiol head groups of MPSA 136
7.1 Electrostatic potential variations when 1 ppm MPSA, SSPSS, or TPT are added followed by 50 ppm NaCl addition to the electrolyte 146
8.1 Pictorial summary of the simulation and experimental conclusions . . 152

List of Symbols

Greek Nomenclature

α	Ewald convergence parameter
ϵ	Lennard-Jones or modified Morse parameter or dielectric constant
ϵ_0	Permittivity of free space
γ	Inverse charge width parameter
λ	Undetermined multiplier
μ	Undetermined multiplier and molecular dipole moment
ϕ	Electrostatic potential
ρ	Mass, number, or charge density
σ	Lennard-Jones size parameter
θ	Dihedral angle
τ	Time constant
ξ	Proportional feedback control parameter
ζ	Integral feedback control parameter

Roman Nomenclature

A	Dihedral potential parameter or modified-Morse parameter
C	Coulomb overlap integrals
D	Diffusion coefficient
E	Electric field
F	Force
$\mathcal{F}$	Faradays constant
G	Optimal influence function
$\mathcal{L}$	Lagrangian
Q	Total charge or stiffness parameter
R	Universal gas constant
T	System or charge temperature
U	Energy, kJ/mol
W	Charge assignment function or potential of mean force
a	Lattice parameter or sphere radius
e	Elementary charge
h	Mesh-point spacing

i	Electric current
k	Harmonic potential constants
k_B	Boltzmann's constant
k_F	Fermi wave vector
m	Site mass
n	Number of particles or electrons
q	Charge density at electrode surface or site charge
q_i^c	Core point charge on metal site i
q_i^v	Diffuse valence charge on metal site i
r	Radial distance
r^*	Modified-Morse parameter
v	Velocity
x, y	Cartesian coordinates
z	Cartesian coordinate or site charge
$<$	Angle, radians

Chapter 1

Introduction

An electrochemical interface exists at the phase boundary between a metal and a liquid. The dynamics and structure of such a ubiquitous interface are important in the field of metal electrodeposition for example. Friedel oscillations in the charge density in the metal near the surface and oscillations in the liquid species densities influence the transfer of electrons or chemical species to and from the interface [1]. Additionally, the interaction between the metal and solution charges determines the interfacial structure of the solution species. Knowledge of the dynamics and structure of the electrochemical interface could facilitate the manipulation of chemical deposition and dissolution processes or guide the development of new electrochemical devices.

A complete understanding of interfacial dynamics and structure would direct the *a priori* solution of electrodeposition or corrosion problems. Questions such as "How do I decrease the number of grain boundaries formed during electrodeposition?" or "How can I manipulate the interface to force the deposition or dissolution of a metal at a specific location?" could more readily be addressed due to an indepth understanding of the behavior of the complex solid-liquid interface. Often it isn't known how multiple chemicals interact and influence electron transfer, and so of necessity, problems are solved empirically or with limited understanding so that the 'whys' or 'why nots' of system behavior aren't fully known. For example, in the semiconductor industry,

copper metal deposits have been improved by inclusion of organic additives to modify the electrochemical double layer during electrodeposition [2]. Exactly how the organic additive causes the deposition rate to be accelerated isn't completely understood.

The objective of this work is to provide additional insight into the structure of the electrochemical interface between a metal surface and an aqueous solution. The species of greatest influence at an aqueous liquid-metal interface is water as it is the most abundant surface species. In this work, I give the structure of water at the interface and detail how changes in the chemical makeup of the solution adjacent to the solid influence various interfacial properties.

An additional objective of this work is to determine the function of 3-mercaptopropane sulfonic acid (MPSA) in facilitating the deposition of copper in high-aspect ratio chip interconnects. The adsorption strength of MPSA at the surface as well as the influence of sodium chloride on that adsorption are given. The molecular dynamics results showing the behavior of MPSA at the interface are augmented with experimental chronoamperometry results at a rotating disk electrode. In this way I provide insight and understanding that can be used to guide the manipulation of interfacial behavior in electrodeposition of copper and other applications.

In this introductory chapter, I briefly examine the electrochemical interface. A brief background of the molecular dynamics technique is also discussed with a more indepth treatment in Chap. 2. A discussion of the structure and scope of the remaining chapters concludes this introduction.

1.1 Modeling an Electrochemical Interface

The behavior of molecules at the electrochemical interface is dominated by the interactions between the electrons in the system. Electrons Coulombically interact with other electrons. At short range, the electrons in a molecular orbital can correlate with

electrons in adjacent orbitals resulting in attraction. At very small molecular separation distances, the molecules are repelled (termed Pauli repulsion) due to Coulombic repulsion and the Pauli exclusion principle. These two principles, electron correlation and Pauli repulsion (collectively referred to as van-der-Waals interactions), govern the phase transition from gas to liquid in non-polar, non-charged media like argon. In polar or charged media, like an aqueous electrolyte, there are also long-range charge-charge interactions between two ions for example.

When a molecule approaches a metal surface, the electrons in the conduction band can adjust to the approaching charge distribution so as to equilibrate the chemical potential of electrons in the metal. This adjustment of charge at the metal surface, results in an additional attraction to the surface over and above the attraction from electron correlation between the surface atoms and the molecule. At distances very near the surface, Pauli repulsion dominates the surface-molecule interaction.

The distribution of ions, water, and other molecules near the solid-liquid interface is determined by the interactions in solution and by the interactions of the solution with the metal surface. For instance, in an aqueous solution, those ions that are hydrated well may not be abundant at the surface as surface adsorption requires the shedding of the ion's hydration shell. The structure of the interface, as determined by the interatomic interactions, gives rise to a charge distribution in the solution and in the metal. This interfacial layer is often referred to as a double layer.

There are several levels of modeling double-layer structure and dynamics. All are motivated by the desire to fundamentally understand the important factors affecting system performance so as to manipulate such performance. Shown in Figure 1.1 is a depiction of the relative length and time scales of several modeling techniques. Smaller scale techniques include quantum-mechanically based molecular mechanics and Car-Parinello molecular dynamics. Larger scale techniques include microscopic methods like dissipative particle dynamics and macroscopic numerical models.

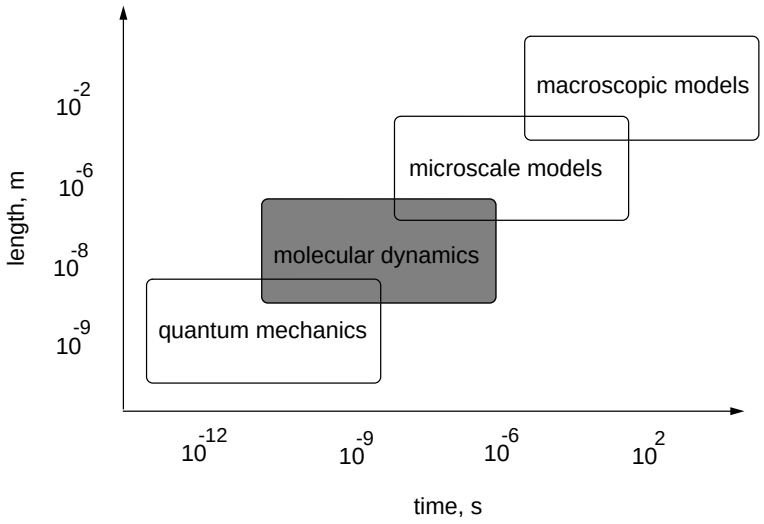

Figure 1.1: Depiction of the relative length and time scales of several modeling techniques. Smaller scale techniques include quantum-mechanically based molecular mechanics and Car-Parinello molecular dynamics. Larger scale techniques include microscopic methods like dissipative particle dynamics and macroscopic numerical models.

The first models of the electrochemical interface were continuum or microscale methods, the most quoted of which is that of Gouy [3] and Chapman [4]. In this model the layer of charge at the metal surface is compensated by a diffuse layer of ions in solution that offset the net charge in the metal. It is assumed that the solution ions follow the Boltzmann distribution: the ion profiles are proportional to an exponential function of the ratio of electric to thermal energy. Debye and Hückel used this model to treat the diffuse charge about an ion. The Gouy-Chapman model has been successful at estimating the double-layer capacitance near the potential of zero charge and the Debye-Hückel model is successful at approximating the chemical potential of ions in dilute solutions. Shortcomings in the Gouy-Chapman model led to the development of the Stern model [5] that incorporates a layer of contact-adsorbed ions into the Gouy-Chapman representation. The Stern model does a better

job at replicating the experimental capacitance for instance; however, a fundamental description of the interactions dominating the interfacial behavior is deficient.

Perhaps the most apparent discrepancy in the Gouy-Chapman theory or Stern model is the assumption of a continuum solvent and counter-ions that results in a predicted monotonic decay in the ionic charge distribution near the surface. It has been shown [6, 7] that this charge distribution instead consists of alternating layers of net positive and net negative charge. As one seeks molecularly resolved interfacial details, continuum approaches are inadequate as they neglect essential details (*e.g.* the dielectric constant of the interfacial region is often treated as a constant).

In contrast to a macroscopic treatment of the interfacial layer, an exact quantum mechanical treatment of the solution and metal electrode would in principle permit complete characterization of the interface. The electronic or charge distribution in the metal and solution would be dynamically available to view, for example, cupric or cuprous ions in their movement from solution to incorporation into the metal matrix during electrodeposition. This detailed view and consequent understanding would clearly have wide-reaching consequences, although such a large-scale quantum-mechanical representation is presently computationally unavailable. By using an approximate or less-detailed quantum treatment of system electron behavior (examples of which are *ab initio* Car-Parinello (CP) molecular dynamics and density functional theory (DFT)), electron transfer, transition state calculations, and other interfacial properties are available, although limited to relatively small systems [8–11].

Molecular simulation of fairly large systems using empirical or regressed *ab initio* pair-wise additive potentials can be performed to obtain statistical property averages that reflect bulk and interfacial macroscopic behavior. This method, as opposed to *ab initio*, DFT, and CP techniques, treats van der Waals and Coulombic interactions in a classical, simplified manner. Molecular simulation techniques such as Monte Carlo and molecular dynamics are able to model larger systems while still retaining atomistic

detail and behavior. That is, molecular simulation resolves important interfacial features that depend on explicit species interactions.

1.2 Molecular Dynamics Approach

Molecular dynamics (MD) is a technique used to classically simulate interacting molecules in a variety of situations. For example, MD has been used to obtain molecularly resolved information on molecular ion-transport channels [12], metal-liquid interfaces [13], and bulk solutions [14]. Simulations techniques used and discussed herein have been successful at offering insight into adsorbed water orientations, ionic distributions, ionic transport coefficients, atomically resolved electrostatic potential profiles, and interfacial capacitance [6, 14–19].

In molecular simulation, an atom or a group of atoms (a molecular site) is assigned Coulombic and van-der-Waals parameters based on intermolecular potentials derived from experimental data, quantum-mechanical calculations, or a combination thereof. Coupled with Newton's equations of motion, these intermolecular or site-site potentials are then used to obtain site positions and momenta as a function of time. From the positions and momenta of the atoms in the system, bulk and interfacial properties can be calculated. Mechanistic information such as how sodium chloride addition affects the adsorption strength of an organic molecule at a copper surface can also be discovered. The molecular-level observations can be coupled with experimental studies to give insight into the action of the species at the atomic level. MD was chosen at the expense of simulating on larger time and length scales, in order to permit molecular-level resolution of species behavior.

Because of the relatively small number of molecules that can be discretely treated in a molecular simulation cell (on the order of 10^6 atoms compared with 10^{23} experimentally), the resolution of the MD results is bounded by the system size and the duration of the simulation. Computational requirements increase as $n \log n$ or

n^2 as the number of simulated atoms n increases. As such, dilute solutions (millimolar concentrations) require excessive amounts of computation when the solvent is explicitely treated (as is done here but is smeared into a continuum elsewhere [20]). As of this writing, molecular simulation is at the cusp of beginning to include reactions on a large scale. Reactions such as proton transport in acidic solutions or oxidation/reduction events are not routinely incorporated into MD simulations; nor are they included here.

The atomically resolved behavior obtained from the molecular dynamics simulations here could be used as input into mesoscopic simulations [21], much like quantum-mechanical intermolecular potentials are used herein as input to molecular dynamics. Understanding how intermolecular interactions contribute to mesoscopic behavior has and will lead to breakthroughs in a diversity of fields. Indeed, manipulation of material interactions is becoming routine at smaller and smaller length scales.

1.3 Scope of Work

Much work has been done using molecular dynamics to obtain atomically resolved details about the solid-solution interface [10, 16, 17, 19, 22, 23]. I build upon that work by developing and implementing an algorithm to approximate the charge dynamics in a metal in contact with a solution. This electrode charge dynamics routine smoothly incorporates metal-cluster quantum-mechanical calculations into large-scale simulations of metal surfaces of arbitrary geometry. Interfacial effects of including internal modes of vibration in the water solvent are also documented. I then give results indicating how an industrially significant organic additive behaves in the double layer using both molecular dynamics and rotating disk electrode experiments.

This work is divided into sections that treat *ab initio* calculations, molecular dynamics simulations, and experimental rotating-disk-electrode results that all aid in determining the structure and dynamics of the electrochemical interface, in particular

how MPSA behaves near that interface. Quantum-mechanical calculations are used to approximate the interactions between atoms or groups of atoms (sometimes referred to as site-site interactions). I use those interatomic potentials coupled with Newton's equations of motion to simulate three interfacial systems: (1) a solution of water and ions near a uniformly charged (100) surface, (2) a solution of water and sodium chloride near a perfectly polarizable copper (111) surface, and (3) a solution of water, sodium chloride, copper sulfate, and MPSA near, again, a perfectly polarizable copper (111) surface. These systems were chosen for reasons that will become apparent in later chapters. Briefly, though, the three systems were chosen to (1) evaluate how internal modes of vibration in the water solvent affect the interfacial structure, (2) determine the interfacial structure of a well characterized system (H_2O and NaCl) near a surface modeled with the new electrode charge dynamics routine, and (3) obtain the adsorption strength of MPSA, with and without NaCl, at a cathodic copper surface.

The majority of this work treats molecular simulation. Towards the end of the dissertation, I supplement the simulation work with rotating-disk-electrode (RDE) experiments. The RDE galvanostatic (constant current) experiments show how the electrode potential changes upon addition of thiol- or sulfonate-containing additives during copper electrodeposition. This is done to obtain *in situ* results that can be used to infer which end of MPSA, thiol or sulfonate, is responsible for inhibition or acceleration of copper deposition. The rotating-disk-electrode experiments coupled with the molecular dynamics of additive and additive-free solutions offer insight into the behavior of copper ions near MPSA and the adsorption of MPSA at the surface with and without sodium chloride present. The subsequent paragraphs introduce the chapter by chapter topics and pertinent results.

Chapter 2 begins by discussing some specifics of molecular dynamics including pair-wise additivity, periodic boundaries, and the Ewald sum. I then give quantum-mechanically, or semi-empirically obtained interatomic potentials for the molecules

that will be simulated in solution. The solution species are water, sodium ion, chloride ion, MPSA (3-mercaptopropanesulfonic acid), cupric ion, cuprous ion, and a bisulfate ion. Instead of presenting all of the molecular model parameters in one chapter, I only discuss interatomic interactions between solution species in Chap. 2. The resolved interatomic interactions between the solution species and the solid surface are discussed in the chapters as the respective species are included in the simulated solution.

Chapter 3 shows the effects of including water internal modes of vibration on ion distributions near a charged insulating surface. I find that including modes of vibration in the solvent model causes an increase in the ion adsorption and ion affinity in the double layer. I also address the calculation of the solution electrostatic potential profile using Poisson's equation.

Chapter 4 presents electrode charge dynamics (ECD), a routine I developed that bridges the gap between small quantum-mechanical calculations and simulations of a metal surface of arbitrary geometry. Quantum-mechanical calculations are carried out on small metal clusters (10-20 metal atoms) that are used to define the van-der-Waals interaction parameters with the metal atoms. The van-der-Waals potentials are then used in concert with the ECD routine to accurately and smoothly model the short- and long-range interactions of the species and the metal surface.

Chapter 5 describes the use of electrode charge dynamics to simulate an aqueous sodium-chloride salt solution in contact with a copper metal. I observe that chloride ions are strongly adsorbed to the surface at both negative and positive potentials, which is consistent with others' results. I also report that the high density layers of water nearest the metal form highly ordered ice 'sheets.'

Chapter 6 presents simulation results on the action of an industrially significant additive MPSA, that aids in the deposition of copper from solution into small copper

channels on a computer chip. I simulate MPSA in an aqueous bath of sodium, chloride, cuprous, cupric, and bisulfate ions near a cathodic copper electrode that is held at electrode potentials that closely relate to experiment. These simulated species are chosen as a model of an experimental aqueous sulfuric-acid copper deposition bath. The simulations in this work are in qualitative agreement with experimental results indicating that chloride ion influences the behavior of MPSA during electrodeposition and enhances the rate of copper deposition. The simulated adsorption energy of MPSA decreases when chloride ions are included in the simulated electrolyte.

Chapter 7 gives details and results of an experimental RDE copper electrodeposition study where I investigate copper deposition inhibition by organic additive addition. I show results that support the hypothesis that it is the thiol chemical group of MPSA that is responsible for inhibiting copper deposition in the absence of chloride ions. Chapter 8 summarizes the simulation and experimental results and proposes a mechanism accounting for copper deposition inhibition by MPSA, acceleration by Cl^-, and acceleration by MPSA and Cl^-.

Chapter 2

Molecular Models of the Aqueous Species

2.1 Introduction

This chapter discusses the molecular dynamics technique as it applies to simulations of solid-liquid interfaces. Section 2.2 discusses some of the key elements of interest when simulating a condensed fluid next to a solid surface. Section 2.3 is the larger of the two sections and treats the molecular models of the aqueous species simulated in this work. The interatomic interactions between solution species that are highlighted below determine the behavior of the three different systems modeled here. In addition to the interatomic interactions between solution species, there are interactions between the species in solution and the surface that are discussed in succeeding chapters.

2.2 Molecular Dynamics Introduction

There are many texts that explain well the principles of molecular dynamics. Some of these include Frenkel and Smit [24], Allen and Tildesley [25] and Rowley [26]. I refer the reader to these well-documented texts for a more thorough discussion

and explanation of molecular simulations. This section briefly discusses molecular interactions, pair-wise additivity, combining rules, and periodicity in slab geometries.

2.2.1 Molecular Interactions

Central to molecular simulation is the need to effectively parameterize the potential energy that describes the interactions between the atoms in the fluid. This potential energy, often referred to as a potential energy surface, is a function of the orientation and separation distance of interacting molecules. The potential energy between two interacting atoms can be partitioned into a few broad categories. These categories include (1) electron-electron or Pauli repulsion that occurs at very close range, (2) short-ranged dispersion or electron correlation interactions, and (3) long-range charge-charge interactions.

Herein, I treat the short-range interactions (categories 1 and 2 in preceding paragraph) of solution atoms interacting with other atoms in solution with the Lennard-Jones (LJ) potential. Long-range Coulombic interactions in solution are often modeled as point charges interacting with other point charges. The LJ potential and Coulomb's law are used in a pair-wise additive scheme to compute the energy and forces in the simulated fluid. The potential energy (U) of the fluid is given by

$$U = \sum_{i}^{N-1} \sum_{j=i+1}^{N} 4\epsilon_{ij} \left[\left(\frac{\sigma_{ij}}{r_{ij}} \right)^{12} - \left(\frac{\sigma_{ij}}{r_{ij}} \right)^{6} \right] + \frac{q_i q_j}{4\pi\epsilon_o r_{ij}}, \tag{2.1}$$

where i and j are site indices, N is the number of sites simulated, ϵ and σ are Lennard-Jones parameters, ϵ_o is the permittivity of free space, and r_{ij} is the distance separating interacting sites.

2.2.2 Pair-wise Additivity

The term *pair-wise additive* denotes that the interaction between site A (an atom or group of atoms) and site B is not affected by the presence of a third site or species.

Here, as is commonly done, I assume that such higher-order multibody effects make only minor contributions to system behavior. This is a valid assumption when pair-wise additive potentials are regressed or obtained in an environment similar to the simulated conditions. If the system is simulated at significantly different conditions than the environment present when parameterizing the potential energy surface, the simulated result may be inaccurate due in large part to the pair-wise-additive assumption.

In the simulations reported on in Chapter 5 interactions in the solution are modeled with effective parameters meaning that the Lennard-Jones parameters were chosen so that properties in the bulk simulation agree with the experimental result. For the simulations of the solution containing MPSA, copper ions and bisulfate ions (not treated until Chap. 6), the interaction potentials between the species in solution (which are detailed in Sec. 2.3 below) are obtained from *ab initio* calculations. From these quantum-mechanical calculations I observe that the interactions between the solution species is dominated by the Coulombic interactions. The dispersion (electron correlation) energy is relatively small. I assume that the pair-wise additive treatment here is a good approximation, *i.e.* the polarizability of the solution species is such that the multibody effects are negligible.

The three systems studied in this work treat the solid-solution interface. Interactions of the solution species with the copper metal surface are not pair-wise additive. That is, the interaction strength between the metal and a chloride ion for instance depends on the charge distribution in the metal. That metal charge distribution depends on the distribution of solution species that surround the chloride ion. The electrode charge dynamics routine (developed in Chap. 4) correctly accounts for these multibody effects when solution species interact with the copper metal.

2.2.3 Combining Rules

In simulating a system consisting of many different species, combining rules are used to predict some of the cross-interaction parameters σ_{ij} and ϵ_{ij} to reduce computational expenses. The number of cross interactions increases rapidly (as n^2) as the number of unique sites n increases. For instance, a system consisting of 16 unique sites (as some of the simulations here do), there are 240 unique LJ parameters that need to be defined. Although it is has been shown [27] that use of combining rules is inaccurate for interactions between species of differing size and ionization potential, I use combining rules to approximately describe some of the cross interactions between different atoms or sites. Here, I assign characteristic LJ parameters σ_{ii} and ϵ_{ii} to each atomic site belonging to a particular molecule. Then using combining rules, I generate the cross interaction LJ parameters σ_{ij} and ϵ_{ij}. For example, the parameters that approximate the potential between a sodium and chloride ion would be found using combining rules, whereas a sodium-sodium interaction would not use combining rules. I use the combining rules proposed by Wheeler and Rowley [28] for the interatomic interactions in solution, where the popular Lorentz portion of the Lorentz-Berthelot rules has been retained. The combining rules are

$$\sigma_{ij} = \frac{\sigma_{ii} + \sigma_{jj}}{2} \tag{2.2a}$$

$$\epsilon_{ij} = \frac{\sigma_{ii}^3 \sigma_{jj}^3}{\sigma_{ij}^6} \sqrt{\epsilon_{ii}\epsilon_{jj}}. \tag{2.2b}$$

As mentioned, I discuss in future chapters (Chaps. 5 and 6) the regression of interatomic interactions between the surface and solution species where combining rules are not used.

2.2.4 Simulation of Slab Geometries Using the Ewald Sum

In molecular dynamics simulations, the system sizes are such that to avoid edge effects the simulated unit cell is periodically repeated. That is, when a molecule moves toward the boundary of the unit cell it interacts with an image of the unit cell. I leave an indepth treatment of periodic boundary conditions to the literature [24, 26] and review here issues that arise when using periodic boundary conditions to simulate fluid bounded by solid surfaces. The systems simulated in this work consist of atoms or sites in such a geometry.

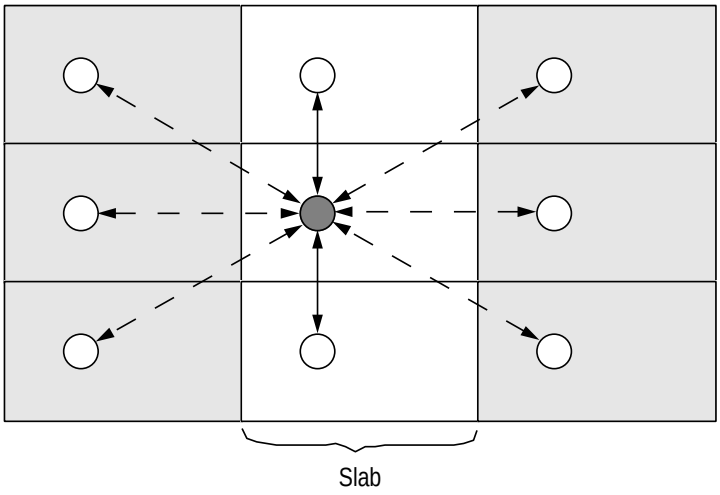

Figure 2.1: 2D slab geometry representation of a single particle system. Undesirable interactions with lateral images are indicated with dashed lines. Lateral images of the unit cell are shaded gray. The shaded particle is in the unit cell.

During a simulation of charged particles bounded by solid surfaces, it is desired that the particles only interact with the particles belonging to the same periodic 'slab.'

That is, periodic replications of the fluid (in the direction normal to the walls) should not interact. This slab geometry is shown in Fig. 2.1.

The Ewald sum is an efficient algorithm to sum the slowly converging or long-range charge-charge interactions [29]. The 2-D formulation of the Ewald sum [30] is a rigorous approach to ensure that the lateral images don't Coulombically influence the particles in the slab of interest. Lateral images of the unit cell are indicated in Fig. 2.1. However, the 2-D Ewald sum is much more computationally demanding than the 3-D formalism. Some have simulated the slab geometry by including a void space that separates lateral images of the unit cell. The 2-D Ewald results are obtained using the 3-D sum when including a void space and a correction term [31]. This results in significant computational savings [32]. Chapter 4 discusses another viable option that negates the use of a void space between periodic slabs while still retaining the benefits of using the 3-D Ewald formulation.

2.3 Interaction Potentials for Species in Solution

For each of the solution species that will be included in the simulations, potential parameters (such as σ and ϵ) must be obtained for inclusion in Eq. 2.1. Lennard-Jones interaction parameters are presented in this section for each of the species that will be included in the simulations even when the species like $MPSA^-$, copper ions, and bisulfate ions aren't used or discussed again until Chap. 6. Throughout the rest of this work I denote the deprotonated form of MPSA (SO_3-$(CH_2)_3$-SH) with the acronym $MPSA^-$.

Solution models of water, sodium ion, chloride ion, and cuprous ion are reviewed in Section 2.3.1. For the other species in solution, there is limited potential model information in the peer-reviewed literature, so I give the parameterized results from *ab initio* calculations. I leave to future chapters (Chaps. 5 and 6) the *ab initio* results and parameterization of interactions between a copper surface and solution

molecules. This section discusses and presents results of the interactions between species in solution.

In addition to those species already mentioned in Chap. 1, I also include derivatives of $MPSA^-$ in the simulated solution: 1,3-propanedithiol (TPT) and 1,3-propanedisulfonic acid ($SSPSS^{2-}$). TPT and $SSPSS^{2-}$ are central in the rotating-disk-electrode experiments reported on in Chap. 7. Specific reasons for including TPT and $SSPSS^{2-}$ in the simulations will be apparent in future chapters.

For each molecule included in the solution, the molecular geometry and point charges at the molecular sites must be defined. In the case of monatomic ions, the point-charge magnitude is defined by the ionic charge. I determined the geometries of $MPSA^-$, TPT, $SSPSS^{2-}$, and bisulfate ions through geometry optimizations at the Hartree-Fock level of theory with the 6-31+G(d) basis set using Gaussian98 [33], a quantum-mechanical calculations package. Point charges at the atomic centers of all the polyatomic species were also found using Gaussian98 but at the second-order Moeller-Plesset (MP2) level of theory and larger basis-set size of 6-311+G(2df,2pd). Charges were assigned to reproduce the calculated dipole moment under the CHelpG scheme using the MP2 density with the hydrogen charges summed onto the associated carbon atoms (if any).

In addition to the model geometry and charge distribution, each site is characterized by Lennard-Jones parameters that define its interaction strength with itself and other molecules in solution. I obtained the solution interaction-potential parameters from either (1) established models obtained from parameterization of experimental data or (2) regression of quantum-mechanical potential scans. In this second method, the *ab initio* system energy, U_{tot}, of two molecules is calculated at multiple points of separation. The interaction energy between the two molecules, U_{ab}, is then found by subtracting the isolated molecular energies, U_a and U_b, from the total, *i.e.*

$U_{ab} = U_{tot} - U_a - U_b$. The *ab initio* energies used to find U_{ab}, U_a, and U_b are calculated at the second-order Moeller-Plesset (MP2) level of theory with basis-set size of 6-31+G(d). The energy U, given in Eq. 2.1, is then fit to U_{ab} by varying σ and ϵ. This formulation neglects the basis-set-superposition error; the reason for this is discussed at the end of this chapter.

The basis sets and MP2 level of theory was chosen to allow for electron correlation and polarization effects in the *ab initio* potential energy scans. For the interactions of water, sodium ion, and chloride ion with copper clusters [34] (discussed in the Chap. 5), the MP2 level of theory and 6-31+G(d) basis set is used to treat the approaching ions and water molecules. I use the same basis set and level of theory to obtain the quantum-mechanical interactions between solution species.

In the regression of the Lennard-Jones site-site interactions for $MPSA^-$ and sulfate ions, I find that 4 parameters can satisfactorily fit the potential energy surface. All the other LJ parameters are either set from previous studies or are found using the aforementioned combining rules (Eq. 2.2). These 4 empirical parameters are the σ values for sulfur (in a sulfonate or sulfate environment), sulfur (in a thiol group), oxygen (in a sulfonate group), and oxygen (in a sulfate group). These parameters are given at the end of the chapter.

In the following section I summarize the water, and monatomic ion parameters as previously established models describe them. I then discuss the predicted versus the *ab initio* interaction energies for the polyatomic species (other than water). (Although the divalent sulfate ion is not included in the simulations, it is included here as it is similar to bisulfate ion and exists in sulfuric acid solutions.) I also present the molecular geometry and charges of the species. Although molecular geometries and charges are presented along side the LJ parametric results for solution species interactions, I model the molecular geometry and charges as independent of the media with which they interact, be it with a solution or a surface.

2.3.1 H_2O, Na^+, Cl^-, Cu^+, and Cu^{2+} Models

In the simulations here, I use the popular SPC/E [35] model of water. It reproduces fairly accurately the properties of water at ambient temperature and pressures [35]. It has three charged sites, and one Lennard-Jones (LJ) site potential located on the oxygen.

Wheeler regressed ionic potentials for sodium and chloride in water by attempting to match experimental solution densities and cation transference numbers at 1 molal salt concentration. The resultant parameters are moderately successful at matching experimental results [14]. Solution densities and binary diffusivities agree well with experiment with less-accurate agreement for solution viscosities as a function of concentration. Cross-interaction parameters are also found using the Wheeler-Rowley combining rules (Eq. 2.2).

Relative to the amount of chloride- and sodium-ion simulation models reported in the literature, few models exist that describe the behavior of cuprous or cupric ions in solution. Fulton *et al.* report Lennard-Jones parameters for cuprous ion used in simulating $[CuBr_2]^-$ [36]. I use Fulton's model of Cu(I). Although there is a three-body potential in the literature used to model cupric ions [37] that is able to correctly reproduce the Jahn-Teller effect, for simplicity and consistency the model of cupric ions will differ from cuprous ions only in its charge.

The model of a cupric ion presented here is unable to reproduce the Jahn-Teller effect that is experimentally observed. The Jahn-Teller effect is a phenomenon where the cupric ion distorts to reach a lower energy which results in a high water exchange rate (cupric ions can more easily shed its hydrating waters than ions of similar electronic structure and charge). As the model of cupric ion here is spherically symmetric within a pair-wise additive scheme, such an anisotropic distortion isn't possible. Molecular dynamic simulations using 3-body potentials to incorporate this ionic distortion do not exhibit any first-shell water exchanges over a 30 ps time frame [37].

Table 2.1: Lennard-Jones parameters and charges for each of the monatomic ions in the simulated solution

	σ, Å	ϵ/k, K	q, $\lvert e\rvert$
Na^+	2.35	55.3	1.000
Cl^-	4.42	54.2	-1.000
Cu^+	1.55	50.32	1.000
Cu^{2+}	1.55	50.32	2.000

I expect effects stemming from anisotropic distortions in the cupric-ion hydration structure to be small over the simulation time scale here also.

The parameters for each of the monatomic ions in solution are given in Table 2.1. Note that the well-depths (as given by ϵ) for the like-like interactions (*e.g.* Na^+-Na^+) are very similar, while there are significant differences in the size parameter σ. This size parameter greatly influences the hydration of the ion as does the ionic charge. Generally speaking, the smaller the size, the greater the strength of hydration.

2.3.2 MPSA$^-$ Model

I model MPSA$^-$ with nine interacting sites: 3 sites for the sulfonate oxygens, 1 site for the sulfonate sulfur, 3 sites for the carbon backbone, 1 site for the sulfide sulfur, and 1 site for the sulfide hydrogen. Shown in Figure 2.2 are the nine sites with their accompanying Coulombic charges found from *ab initio* calculations at the MP2 level with basis set of 6-311+G(2df,2pd). Charges on the hydrogens bonded to carbon atoms are summed into the carbon charge and assigned to the -CH_2- site.

Although experimentally based short-ranged interaction parameters are available for some of the MPSA$^-$ sites, I desired more system-specific potentials to represent well the interaction of the sulfide and sulfonate groups with water and various ionic species. I globally regress LJ parameters for MPSA$^-$ by approaching MPSA$^-$ with

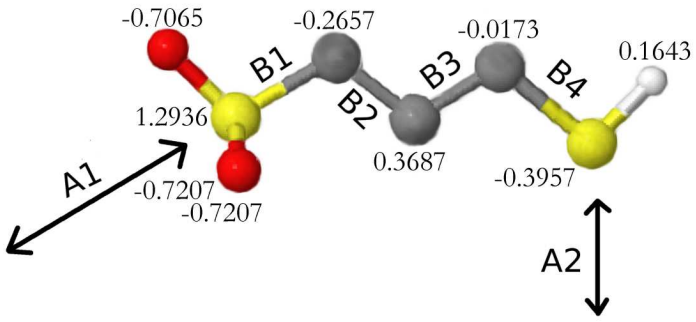

Figure 2.2: Pictorial representation of $MPSA^-$. A1 and A2 represent the lines of approach used to regress interaction parameters with A1 approaching the sulfonate group and A2 the sulfide group. B1 through B4 label the bonds about which dihedral potentials have been calculated. Site charges, in units of $|e|$, are also indicated. These site charges are found from *ab initio* calculations at the MP2 level with basis set of 6-311+G(2df,2pd). Charges on the hydrogens bonded to carbon atoms are summed into the carbon charge and assigned to the -CH_2- site. Hydrogens attached to sp^3 carbons are not shown.

several species along the A1 and A2 lines of approach in Fig. 2.2. The species that approach $MPSA^-$ to arrive at the LJ parameters for $MPSA^-$ are water, sodium, chloride, and cuprous ion. Wheeler-Rowley combining rules are used to get the modeled interaction potentials. The A1 and A2 approaches were chosen as they minimize secondary effects due to the presence of the other atoms of $MPSA^-$ in obtaining parameters for the sulfide and sulfonate sites.

A water molecule, chloride ion, sodium ion, and a cuprous ion each singly approaches the sulfonate and sulfide groups of $MPSA^-$. The LJ interaction parameters for the sulfur and oxygen atoms were found using Gaussian98 [33] with a split valence RECP (Relativistic Effective Core Potential) basis set, augmented with a single set of f-type polarization functions [34, 38] for calculations involving the cuprous ion. The LJ parameters for the -CH_2- sites were fixed at the OPLS values [39]. OPLS refers

to Optimized Potentials for Liquid Simulations; these are interaction parameters regressed to match the simulated results with experimental properties [39, 40].

Like the hydrogen sites on SPC/E water, the hydrogen site at the sulfide group was assigned a well-depth of zero ($\epsilon = 0$) while retaining its Coulombic charge. This choice of setting ϵ for the sulfide-hydrogen site to zero is consistent with sulfide parameters for the thiol group in cysteine reported by Kaminiski *et al.* [40].

The *ab initio* potential scans are shown as points below in Figure 2.3 and 2.4. The lines represent the fit of the quantum-mechanical points. When water approaches $MPSA^-$ in the *ab initio* potential scans, the geometry was fixed at the SPC/E [35] values. The above combining rules (Eq. 2.2) were used in calculating the predicted interaction energy (shown as the solid or dashed lines in Figure 2.3 and 2.4).

The Lennard-Jones fit of the *ab initio* data matches very well in the case of water, shown in Fig. 2.3(a). This is encouraging as in this work the majority of interatomic interactions involving $MPSA^-$ will be with the solvent, water. When water approaches the sulfonate head group, the most favorable interaction is about 40 kJ/mol more negative than when approaching the sulfide group.

Figure 2.4 shows potential energy curves as a function of distance when chloride and cuprous ions approach the $MPSA^-$ molecule along the routes in Fig. 2.2. Here, I am not regressing additional sodium, chloride, water, or cuprous ion LJ parameters for interactions with MPSA. Using the combining rules I globally fit LJ parameters for MPSA only. Agreement between the LJ fit and the *ab initio* results agree within 5% at distances greater than about 4 Å. At shorter distances $MPSA^-$ is able to polarize and thus significantly enhance the attraction (for Cu^+) or decrease the repulsion (for Cl^-). This polarization effect is only partially accounted for in the pair-wise Lennard-Jones potential.

The corrected points given in Fig. 2.4(b) show that the basis-set-superposition error is relatively small in the case of the cuprous-MPSA potential scan. I expect

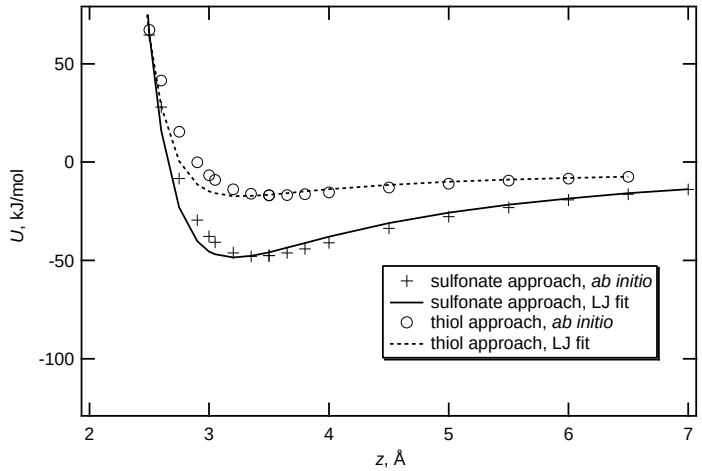

(a) MPSA water scan.

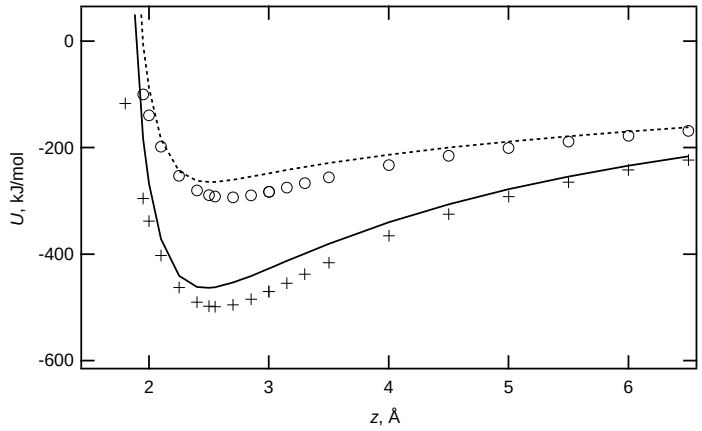

(b) MPSA sodium ion scan.

Figure 2.3: *Ab initio* potential scans of MPSA for (a) water and (b) sodium. Distances are measured from the ion (or oxygen atom in the case of water) to the sulfur atom. Water and sodium approach the sulfonate and sulfide groups of $MPSA^-$ as indicated in Fig. 2.2. In the case of the water scans, the water dipole moment points toward $MPSA^-$ and coincides with the lines of approach.

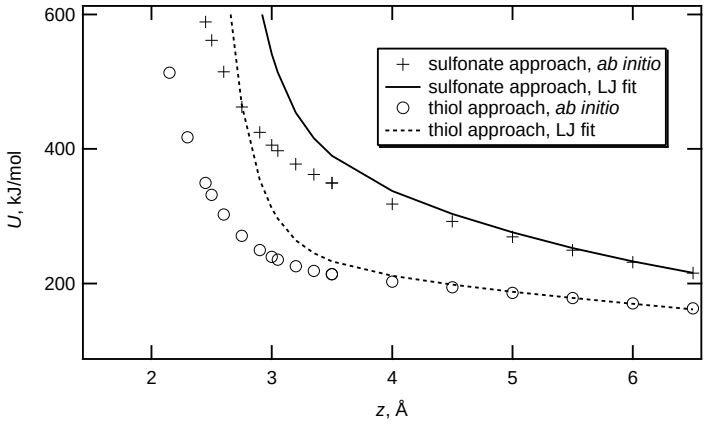

(a) MPSA chloride ion scan.

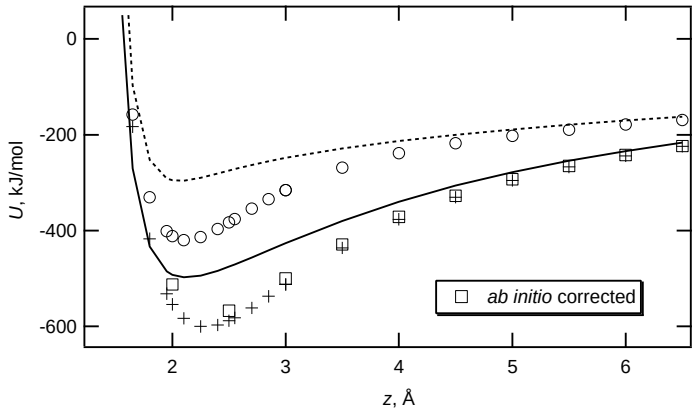

(b) MPSA cuprous ion scan.

Figure 2.4: *Ab initio* potential scans of MPSA for (a) chloride and (b) cuprous ion. Distances are measured from the ion to the sulfur atom. Chloride and cuprous ion approach the sulfonate and thiol groups of $MPSA^-$ as indicated in Fig. 2.2. In (b) the *ab initio* corrected points reflect the small basis-set-superposition error.

that the other scans with MPSA would also reflect a similar trend. More will be said about this error in the conclusions in this chapter.

The fact that use of the combining rules and the regressed $MPSA^-$ parameters doesn't fit the well-depth of the cuprous-$MPSA^-$ scans indicates that perhaps the *ab initio* result overpredicts the interaction of Cu^+ with $MPSA^-$. Note how deep the well is in the *ab initio* potential scan, almost 600 kJ/mol. As the sodium-MPSA potential is well represented in regions were the interactions are Coulombically dominated, it seems that the charges on the MPSA sites are accurate. I would expect likewise that at the interaction well, where charge-charge interactions dominate the interaction, the predicted energy based on the charges on the MPSA sites interacting with the +1 charge of the cuprous ion would better agree with the *ab initio* result. The fact that I don't see agreement in the *ab initio* and predicted Cu^+-MPSA scans indicates that the quantum-mechanical result may be overestimated.

Cupric ion-MPSA scans are not included in the regression of the LJ solution parameters for MPSA as I had difficulty obtaining realistic *ab initio* results for the Cu^{2+}-MPSA scans. The Cu^+-Cu_{10} cluster scans discussed in Chap. 6 also show somewhat unexpected results. Better models describing the quantum-mechanical interactions of cupric and cuprous ions with a diversity of species are needed.

In Fig. 2.2 I indicated the bonds about which the $MPSA^-$ dihedral angles can change. I have used Hartree-Fock-level calculations with the basis set 6-31+G(d) to obtain the dihedral potential parameters. The form of the potential is

$$U_{dihedral} = \sum_{i=0}^{5} A_i[\cos(\theta)]^i, \tag{2.3}$$

where $U_{dihedral}$ is the dihedral energy, θ the dihedral angle, and A_i are the dihedral potential parameters. The predicted energy, found from Eq. 2.3, never varies more than 3 kJ/mol from the quantum-mechanical data. Table 2.2 contains the dihedral

Table 2.2: $MPSA^-$ dihedral potential parameters around the bonds indicated in Figure 2.2, in units of K.

	B1	B2	B3	B4
A_0	1181.	482.5	1601.	567.6
A_1	-3596.	-802.6	-2150.	-1174.
A_2	-12.14	4763.	917.1	-415.0
A_3	4795.	5000.	5030.	1333.
A_4	13.72	-1059.	785.3	61.19
A_5	-0.87	47.13	435.9	-58.08

potential parameters A_i. These are also used to determine the dihedral motion in TPT and $SSPSS^{2-}$.

2.3.3 TPT and $SSPSS^{2-}$ Models

As shown in Figure 2.2, $MPSA^-$ has a sulfonate group and a thiol group at the ends of a propane chain. In the case of TPT and $SSPSS^{2-}$, the two groups flanking the propane chain are the same: thiol for TPT and sulfonate for $SSPSS^{2-}$. Thiol and sulfonate groups are at the ends of TPT and $SSPSS^{2-}$, respectively. Experimentally, I investigate how these molecular changes affect the experimental inhibition or acceleration of copper deposition. Analogous to the experimental, I am also interested in simulating the effects of $MPSA^-$ end-group substitutions.

The site charges for TPT and $SSPSS^{2-}$ are found in the same manner as $MPSA^-$ as previously described. Listed in Table 2.3 are the charge and model coordinates for the organic additives. This is in partial summary of this and the previous section treating $MPSA^-$. The reader may notice that the charges on TPT are symmetric (*e.g.* the charge on the two thiol sulfurs are the same); this is due to the C_{2V} symmetry of TPT. This is not the case for $SSPSS^{2-}$ as it belongs to the point group C_2, though the site charges on opposite halves of the molecule differ by less than 3%.

Table 2.3: Charge and model coordinates for the simulated organic additives: $MPSA^{-}$, TPT, and $SSPSS^{2-}$

	q, $\lvert e\rvert$	x, Å	y, Å	z, Å
$MPSA^{-}$				
H	0.1643	0.0000	-0.8823	0.0000
S	-0.3957	0.0000	0.1216	0.8794
C	-0.0173	0.0000	-0.9016	2.3931
C	0.3687	0.0000	0.0000	3.6150
C	-0.2657	0.0000	-0.8219	4.8919
S	1.2936	0.0000	0.2246	6.3637
O	-0.7207	1.2321	1.0126	6.2377
O	-0.7207	-1.2321	1.0126	6.2377
O	-0.7065	0.0000	-0.7292	7.4770
TPT				
H	0.2049	0.0000	-0.5771	0.0000
S	-0.3309	0.0000	0.3879	0.9204
C	-0.1159	0.0000	-0.7050	2.3766
C	0.4838	0.0000	0.1581	3.6282
C	-0.1159	0.0000	-0.7050	4.8797
S	-0.3309	0.0000	0.3878	6.3359
H	0.2049	0.0000	-0.5772	7.2563
$SSPSS^{2-}$				
O	-0.7797	0.0000	-1.1428	0.0000
O	-0.7560	1.2054	0.6797	1.0009
O	-0.7560	-1.2054	0.6797	1.0009
S	1.3791	0.0000	-0.1081	1.0015
C	-0.2277	0.0000	-1.0193	2.5539
C	0.2709	0.0000	-0.1945	3.8414
C	-0.2141	0.0000	-1.1279	5.0524
S	1.4175	0.0000	-0.3703	6.6852
O	-0.7640	0.0000	1.0566	6.4911
O	-0.7850	-1.1990	-0.8586	7.3156
O	-0.7850	1.1990	-0.8586	7.3156

As the interatomic interactions between solution species are largely dominated by Coulombic forces, I assign the same $MPSA^-$ LJ parameters to the corresponding sites in TPT and $SSPSS^{2-}$. In effect I'm assuming that the Coulombic portion of the interactions swamp out any secondary effects due to atomic changes four atoms removed from the approaches reported in the previous sub-section on $MPSA^-$. This is a reasonable assumption as similar changes don't significantly affect the van der Waals parameters when approaching a copper surface (section 6.2.1).

2.3.4 Divalent Sulfate Ion Model

I obtain the interaction parameters for $MPSA^-$, bisulfate ion, and copper ions as these species are simulated near a copper surface in an effort to understand how $MPSA^-$ behaves during experimental copper deposition with and without sodium chloride present. As Chap. 6 discusses, these species are included in the simulated electrolyte to approximate the experimental bath near the copper surface. Although it is known that bisulfate ions are the most prevalent species in sulfuric acid solutions, here I include the parameter regresion for divalent sulfate ion as it is similar to the bisulfate ion. The bisulfate ion model is given in the next subsection.

As in the case of $MPSA^-$, I was unable to find a thorough Lennard-Jones parameterization of sulfate or bisulfate ions interacting with water and other ions. Though, Impey *et al.* report on solid $LiSO_4$ and give parameters to use with the exponential-6 potential [41]. Here I have again used Gaussian98 to obtain Lennard-Jones parameters for sulfate to be used with the Wheeler-Rowley combining rules. I choose a sulfate ion approaching another sulfate ion and a water approaching a sulfate ion to obtain parameters that when used with the combining rules will accurately embody the most prevalent sulfate interaction: sulfate interacting with the water solvent.

I model the sulfate divalent ion with two unique sites, one on the sulfur and the other on the oxygen atoms, for a total of five sites. It has a tetrahedral structure, point

group T_d, with a distance from sulfur to oxygen atoms of 1.5033 Å. The charges were found in the same manner as indicated above for $MPSA^-$; the results gave a charge on sulfur of 1.8668 $|e|$. The LJ parameters were determined by fitting the sulfur and oxygen parameters to the *ab initio* scans. In Figure 2.5 is shown the results of the *ab initio* and model calculations. Directly above the plot are shown sulfate-sulfate and sulfate-water pictorial representations of the approaches. In each route shown, either two sulfur and two oxygens or one sulfur and two oxygens are colinear.

2.3.5 Bisulfate Ion Model

In the previous sections dealing with $MPSA^-$ and divalent sulfate ion, I fit the *ab initio* results to U in Eq. 2.1 by varying the LJ parameter values. In this sub-section, those same parameters are used to check the agreement between the theoretical and predicted results; no new parameters are regressed. The bisulfate ion is probed with water and another bisulfate ion. I probe with water to ensure that the water-sulfate interaction is accurately modeled as water is the most abundant species in solution. I find that use of the previously arrived at LJ parameters, with use of the Wheeler-Rowley combining rules, give model predictions that agree well with the *ab initio* results.

Figure 2.6 shows the results for the bisulfate-bisulfate scans as well as depictions of the orientations used. In each scan, a sulfur and oxygen on each bisulfate ion are colinear. The LJ fit matches the *ab initio* result within 10% at distances greater than 3.5 Å.

Figure 2.7 gives the results for the four water approaches to the bisulfate ion. Also in the figure are shown pictorial depictions of the two attractive and two repulsive routes. In each scan or route, one sulfur and two oxygen atoms are colinear. The LJ interaction of the attractive routes agree well with the *ab initio* results, though the model over-predicts the repulsion experienced in Routes 2 and 3.

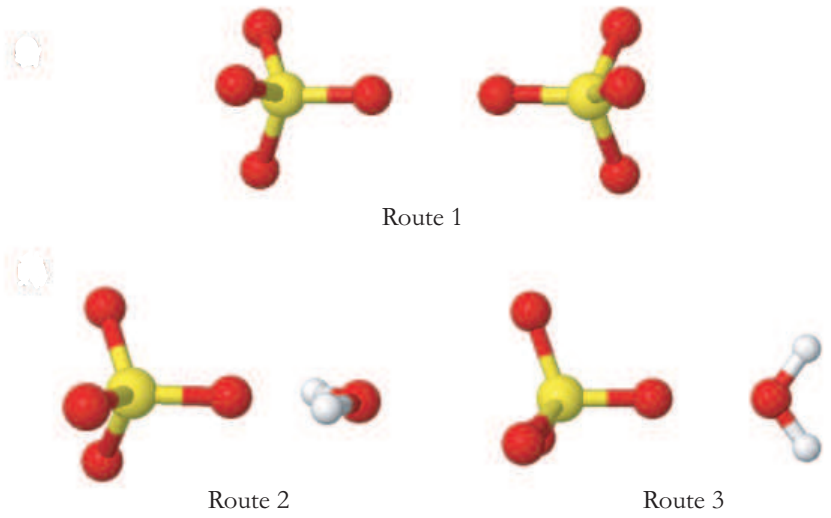

(a) Pictorial representation of sulfate scans.

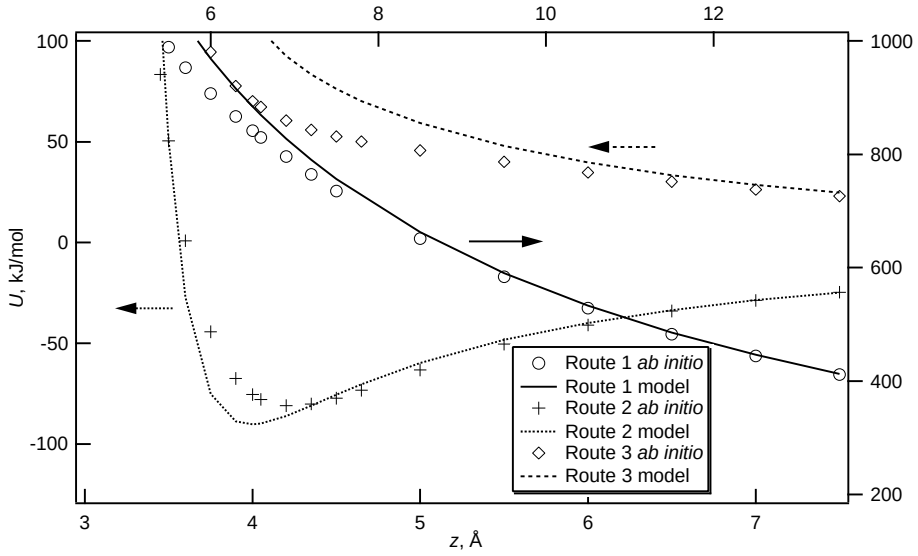

(b) Potential energy of sulfate scans.

Figure 2.5: *Ab initio* potential energy scans and fitted results of the divalent sulfate ion. Distances are measured from the ion (or oxygen atom in the case of water) to the sulfur atom. In each route, either two sulfur and two oxygens or one sulfur and two oxygens are colinear. Route 1 data and fit are referenced to the right abscissa and top ordinate.

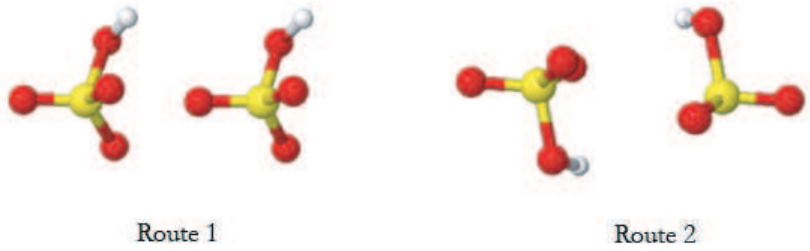

(a) Pictorial representations of bisulfate-bisulfate scans.

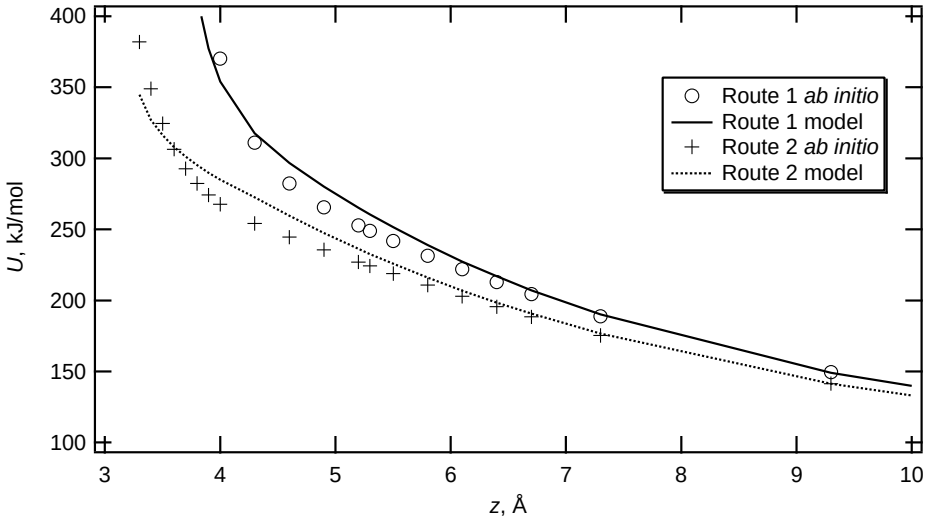

(b) Potential energy of bisulfate-bisulfate scans.

Figure 2.6: *Ab initio* and model potential energy of bisulfate-bisulfate scans. Distances are a measure of sulfur-sulfur separation. In each route, two sulfur and two oxygen atoms are colinear.

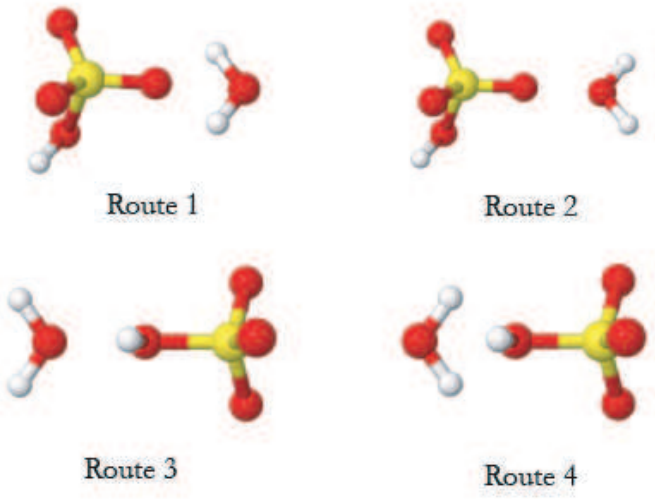

(a) Pictorial representation of bisulfate-water scans.

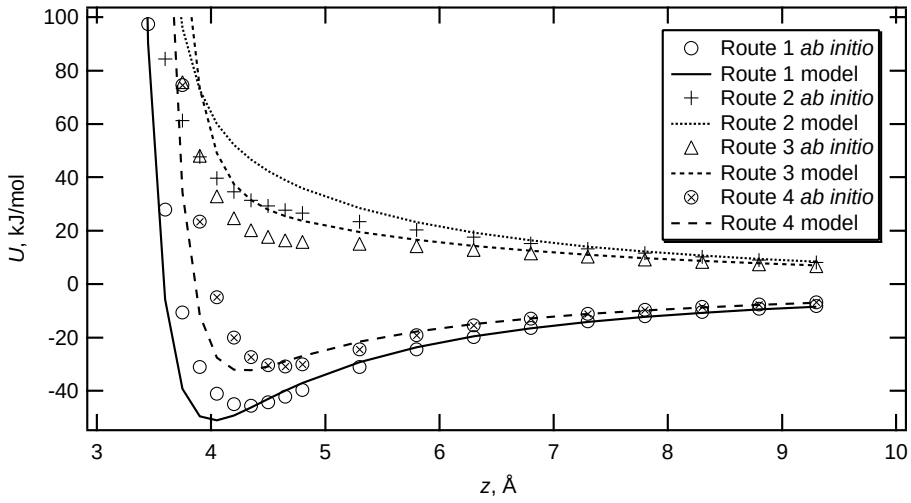

(b) Potential energy of water-bisulfate scans.

Figure 2.7: *Ab initio* and model potential energy of water-bisulfate scans. Distances are a measure of sulfur-sulfur separation. In each route, one sulfur and two oxygen atoms are colinear.

Table 2.4: Charge and model coordinates for the bisulfate ion. The charges and model geometry were found in the same way as previous models.

	q, $\|e\|$	x, Å	y, Å	z, Å
S	1.4285	-0.0720	-0.0720	0.7769
O	-0.6958	-0.8721	0.8423	0.0001
O	-0.6958	0.8424	-0.8720	0.0000
O	-0.7472	-0.8041	-0.8042	1.7968
O	-0.6651	0.8913	0.8914	1.6808
H	0.3754	0.6916	0.6917	2.5863

Table 2.4 gives the coordinates and charges for the bisulfate ion model. The charges and model geometry were found in the same way as previous models

When simulating bisulfate ion, I allow the hydrogen to swivel about the attached oxygen. That is, the dihedral angle defined by the oxygen-sulfur bond changes according to the potential given in Eq. 2.3 with constants A_i equal to 288.5, -398.4, -266.1, 423.9, -3.045, and -5.158 Kelvin, respectively.

2.3.6 Summary

Here I have presented regressed interaction potentials involving $MPSA^-$, TPT, $SSPSS^{2-}$, sulfate, and bisulfate ions. When charged species approach other charged species, the potential is Coulombically dominated. That is, the magnitude of the effective LJ dispersion, $4\epsilon\sigma^6$, is small relative to the charge-charge interaction. For example, the Coulombic interaction between a sodium ion and a sulfonate oxygen is 50 times larger than the dispersive interaction at 2.5 Å. In such cases, the potential effectively consists of a charge-charge interaction and a Pauli repulsion term. Thus, one of the LJ parameters can be fixed, and not used in the fit. For each of the sites here for which I regress LJ interaction parameters, I fix the ϵ parameter to values found in the literature. The ϵ values for sulfur and oxygen (in the sulfate, bisulfate,

Table 2.5: LJ parameters for $MPSA^-$, TPT, $SSPSS^{2-}$, and sulfate ions used to describe interatomic interactions between solution species.

	σ, Å	ϵ/k, K
S	3.405	125.9
S_{thiol}	3.407	213.9
$O_{sulfonate}$	3.054	100.7
$O_{sulfate}$	2.537	100.7
CH_2	3.905	59.38
H	0.	0.

or sulfonate groups) are given by Vishnyakov and Neimark [42], and the ϵ parameter for thiol sulfur was left at the OPLS value [40].

Listed in Table 2.5 are the summarized LJ parameters for $MPSA^-$, TPT, $SSPSS^{2-}$, and sulfate ions used to describe interatomic interactions between solution species. As seen in Table 2.3 the charge on the thiol sulfur is much more negative than the sulfonate sulfur. From this it could be expected that the ϵ for thiol sulfur would be greater than sulfonate sulfur because greater electron density results in a greater electron correlation effect in the case of thiol sulfur. Values for the sulfur ϵ parameters are consistent with this reasoning.

From the agreement between the predicted and quantum-mechanical scans presented here, water's interaction with the solution components will be well represented. I also have shown that the LJ predictions of bisulfate scans fit well the *ab initio* result without parameter modification. This result and the small amount of variable parameters used in conjunction with the combining rules in the regression indicates that other cross interactions (such as a cuprous-bisulfate or chloride-TPT interactions) also are likely to be acceptably reproduced.

Will Use of These Parameters Reflect Reality?

Through the use of experimentally regressed parameters and *ab initio* calculations, the interaction of water and monatomic ions with $MPSA^-$ can be satisfactorily parameterized to reproduce the *ab initio* quantum-mechanical results. I have not shown, however, that the use of all these parameters to model a liquid simulation leads to realistic property or behavioral predictions. The chapters that follow will treat that subject. As an introduction, I list points that support or undermine the argument that these models accurately represent a real fluid system of similar length and time scales.

The *ab initio* calculations reported here and in future chapters are all performed in vacuum. I have argued here that the molecular site charges are of primary importance. In a liquid-like polarizing media or an electrochemical solution, the site charges of the model molecules are likely to fluctuate about a different value than found in vacuum. The electronic structure of the molecules of interest can be affected by the solution: an example is the enhancement in the dipole moment of water when moved from vacuum to liquid.

The error introduced due to simulating with the reported vacuum molecular site charges may be important with models containing sulfur. The other models' charges were found by incorporating situationally relevant experimental or theoretical results. Although there is also good agreement (average deviation of 10 %) when comparing the sulfonate and thiol site charges to corresponding site charges found in cysteine [40] and nafion [42] model molecules.

Multibody effects in solution will not be explicitly included. These are caused by the proximity of a third or more molecules influencing the interaction between a pair or group of molecules. Depending on the system and the property considered, the error introduced by neglecting multibody effects varies [43]. Including multibody effects reduces the amount of phase space simulated for a given level of computational effort.

I valued the ability to simulate larger systems over longer time frames over any possible errors introduced by the neglect of multibody terms in interatomic interactions. The following chapter discusses how including internal modes of vibration (which allow for multibody type influences) in the water model molecules affects the structure of the solid-liquid interface. Chapter 4 discusses how I have included multibody type interactions at the interface between a liquid and an ideally polarizable surface. An ideally polarizable surface is one that responds to the charge distribution in the solution phase and doesn't leak charge; that is, reactions at the metal surface don't occur.

In all the quantum-mechanical calculations reported on in this work, the basis-set superposition error (BSSE) is neglected. In interatomic potential scans, the BSSE arises from the availability of the partner molecule's base orbitals for electron occupation. It results in an artificial lowering of the interatomic potential. The magnitude of the error depends strongly on the electron structure of the interacting species. As of yet, there isn't a viable scheme to properly correct the error in strongly interacting systems [44]. One commonly used method to estimate the BSSE is the counter-poise correction scheme. With metal clusters, some studies use it [45, 46] while others do not [47–49]. Particularly in the case of metal clusters, the counter-poise correction may overcorrect the BSSE [34]. I neglect the BSSE as the majority of interatomic interactions in this work are Coulombically dominated. For example, in the case of MPSA interacting with a cuprous ion, the BSSE is small as the interaction is dominated by the molecular charges of the interacting species (Fig. 2.4(b)). In the case where the interaction isn't Coulombically dominated, *e.g.* water interacting with a copper metal cluster, the interatomic interactions parameters reported herein approximate the true dispersion interaction [13].

This chapter discussed and presented models of the interatomic interactions between the solution species. The models of the solution species have fixed geometries.

I do not include intramolecular modes of vibration in the polyatomic models. The next chapter addresses how intramolecular modes of vibration in the water model affect the ion distributions at a solid-solution interface.

Chapter 3

Solvent Vibrational Mode Effects

3.1 Introduction

This chapter discusses the influence of including bond and angle vibrational modes in the water model on ion distributions near the solid-solution interface. I observe that including the modes of vibration, among other things, results in an increase in the ion density near the uniformly charged non-metallic surface, and an increase in ion-affinity. This chapter introduces the work by reviewing related molecular simulations, and constitutes the earliest work done in the project [18].

Previously, Crozier *et al.* performed molecular dynamics simulations on a model aqueous electrolyte solution between two surfaces [19] using a rigid, nonpolarizable model for water. In that study, the potential in the double layer exhibited an oscillatory behavior near the solid surface owing to the discrete nature of the molecular system. The simulated oscillations in the potential cannot be predicted from theories that do not include a molecular description of the solvent. The non-monotonic character of the interfacial properties agrees qualitatively with the interfacial fluid structure suggested by simulation [50] and experimental [51] studies of a mercury-water interface.

Several recent studies [52–56] of bulk water and electrolyte systems have used models that include polarization of the solvent molecules, self-consistent with the instantaneous molecular environment. Molecular polarizability may impact the structure of the double layer near a charged surface and affect the solvation energy of the ions in the bulk. With this in mind, I perform molecular dynamics (MD) simulations of aqueous electrolyte solutions confined between surfaces of varying applied charge using a flexible model for water that allows angle bending and bond vibrations. The resultant double layer structure and ion solvation characteristics are compared to previous results for rigid water molecules with fixed dipole moments [19]. This comparison allows me to focus on solvent effects resulting directly from the flexibility of the solvent and the concomitant polarizability, or change in dipole moment, created by this flexibility.

This chapter also gives the calculated electric field within the confined aqueous electrolyte obtained by integrating the one-dimensional Poisson equation. The integration may be performed from the center of the simulation cell to the solid surface, but I find that for very dilute concentrations the electric field damps out asymptotically from the solid surface and extends into the solution a long distance relative to the simulation cell length. This electric field penetration distance depends strongly on the concentration of mobile charge carriers in solution. Consequently, I have chosen to calculate the field by integrating Poisson's equation from the solid surface outward by assuming a uniformly charged-sheet value for the field at the solid surface. This field (at a uniformly charged-sheet) is equivalent to the charge density on the surface divided by the permittivity of free space. While this assumption is not rigorous very near a surface consisting of discretely charged molecules, I show that deviations from a three-dimensional solution of Poisson's equation are small. Using this procedure, I am able to show the influence of ion concentration on the electric field and assess any limitations due to the computational domain.

3.2 Simulation Specifics

I have used three different water models in the simulations reported on in this chapter. In previous related studies, SPC/E [35] water molecules were simulated between two model surfaces [19,57]. In the SPC/E model, the dispersion interactions are treated with a spherical Lennard-Jones (LJ) potential located at the center of the oxygen atom. Polar interactions are included through equivalent partial positive charges located at the hydrogen nuclei, but the hydrogen atoms in this model do not have any LJ potentials assigned to them. An equivalent negative charge is also assigned to the oxygen atomic center.

To examine the effects of polarization due to model flexibility, without a full relaxation of the electron density distribution, I have formulated a flexible SPC/E model, or SPC/E-F, in which a harmonic potential [58, 59] coupled with a multiple-time-scale integrator is used to determine intramolecular motion. The bond distances and bond angles for the isolated SPC/E-F molecule are identical to those in the SPC/E model. However, the equilibrium bond distances and angles are different when in condensed-phase simulations.

To separate out flexibility effects from induced dipole effects caused by changes in the equilibrium geometry in the condensed phase, I performed simulations using a third model, SPC/E-Fd, in which the equilibrium bonds and angles in the liquid are fixed to produce the same dipole moment at the simulation conditions as the rigid SPC/E model. Given in Table 3.1 are the bond and angle harmonic potential parameters for the flexible models where r°_{OH} is the harmonic equilibrium OH bond distance, $<^{\circ}_{\mathrm{HOH}}$ is the harmonic equilibrium HOH bond angle, r_{OH} is the average OH bond distance, $<_{\mathrm{HOH}}$ is the average HOH bond angle, k_b is the harmonic bond constant, and k_a is the harmonic angle constant.

As in previous collaborative studies [19,57], the model fluids were placed between two surfaces comprised of fixed, charged LJ spheres. Simulations were performed

Table 3.1: Three molecular models of water simulated in this study. SPC/E is rigid, whereas SPC/E-F and SPC/E-Fd include internal modes of vibration.

	SPC/E	SPC/E-F	SPC/E-Fd
r°_{OH} (Å)	1.00	1.00	0.99
$<^{\circ}_{\mathrm{HOH}}$ (rad)	1.911	1.911	1.978
r_{OH} (Å)	1.01	1.02	1.01
$<_{\mathrm{HOH}}$ (rad)	1.88	1.82	1.90
k_b (kJ/mol/Å^2)	$\cdots$	4638	4638
k_a (kJ/mol/rad^2)	$\cdots$	384	384
Vibrational freq. (cm^{-1})	$\cdots$	1621, 3662, 3749	1621, 3663, 3736

at surface charge densities of 0, $\pm$0.1, and $\pm$0.2 C/m^2 and ion concentrations of 0, 0.5, and 1M. The SPC/E-Fd model was used in simulations at $\pm$0.1 C/m^2 surface charge density and 1 M ion concentration. The univalent ions were modeled as LJ spheres with mass, σ and ϵ values of 18.015 amu, 78.178 K, and 3.169 Å, respectively (same σ and ϵ parameters as the oxygen atom in SPC/E water). As in the previous collaborative work with a rigid solvent, the cation and anion are identical except for charge. The ions are the same size to compare the hydration of the positive and negative ions near the surface and in the bulk without the added effect of the size differences between anions (such as Cl^-) and cations (such as Na^+).

The lengths of the cell in the x, y, and z directions were 85.12, 25.5 and 25.5 Å, respectively. The solid surfaces were positioned at 0 and 42.56 Å so that half the cell was filled with fluid; the other half of the cell was empty space to damp out long-range interactions (see Reference [31]). Each surface was modeled with 289 LJ atoms distributed as a single layer of a BCC lattice, exposing the [1 0 0] surface, with a lattice constant of 1.5 Å. The LJ parameters for the surface atoms were σ = 1.5 Å and ϵ = 50 K. Lorentz-Berthelot combining rules were used to obtain the cross parameters between the fluid and surface atoms.

Ten simulations were performed at each condition. All simulations were initiated from unique starting configurations and included 105 ps of equilibration and 200 ps of data collection. The time step size was 2.5 fs. Results are an average of the ten runs performed at each condition. Coulomb real-space and Lennard-Jones interactions were cut off at 10 Å. Long-range Coulombic interactions were treated with the particle-particle-particle-mesh (P^3M) technique [29], using an alpha value of 0.3007 $Å^{-1}$ and the Yeh and Berkowitz correction term [31]. The P^3M mesh size was 16 x 16 x 64 in the x, y and z directions, respectively. One thousand mobile molecules were in each simulation at a bulk density of 60 mol/L and a temperature of 300 K. A fifth-order gear predictor-corrector integrator was used in conjunction with Gaussian constraints for the rigid SPC/E model; an rRESPA algorithm [60, 61] was used for the flexible models in which ten 'fast' steps were integrated for each long step.

3.3 Results and Discussion

This section presents the results and discusses the significance of these molecular-dynamics simulations. I first discuss the bulk property differences between the rigid and flexible models. I then discuss the differences in the hydration of ions in bulk solution and in proximity to the solid surfaces. A discussion of the electrical properties of the simulated solid-liquid interface concludes this section.

3.3.1 Bulk Property Comparisons for the Three Models

To compare the differences between solvent models in bulk phase properties, bulk NVT simulations with periodic boundaries (no solid-liquid interfaces) were performed. In these cases, 1000 molecules were simulated in a cubic box of length 30.25 Å. The results for the SPC/E-F model in Table 3.1 show that the introduction of flexibility increases the OH bond lengths and compresses the HOH angles. The combination results in a 5% increase in the condensed-phase dipole moment. The potential energy

of the system is lower for the flexible model because of the increased equilibrium dipole moment and resultant stronger hydrogen bonds.

The self-diffusion coefficient is also decreased, presumably by this same mechanism. Results for the SPC/E-Fd model show that the decrease in potential energy for SPC/E-F is due to the increased dipole moment as the potential energy for SPC/E-Fd is nearly equal to that of the rigid model. Interestingly, flexibility by itself (SPC/E-Fd) increases the self-diffusion coefficient; this effect is also seen by Tironi *et al.* [58] as well as Teleman and Jönsson [59]. The increase in the self-diffusion coefficient due solely to flexibility may be due to increased mobility and reduced drag as molecules can deform to move past one another. This explanation is consistent with results from other simulations that indicate that flexibility decreases viscosity [62, 63].

Table 3.2 compares bulk properties (intermolecular potential energy U_{inter}, intramolecular potential energy U_{intra}, average dipole moment $< \mu >$, and self-diffusion coefficient D) obtained using the models used in this study with values reported for other flexible models already in the literature and experiment. The frequencies of condensed phase bending and symmetric/asymmetric stretch of the flexible models agree well with water vapor experimental values [64] (1595, 3657, and 3756 cm-1). It is known that the IR absorbance for these same stretching modes decreases in the condensed-phase water; no density dependence is observed here owing to the use of perfectly harmonic intramolecular potentials to model the bond and angle vibrations [65].

3.3.2 Ion Hydration Results in the Absence of a Solid-Liquid Interface

A comparison of bulk solution structure characteristic of the models was investigated by computing the ion-oxygen radial distribution function (rdf). Figure 3.1 (a) shows a comparison of the cation-O rdf obtained for the various models using an average of five independent runs at an ion concentration of 0.063 M. If an ion-ion distance

Table 3.2: Comparison of bulk properties obtained from SPC/E and various models of water that include flexibility.

	SPC/E	SPC/E-F	SPC/E-Fd	SPC/F[1]	SPC-mTR[2]	exp[3]
T (K)	298	301	301	298	298	298
ρ (g/cm^3)	1.08	1.08	1.08	0.996	0.998	0.997
U_{inter} (kJ/mol)	-48.6	-53.1	-48.0	-41.2	-48.71	-41.5[4]
U_{intra} (kJ/mol)	$\cdots$	7.2	6.8	5.9	7.07	
$<\mu>$ (D)	2.41	2.54	2.39	2.30	2.44	2.6-3.0
D (10^{-5} cm^2/s)	2.2	1.8	2.6	4.6	2.7	2.3

[1] Tironi, Brunne and van Gunsteren [58]
[2] modified Toukan-Rahman model [65]
[3] experimental data from Refs. [66, 67]
[4] includes U_{intra}

was less than 20 Å the fluid structure was excluded from the rdf averages so as to compare the ion-O rdf functions of just the hydration of water, without the affects of possible ion pairing. Figure 3.1 (b) shows a similar comparison for the anion-O rdf. Flexibility is seen to increase the first peak height (the peak representing the fluid structure closest to the ion) for both ion models. While a similar effect is observed in Figure 3.2 (b) for the anion-H rdf, flexibility has little apparent effect on the cation-H rdf shown in Figure 3.2 (a).

The increased dipole moment of the SPC/E-F model does produce a slight increase in the anion-H rdf with a minor shift to shorter distances in the second peak, but much of the increase in peak height seems to be due to the flexibility itself. These first-peak results suggest that the primary effect of the flexible solvent is packing; *i.e.*, slight deformation of the solvent molecules permitting higher density in the first coordination shell. Due to the asymmetry in the model water molecules, the negative ion is more strongly hydrated as seen by the location and magnitude of the first peak in the rdf plots. This is because in this study the anion and cation are of equal size and so the partial positive charge on the hydrogen sites can get much closer to

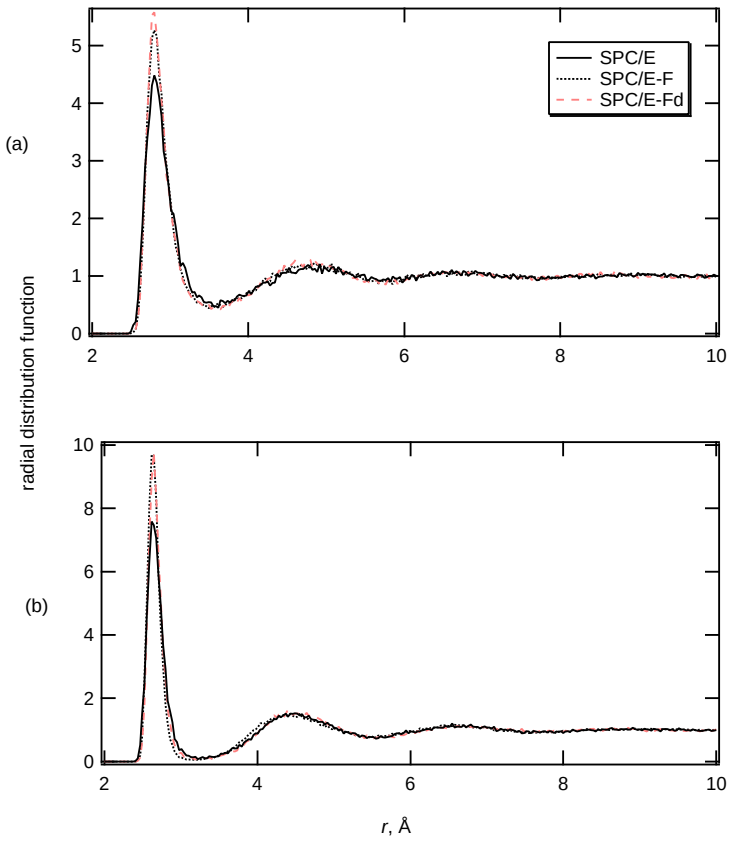

Figure 3.1: Ion-O radial distribution functions for a (a) cation and (b) anion using the SPC/E, SPC/E-F, and SPC/E-Fd models.

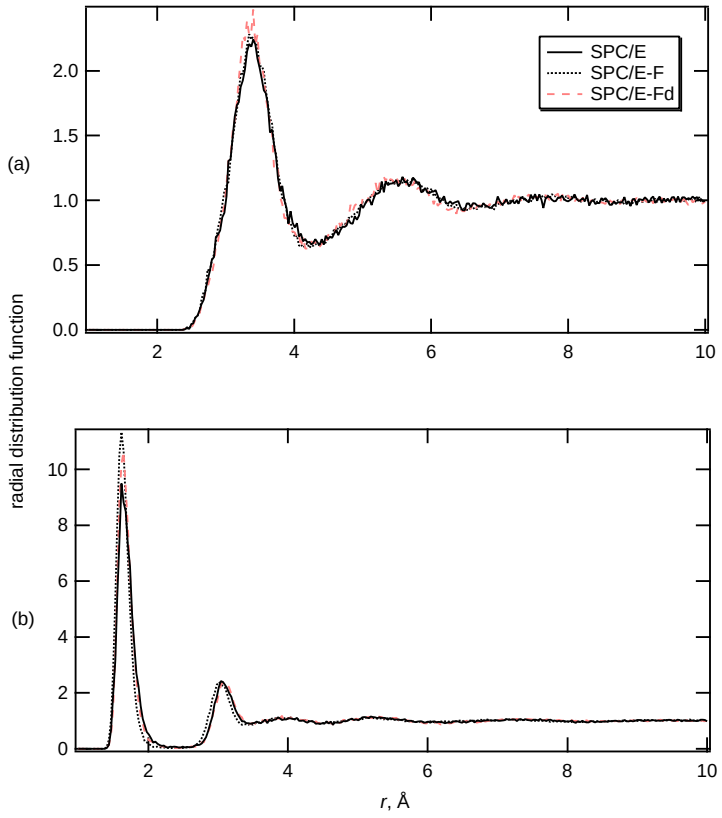

Figure 3.2: Ion-H radial distribution functions for a (a) cation and (b) anion using the SPC/E, SPC/E-F, and SPC/E-Fd models.

the charge center of the counter-charged ion than can the partial negative charge at the center of the oxygen site. Obviously, in real systems where the anion is often significantly larger than the cation, this same charge-separation explanation would suggest that the anion would be less strongly hydrated.

3.3.3 Ion Hydration in Proximity to the Solid Surface

Figure 3.3 shows the ion density distributions obtained from the simulations for different charges on the solid surfaces at a bulk ion concentration of 1 M (compare with ref. [68]). Results for the flexible model are shown at the right; results for the rigid model are shown on the left. The results for the SPC/E-Fd model at an surface charge density of ± 0.1 C/m^2 are overlaid on the SPC/E-F plot in Fig. 3.3 (b) and are similar to those of the other flexible model. Close examination shows an additional anion peak close to the wall for the SPC/E-Fd model and increased height in other peaks near the wall indicating weaker hydration relative to the SPC/E-F model. However, the differences between the SPC/E-Fd and SPC/E-F results are small relative to the difference between the results of either of these models and the rigid model. I therefore show comparisons only between the SPC/E and SPC/E-F models at the remaining conditions.

Figure 3.3 (a) shows ion-density comparisons for uncharged surfaces. The presence of the primarily repulsive wall terminates the hydrogen-bonding network within the solvent, and water molecules have a preferred orientation at even an uncharged wall (compare Fig. 3.5). This orientation of the dipolar solvent creates a small field. As can be seen in the left-hand plot of Fig. 3.3 (a) for SPC/E water, there is a small enhancement of the ion densities in the so-called Outer-Helmholtz plane (OHP) of both surfaces due to this solvent orientation propensity. However, the more tightly hydrated ions with the SPC/E model do not permit as much orientation of the solvent

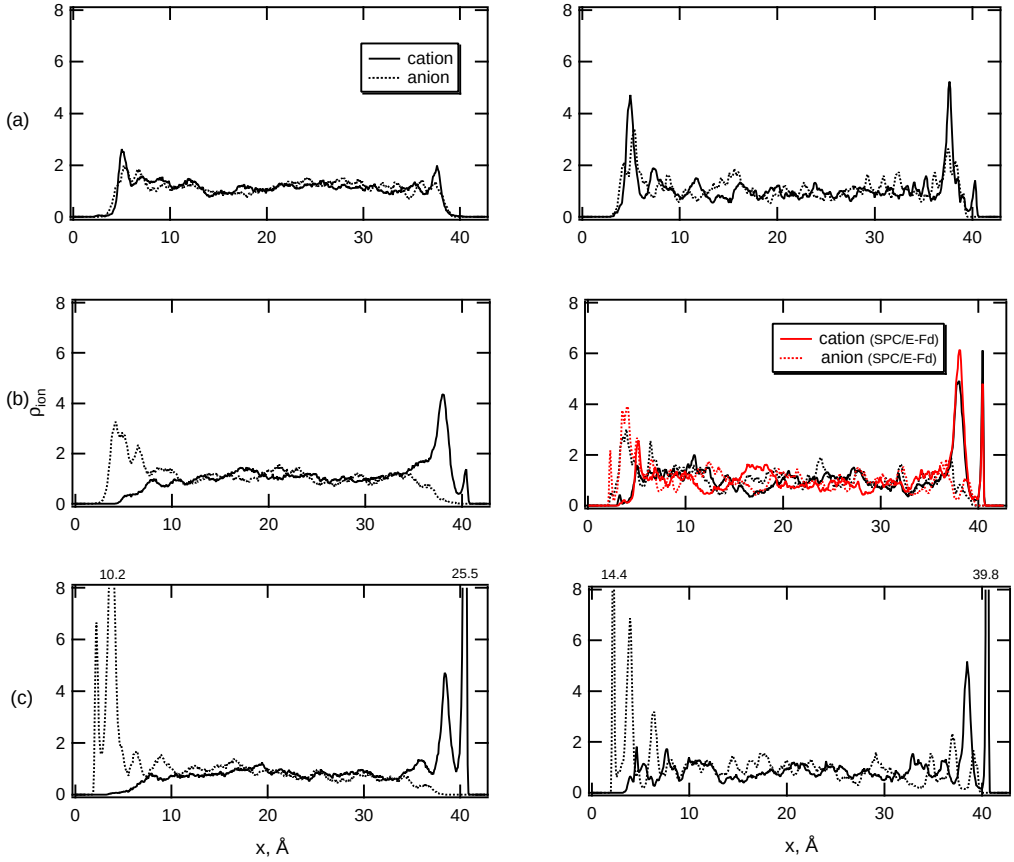

Figure 3.3: Cation and anion average ion density profiles as a function of distance away from the positively charged surface for 1 M bulk concentration. The negative surface is located at 42.56 Å. Surface charge densities are (a) 0.0, (b) ± 0.1, and ± 0.2 C/m^2. SPC/E model results are on the left, SPC/E-F on the right. In the case of ± 0.1 C/m^2 the SPC/E-Fd model cation and anion results are overlaid in red.

at the wall in response to the termination of the hydrogen bonding as do the less-tightly bound ions hydrated with the SPC/E-F model.

The flexible model permits higher solvent orientation at the walls in the presence of ions with a resultant larger ion density enhancement at both neutral surfaces as shown on the right of Fig. 3.3 (a). Evidence of the weaker hydration of the ion with SPC/E-F can also be seen by the increased ion affinity in Fig. 3.3 (a) (right), characterized by the close proximity of counter-ion peaks not present for the rigid model. When the charge on the wall is increased to ± 0.1 C/m^2, flexibility enhances the cation contact adsorption (the Inner-Helmholtz plane or IHP) which is not as pronounced with the SPC/E model. Little effect is observed for the anion. Contact adsorption is again enhanced by solvent flexibility at a charge density of ± 0.2 C/m^2 shown in Fig. 3.3 (c). Contact adsorption of both ions is significantly enhanced by the solvent's flexibility. Again note the ion affinity at these higher charges for the flexible solvent.

Figure 3.3 (c) shows that, in comparison to the rigid model and even in comparison to the flexible model at ± 0.1 C/m^2, some of the cations are pulled back toward the positive surface and some of the anions are pulled closer to the negative surface by their counter ions. The flexible ion density plots are also seen to be rougher than their rigid counterparts, though they represent averages over the same time period, suggesting that the system with the flexible-solvated ions tends to equilibrate more slowly. This decreased ion mobility may be due to an increase in ion-ion interactions and a stronger water hydrogen-bond network, both owing to the weaker ion-solvent interaction for the flexible solvent.

Results at a lower ion concentration, 0.5 M, are shown in Figure 3.4. At this concentration, the effects of flexibility on the IHP are less prominent. However, ion affinity is again seen to be more dominant for the flexible solvent. Strong ion affinity is seen with the surface charge densities of ± 0.1 and ± 0.2 C/m^2.

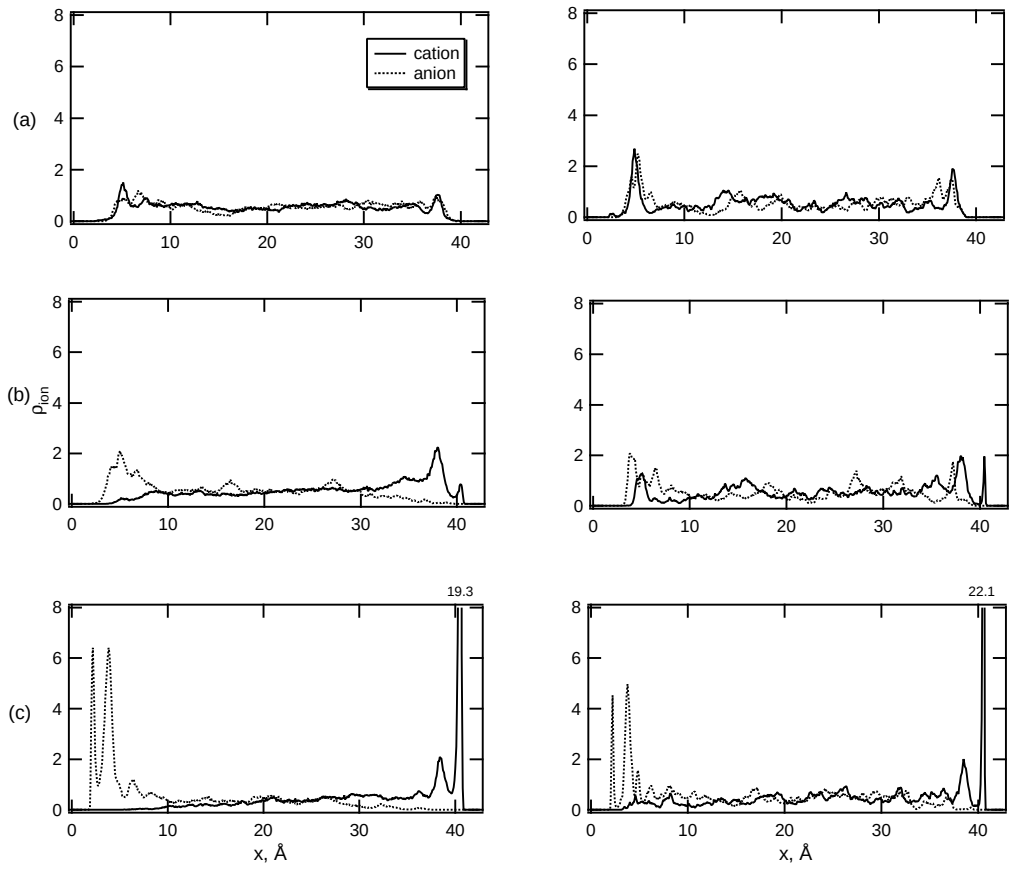

Figure 3.4: Cation and anion average ion density profiles as a function of distance away from the positively charged surface for 0.5 M bulk concentration. The negative surface is located at 42.56 Å. Surface charge densities are (a) 0.0, (b) ± 0.1, and ± 0.2 C/m^2. SPC/E model results are on the left, SPC/E-F on the right.

The ion profiles that are plotted in Figures 3.3 and 3.4 and, indeed, the water molecule profiles that I have not plotted, have appreciable maxima and minima in the density profiles [19, 57, 69]. The water density profiles are not plotted as they are negligibly different from the water profiles given in a previous study of rigid water [19]. This is in pronounced contrast to the prediction of monotonic profiles by the venerable Gouy-Chapman theory that neglects the size of the ions and replaces the discrete water molecules by a continuum. Such non-monotonic profiles have been predicted by theory [70] for nearly three decades and have been seen in recent experiments.

3.3.4 Electrical Properties of the Double Layer

The electric potential, ϕ at any point x (relative to the solid surface) in the double layer may be calculated by integrating the one-dimensional Poisson equation from $x = \infty$ to x [70] or

$$\phi(x) = -\frac{e}{\epsilon_0} \sum_i z_i \int_\infty^x (x - x')\rho_i(x')dx', \tag{3.1}$$

where ρ_i is the local density of site i which has charge z_i, and ϵ_0 is the permittivity of free space. In previous studies [19, 31] it was assumed that the MD simulation cell size is large enough to apply an equation similar to Eq. 3.1 from the center of the cell to x. This assumes that $E = -d\phi/dx = 0$ at the center of the cell. The validity of this assumption depends upon the relative sizes of the MD cell and the double layer; the latter is a function of the surface charge and the ion concentration.

Because orientation of the water molecules constitutes a sensitive measure of the field in the cell, I have examined the zero-field assumption in terms of the water dipole distribution shown in Figs. 3.5, 3.6, and 3.7. Water orientation in these figures is characterized by the projection of the water dipole onto the normal vector for each solid surface, pointing into the cell, or cosθ. Shown are the distributions of cosθ for the rigid SPC/E model as a function of cell position for pure water at surface charge

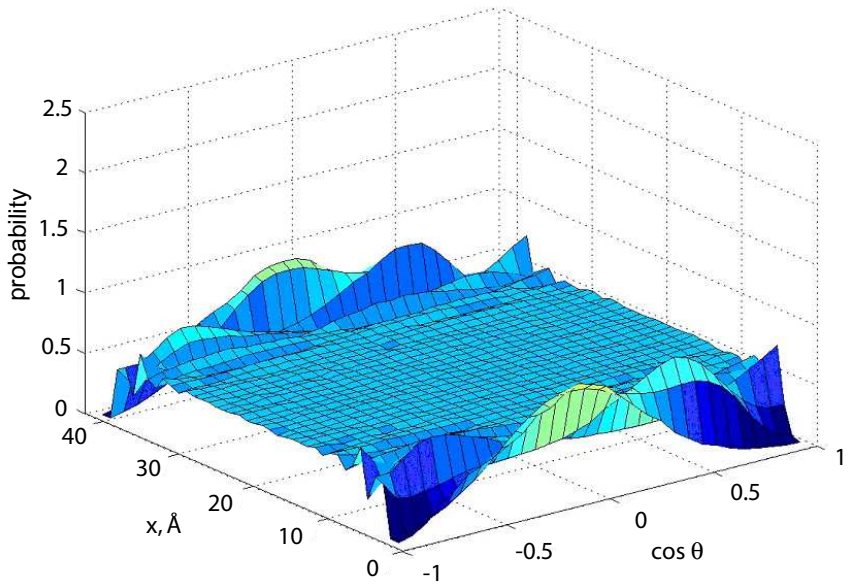

Figure 3.5: Dipole orientation surface for SPC/E model water at a surface charge of 0.0 C/m^2 and 0 M ions. The positively charged surface is located at 0 Å.

densities of 0 (Fig. 3.5) and $\pm$0.1 C/m^2 (Fig. 3.6) and for a nominal concentration of 1 M ions added with a surface charge density of $\pm$0.1 C/m^2 (Fig. 3.7). Note that by referencing to each solid surface, there is a sign reversal at the center of the simulation cell for cosθ in Figs. 3.5, 3.6, and 3.7.

In Fig. 3.5, a preferred orientation of water molecules at the solid walls produces a net dipole near the wall that damps out quickly with distance from the surface. Hence, the assumption of zero field at the midpoint of the cell is valid for the conditions shown in Fig. 3.5. However, in Fig. 3.6 the dipolar solvent does not completely damp the field because there are no mobile charges present. In Fig. 3.7, the addition of ions eliminates most of the field, but there is yet a small field at the center of the cell as evidenced by the slight bump in the profile. The diffuse layer in which there is still a

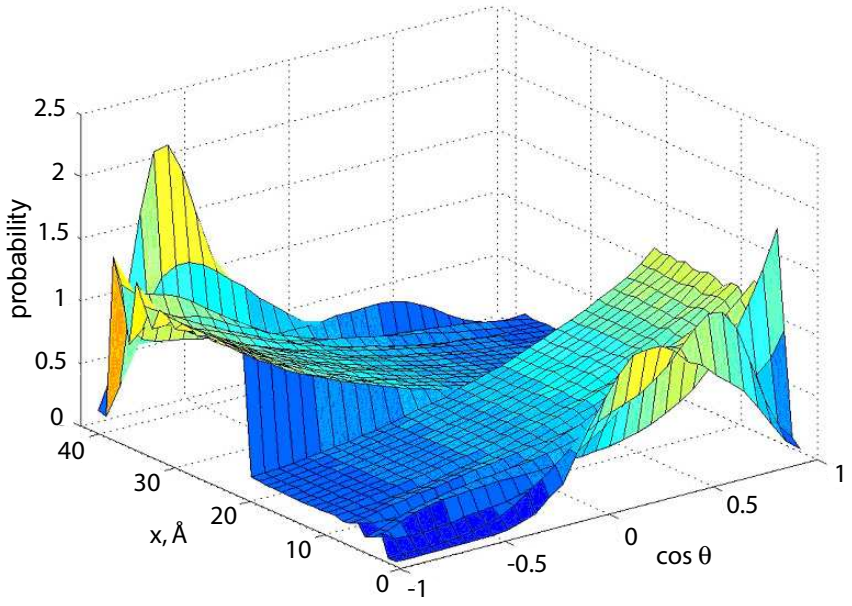

Figure 3.6: Dipole orientation surface for SPC/E model water at a surface charge of ± 0.1 C/m^2 and 0 M ions.. The positively charged surface is located at 0 Å.

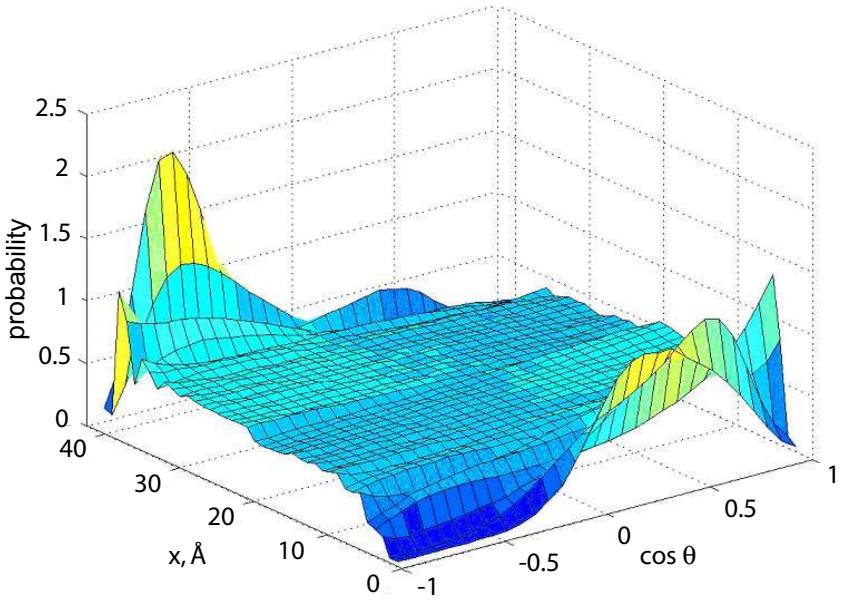

Figure 3.7: Dipole orientation surface for SPC/E model water at a surface charge of ± 0.1 C/m^2 and 1 M ions. The positively charged surface is located at 0 Å.

small field present is quite large because of the decreasing diffusional response of the ions to the diminishing field further out from the solid surface. The assumption of a zero field at the center of the cell may be problematic in this case. Polarizability in the SPC/E-F model enhances the dipole orientations at the solid surface and shields the field to a greater degree. This also enhances the possibility of ion affinity as previously noted.

As an alternative to finding the potential from Eq. 3.1, one can integrate Poisson's equation from the solid surface to x, thereby avoiding the use of a possibly incorrect boundary condition. In so doing, the field at the solid surface ($x = 0$) must be known and is obtained from the applied external field. In this work, I have assumed the field present at the surface is equal to the uniformly charged sheet value, q/ϵ_0, to obtain

$$\phi(x) = -\frac{e}{\epsilon_0} \sum_i z_i \int_0^x (x - x')\rho_i(x')dx' - \frac{q}{\epsilon_0}x + \phi(0), \tag{3.2}$$

for the potential distribution, where q is the charge density at the solid surface ($x = 0$), and ($\phi = 0$) is a constant at the solid surface.

Because the model surfaces are molecular in nature with a body-centered-cubic distribution of charges in the yz plane, the one-dimensional Poisson equation with a charged sheet boundary condition is not rigorous very near the solid surface. To test deviations of the field near the molecular surface from that of a charged plate, test charges were used to probe the field (with no solution present) as a function of distance from the surface. Figure 3.8 shows the average electric field divided by the charged plate value, E_{CP}, obtained from the test charges using an Ewald sum with a convergence parameter of 0.287 $\mathrm{\AA}^{-1}$. As can be seen from the average value and the one-sigma confidence interval plotted in Fig. 3.8, the approximation of replacing E with E_{CP} at the solid surface produces an average error of less than 3% (though deviations from the homogeneous field assumption for individual charges

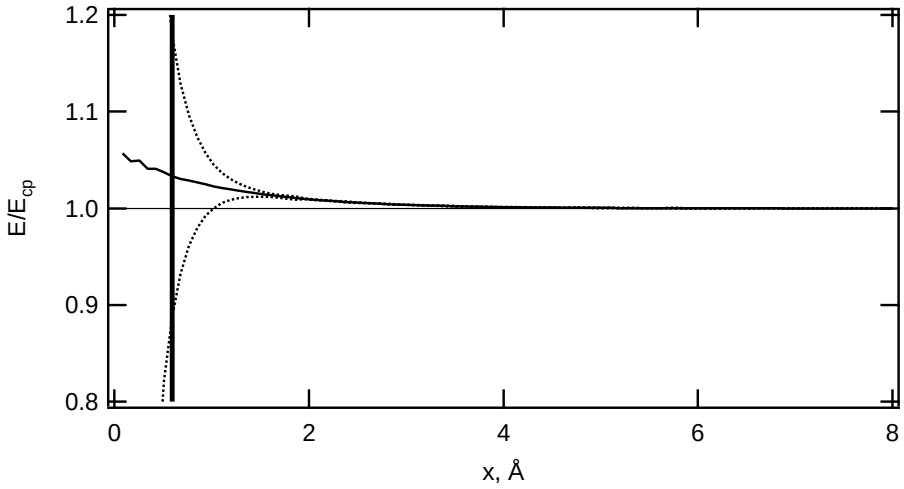

Figure 3.8: Average electric field deviations (solid line) from the uniformly charged plate value as a function of distance from the bcc [1 0 0] point-charged solid surface with a lattice constant of 1.5 Å. The dashed lines represent a one standard deviation range and the vertical bar represents the distance of closest approach of any charge in the MD simulations.

can be larger) in the field at the distance of closest approach (as obtained from the simulations and shown by the vertical line in Fig. 3.8) of a charged site. The error introduced by this assumption is seen to be even smaller at distances greater than x = 0.60 Å.

Figure 3.9 shows electrostatic potential versus cell position (for the SPC/E model with a surface charge density of ± 0.2 C/m^2) calculated from Eq. 3.2. The observed non-monotonic behavior of the potential drop reflects very well the results obtained by Philpott and Glosli [16] and Spohr [15] for NaCl solutions. It is also evident that increasing charge carrier concentration better shields the electric field produced by the charge density on the surfaces. Note that the constant in Eq. 3.2, $\phi(0)$, was fixed to give a value of zero for the voltage at the center of the simulation cell. The flexible

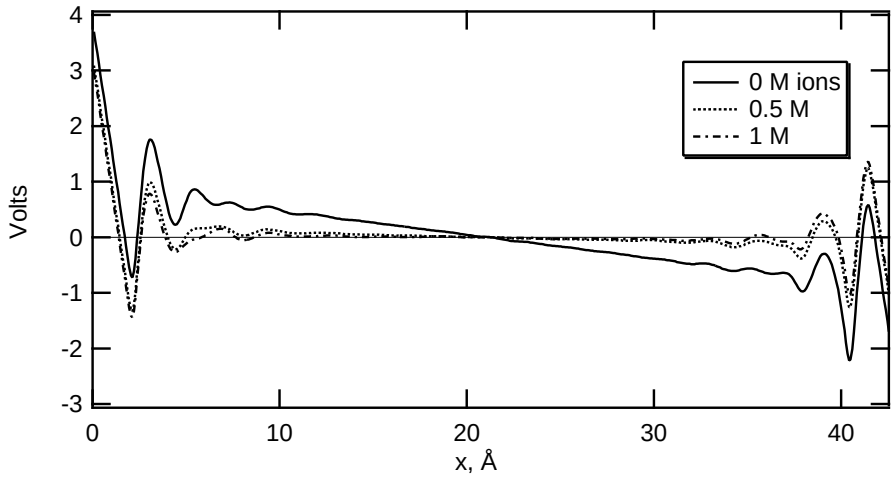

Figure 3.9: Potential drop profile for SPC/E water at a surface charge density of ± 0.2 C/m^2 with an ion concentration of 0, 0.5, and 1 M. Potential set to zero at cell center.

counterpart of Figure 3.9 possesses the same shape with slightly different half-cell voltage drops.

I note that the potential profiles of Figures 3.9 reflect the non-monotonic density profiles of the ions and water molecules. The potential profiles predicted by the Gouy-Chapman theory are monotonic. Thus, the Gouy-Chapman profiles are qualitatively and quantitatively in error. Quantitative errors in the Gouy-Chapman potentials are usually overcome by semi-empirical adjustment of parameters; however, no amount of parameter adjustment can overcome qualitative errors.

Figure 3.10 shows the half-cell voltage drop versus the surface charge density for the SPC/E-F model; results for SPC/E are not shown but are visually indistinguishable. The electrostatic potential drop is approximately a linear function of the charge density. It is of interest to note that the slope of this relationship is smaller for negative surface charges. Likewise, the experimental curves are not symmetric. Thus, the asymmetry in Figure 3.10 agrees with the results in Figures 3.3 and 3.4 where on

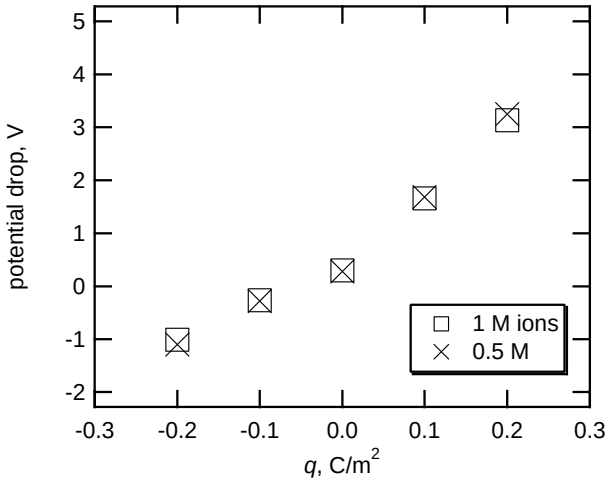

Figure 3.10: Half-cell potential drop as a function of surface charge for 0.5 and 1 M ion concentrations as obtained from the SPC/E-F model.

average, the cations are closer to the negatively charged surface than are the anions to the positively charged surface. The water molecules reinforce this effect. Geometrically, the positively charged hydrogen atoms in the water molecules can approach closer to the solid surface than can the oxygen atoms. A smaller charge separation next to the negative solid surface results in a smaller potential difference for a given magnitude of the surface charge.

The asymmetry seen in Fig. 3.10 is a feature of the model parameters employed here, in particular the equal ion size for anions and cations. Generally, anions are larger in diameter and, more importantly, less fully hydrated than are cations. It is anticipated that this ion size effect, plus any asymmetry in the response of electrons of the electrode to the electrode charge, could easily shift the asymmetry so that it is the slope of the potential difference for positive electrode charge that is smaller as is seen in most experiments.

Table 3.3: Electric field (V/nm) and 95% confidence interval (in parentheses) at the center of the simulation cell.

		q (C/m^2)		
Model	Ion conc. (M)	0.0	0.1	0.2
SPC/E	0.0	0.00 (0.03)	0.13 (0.04)	0.43 (0.05)
	0.5	0.00 (0.07)	0.03 (0.14)	0.06 (0.09)
	1.0	0.00 (0.12)	0.03 (0.11)	0.02 (0.10)
SPC/E-F	0.0	0.00 (0.03)	0.10 (0.05)	0.31 (0.05)
	0.5	-0.02 (0.14)	0.11 (0.15)	0.13 (0.12)
	1.0	0.00 (0.11)	0.03 (0.16)	0.10 (0.10)

Values of the electric field calculated at the center of the simulation cell for the various conditions are shown in Table 3.3. Significant positive values for the field in the center of the fluid indicate that the fluid doesn't completely shield the surface charge. Significant negative values (which aren't seen) would indicate that the solution overcompensates the surface charge. The electric field values in the middle of the cell suggest that the double layer thickness is increased by solvent flexibility. This result may be due to the decreased ability of the mobile charge carriers to shield the field because of the enhanced counter ion affinity.

3.4 Conclusions

Introducing flexibility into the SPC/E model causes significant changes in solvent properties. I have used two flexible models, SPC/E-F and SPC/E-Fd, to distinguish effects due to a flexible geometry from those that result from the changed dipole moment in the condensed phase. Both effects appear to impact the diffusion coefficient of the pure solvent while the model effect on total energy is due primarily to the dipole moment change. Both effects tend to increase the height of the first oxygen and hydrogen ion rdf peaks. The increase in rdf peak height appears to be mainly due to geometrical packing considerations as evidenced by detailed density profiles that

suggest the hydration strength of the ions is smaller for the flexible solvent models. Ion density profiles show that contact adsorption at solid surfaces is enhanced by ∼40% with solvent flexibility. Ion affinity is also enhanced when the ions are solvated with flexible water molecules.

I have also shown that care must be taken when using finite-sized cells with low concentrations of ions in a strong externally applied field. Although the mobile charges dampen out most of the field rather quickly, a small solvent dipole orientation may persist for a significant distance into the diffuse layer. In such cases, a good alternative to assuming a zero field at the center of the simulation cell, is integrating Poisson's equation from the solid surface outward. I have shown that this can be done with good accuracy by using E_{CP} for the field at the solid surface even when the surface is modeled with fixed molecular centers and these discrete centers constitute the loci of any added surface charges. Using this method for calculating the field, I found that the half-cell voltage drop is a function of the surface charge and bulk ion concentration.

In the remaining chapters, I do not include vibrational modes in the water solvent. I use the rigid SPC/E model of water to describe all the interatomic interactions (with combining rules) with the other species in the solution. A primary benefit is that more phase space (about 50%) can be simulated with the same amount of computational effort due to the time savings of avoiding the multiple time-scales demanded by including intramolecular vibrational modes. Also, the SPC/E model is well defined and is frequently used thus making it convenient to obtain well characterized water-species interactions such as water-water, water-sodium, and water-chloride (rather than regressing parameters anew for the flexible solvent model). Its use also makes it more likely that the potential parameters I regress will be more useful to others who are inclined to use an established water model.

The solid surfaces described in this chapter were unable to polarize or adjust to the solution charge configuration. As such, they mimic an insulating surface. The

following chapter introduces a method I developed to treat an ideally polarizable metal of arbitrary geometry, thus allowing for efficient simulations of a rough copper surface for instance.

Chapter 4

An Electrode Charge Dynamics Routine

4.1 Introduction

Accurate molecular simulations of an electrochemical interface depend on the quality of intermolecular potentials between species. Prior work has resulted in adequate interaction potentials between species in bulk liquid electrolytes; however, potentials suitable at a metallic interface are less well established. For an intermolecular potential to be applicable for use in large-scale MD simulations, it must be computationally efficient. This chapter focuses on obtaining and using accurate and efficient potentials between solution species and the metal. Two common ways of treating a charged species interacting with a polarizable metal are (1) the image-charge method and (2) the use of pairwise additive interatomic potentials obtained from *ab initio* calculations. Both of these approximations have been used to simulate large atomically discrete systems [22, 71–73].

The image-charge method is based on an analytic solution to Poisson's equation. The method correctly reproduces at long range the Coulombic potential between a point charge and a semi-infinite metallic surface. When a charged particle approaches a conducting surface, it polarizes the surface, resulting in an attractive force. The

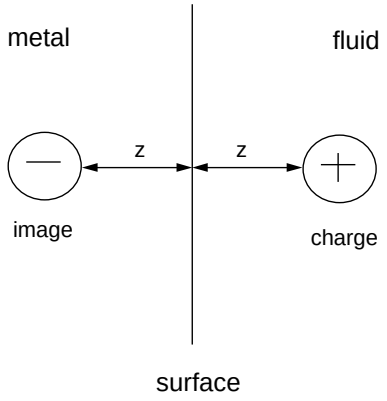

Figure 4.1: Representation of a fictitious image charge in a metal that when Coulombically interacting with the approaching positive charge correctly accounts for the attraction of the positive charge to the polarized metal surface.

induced potential field outside of the metal is mimicked by placing an image point charge beneath the surface of the metal. For a planar interface the image charge magnitude is equal and opposite to the 'real' charge and is equidistant to the interface as represented in Fig. 4.1. In a molecular simulation that uses image charges, all real and image charges interact with each other. However, when the charge is within about 3 Å of the surface, the method overpredicts the strength of interaction and does not resolve important atomic-level details and spatial non-uniformities. For example, the image-charge method predicts the same interaction energy for positive or negative charges, and does not differentiate between surface adsorption sites. Moreover, the method requires the ambiguous selection of the location of the image mirror plane. Spohr and coworkers partially remedy these difficulties by incorporating an additional species-surface inter-atomic potential to account for the surface corrugation [22].

An alternative to the image-charge model is to assume that the potential energy between a molecule and the metal surface is represented well by the interaction between the molecule and a small metal cluster (typically 10-20 metal atoms). The advantage of this method is that the molecule-cluster interaction energy can be

obtained by quantum chemical calculations. In a refinement to this approach, the molecule-cluster interaction is decomposed into pairwise atomic interactions that can then be used for the molecule interacting with the much larger metal surface during a simulation [6, 71]. The primary drawback of this method is that it neglects multi-body charge induction in the metal, that is this model doesn't include the effect of adsorbed molecules influencing the distribution of charge in the metal which in turn influences the adsorption strength of other molecules. These effects will be significant in liquid simulations because of the high density of charges next to the metal. This is in addition to concerns about the assumption that a small metal cluster accurately represents a surface [74].

In addition to the two above highlighted treatments of charge dynamics near a metal surface, Allen et al. [75] and Boda et al. [20] have developed and implemented induced charge computation methods. These recent methods correctly account for the attraction between charged species and a metal surface of arbitrary geometry and thus parallel some of the advantages I claim for this work.

In the sections that follow I present a simple method, termed electrode charge dynamics (ECD), that reproduces the image-charge result at long range and matches quantum-mechanical calculations at short range. ECD is superior to using only pair-wise additive potentials or image charges or a combination thereof as it correctly models both the short-range and long-range contributions to the potential energy and accurately transitions between them (this is verified in Chap. 5.) ECD is also easy to use for irregular surface geometries, an advantage not available to typical image-charge simulations. This chapter resolves the short-range van-der-Waals interactions for species of interest near a Cu (111) metal surface. As will be shown, these short-range van-der-Waals potentials effectively complement the Coulombic interactions found from ECD. In Chapter 5, I validate the method by comparing ECD with

other calculations and give MD simulation results for an aqueous NaCl electrolyte and neat (pure) water next to a planar (111) copper surface.

4.2 Methodology

The electrode charge dynamics method is based on a simple model of charge density in the metal, shown in Fig. 4.2. Metallic conduction-band electrons are free to move in response to Coulombic forces originating within and without the metal, resulting in regions of increased and decreased electron density. I represent the conduction or valence electrons throughout the metal with a diffuse negative charge located at each metal atomic center of variable magnitude q_i^v. A fixed positive point charge q_i^c is co-located at each center to represent the nucleus and core electrons.

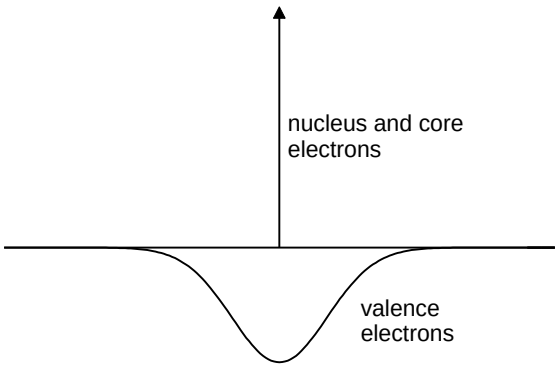

Figure 4.2: Charge on each metal atom. Conduction or valence electrons throughout the metal are represented with a diffuse negative charge located at each metal atomic center of variable magnitude. A fixed positive point charge is co-located at each center to represent the nucleus and core electrons.

Each diffuse charge is modeled with a Gaussian charge-density distribution,

$$\rho_i(r) = q_i^v \gamma_i^3 \pi^{-3/2} exp(-\gamma_i^2 r^2)\,, \tag{4.1}$$

where r is the distance from the atom center and γ_i is an inverse-width parameter. I treat charge mobility in the metal by allowing each diffuse charge magnitude to fluctuate in response to its environment. More specifically, each q_i^v changes so as to minimize the electrostatic energy or equivalently, to equilibrate the chemical potential for q_i^v at each atom. The fluctuation in q_i^v is subject to two constraints. The first constraint is that $q_i^v \leq 0$, corresponding to a limit on the depletion of electron density from a given atom. The second constraint is a fixed total charge Q_{tot} in the simulated metal:

$$\sum_{i=1}^{n} (q_i^v + q_i^c) = Q_{tot}\,. \tag{4.2}$$

where the sum is over all metal atoms.

At this point I note the similarity between this model and the charge equilibration schemes developed by Rappé and Goddard [76] and Rick, Stuart, and Berne [77]. In these models as well as the model developed here, there are two adjustable parameters per unique charge site. In this case, because the metal surface is composed of only one kind of atom, there are only two parameters (here q^c and γ) that characterize the polarization behavior of the metal. The explicit division of the charge into core and valence charges is unique to this work and leads to different behavior for short-range interactions. In particular, this formulation results in a difference in Coulombic interaction energies when a negative versus a positive point charge approaches the surface (detailed in Chap. 5), in agreement with theory. I also note the model's classical resemblance to the quantum-mechanical approximations used by Price and Halley [8].

To obtain the magnitude of the diffuse charge at each electrode atom, I minimize the Coulombic potential energy U of the metal subject to the constraints. This can be done analytically using Lagrange's method of undetermined multipliers. The Lagrangian to be minimized is

$$\mathcal{L} = U - \lambda\left[\sum_{i=1}^{n}(q_i^v + q_i^c) - Q_{tot}\right] - \sum_{i=1}^{n}\mu_i q_i^v, \tag{4.3}$$

where λ and μ_i are undetermined multipliers, and U is the system Coulombic energy.

According to the Kuhn-Tucker conditions for Lagrangian problems with inequality constraints, the solution must satisfy

$$\frac{\partial \mathcal{L}}{\partial q_i^v} = \frac{\partial U}{\partial q_i^v} - \lambda - \mu_i = 0, \tag{4.4}$$

with μ_i positive when q_i^v is not negative or μ_i zero when q_i^v is negative. In this scheme, μ_i acts as a switch to maintain the inequality constraint that q_i^v be negative, and λ corresponds to the total-charge equality constraint (Eq. 4.2). This is a linear minimization problem and can be solved by matrix inversion at each time step throughout the simulation. If there are very many metal atoms, the computational cost of inversion can become excessive. (For a thorough discussion of solving large linear sets of equations see reference [78].) Therefore, I have chosen an alternative implementation.

To avoid the CPU-costly matrix inversion at each step, I treat the diffuse charges as dynamic degrees of freedom that respond to forces that decrease the value of $\mathcal{L}$. This is very similar to the way in which the solution particles seek out the energy minima of phase space. I assign each diffuse charge a fictitious mass m_q, as well as a charge 'velocity' v_i. Each q_i^v is forced down the gradient in the Lagrangian $\mathcal{L}$ while the 'temperature' of the diffuse charges is kept near zero. In this way the diffuse charges in the electrode are efficiently held near the electrostatic energy minimum at a significant computational savings over matrix inversion. Note that the particle

and charge degrees of freedom are coupled as the charge in the metal responds to the structure of the fluid. For this reason separate thermostats must be applied to the particle and charge degrees of freedom in order to maintain them at different temperatures.

The diffuse charge and its velocity are propagated using the following equations of motion:

$$\dot{q}_i^v = v_i - \xi \tag{4.5a}$$

$$\dot{v}_i = \frac{F_i}{m_q} - \zeta v_i, \tag{4.5b}$$

where over-dots indicate time derivatives. ξ, given by

$$\xi = \frac{1}{n\tau}\left[\sum_{j=1}^{n}(q_j^v + q_j^c) - Q_{tot}\right], \tag{4.6}$$

is an additional parameter to correct long-term numerical drift in the total charge of the electrode. τ is a time constant equal to about 100 timesteps. Long-term drift is possible because it is the *derivative* of the total charge constraint that is incorporated into the form of the force F_i on each charge. Because I use the Ewald sum to account for long-range Coulombic interactions, it is important to control charges closely in order to maintain cell neutrality. ζ is an integral-feedback control variable that maintains the average charge temperature at set point $\bar{T}_q$. Using a Nosé-Hoover temperature-control scheme [79], the equation of motion for ζ is

$$\dot{\zeta} = \frac{T_q - \bar{T}_q}{\bar{T}_q \tau^2}, \tag{4.7}$$

where $\bar{T}_q$ is the temperature setpoint. I find that $\bar{T}_q = 5$ K works well. The instantaneous charge temperature is

$$T_q = \frac{m_q}{n k_B} \sum_{j=1}^{n} v_j^2 \,, \tag{4.8}$$

where k_B is Boltzmann's constant. In fact, the choice of mass m_q is tied to the choice of $\bar{T}_q$ and the timestep, in order to maintain numerical stability. I use $m_q = k_B \bar{T}_q (10\,\mathrm{ps}/|e|)^2$.

The force on each valence charge is

$$F_i = -\frac{\partial \mathcal{L}}{\partial q_i^v} = \left(\frac{1}{n} \sum_{j=1}^{n} \phi_j \right) - \phi_i, \tag{4.9}$$

where ϕ_i, the chemical potential for valence charge i, is

$$\phi_i = \frac{\partial U}{\partial q_i^v} - \mu_i. \tag{4.10}$$

Recall that μ_i is the Lagrange multiplier that acts to constrain q_i^v to be negative or zero. This inequality constraint acts like a hard wall for charge degrees of freedom. When using continuous dynamics, a softer repulsion is desirable and so I set

$$\mu_i = -\frac{k_B \bar{T}_q}{Q_\mu} \exp\left(\frac{q_i^v}{Q_\mu} \right), \tag{4.11}$$

which acts as an exponential barrier with $Q_\mu = 0.01\,|e|$ being a stiffness parameter.

To summarize, when charged species approach the electrode, the diffuse charges in the electrode adjust to minimize the energy, or to equilibrate the chemical potential ϕ_i for valence charge at each metal atom. To this point the discussion has focused only on charge-charge interactions that represent gross polarization of the metal conduction-band electrons. In addition to this, electron exchange and correlation effects, manifested at very short range as a Pauli repulsion and at longer range as a dispersion attraction, must be included to properly represent the solution-metal

interaction. I therefore incorporate pairwise van-der-Waals potentials fitted from quantum-mechanical calculations. That procedure is discussed in the next section.

4.2.1 ECD and the Ewald Sum

Before discussing Pauli repulsion and resolved dispersion interactions, I first give more details of the ECD method in the framework of the Ewald sum. Normally large charged systems are of interest where use of the Ewald sum is advantageous, thus I detail the ECD method as used in conjunction with the Ewald sum. Integrating the ECD method into the Ewald framework involves treating the diffuse charges as point charges in Fourier space with appropriate compensation in 'real'-space.

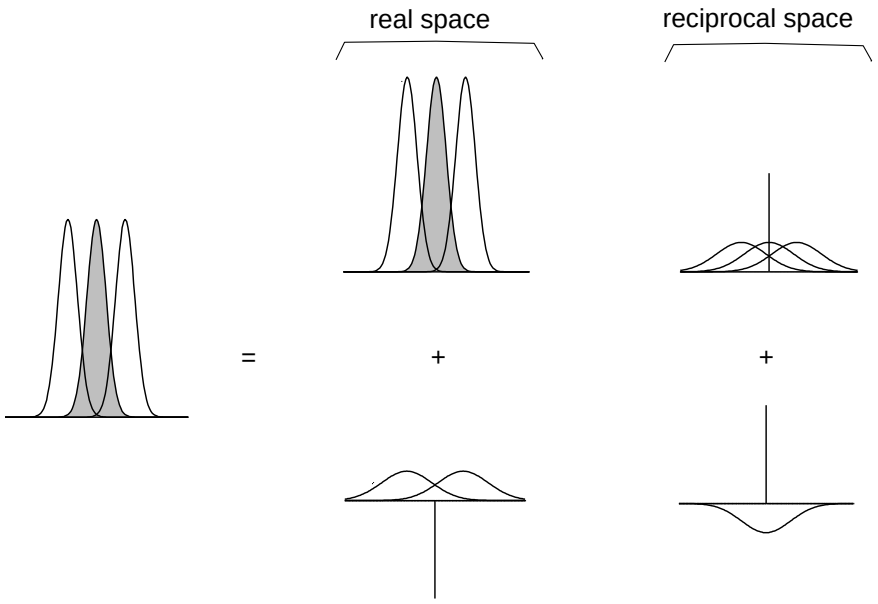

Figure 4.3: Graphic of the splitting of diffuse-charge interactions in the electrode into real and reciprocal space portions. The smaller Gaussian curves represent the screening distributions. In each of the plots, interactions exist between the screening distributions and the point charge or the shaded diffuse charges with the surrounding diffuse charges. The shaded diffuse charges also interact with themselves.

Shown in Figure 4.3 is a graphical sample of the splitting of diffuse-charge interactions in the electrode into real and reciprocal space portions. A screening distribution is added onto the valence-charge distributions to give a rapid decay in the strength of the real-space interactions. The reciprocal space advantageously compensates for what takes place in real space so that the sum of the real- and reciprocal-space interactions give the original at substantial computational savings [24, 80, 81]. Below I give the full system Coulombic energy U and metal atom site potentials ϕ used to simulate the periodic systems of interest.

The real-space system potential energy, U_{real}, including the valence and core metal charges is $U^a_{real} + U^b_{real}$, where U^a_{real} and U^b_{real} are respectively

$$U^a_{real} = \sum_i \sum_{j>i} q^v_i q^v_j C^v_{ij} + (q^v_i q^c_j + q^c_i q^v_j) C^c_{ij} + q^c_i q^c_j \frac{\mathrm{erfc}(\alpha r_{ij})}{r_{ij}}, \tag{4.12}$$

$$U^b_{real} = \sum_i \sum_m q^v_i q_m \frac{\mathrm{erf}(\gamma r_{im}) - \mathrm{erf}(\alpha r_{im})}{r_{im}} + q^c_i q_m \frac{\mathrm{erfc}(\alpha r_{im})}{r_{im}} \quad + \sum_m \sum_{n>m} q_m q_n \frac{\mathrm{erfc}(\alpha r_{mn})}{r_{mn}} \tag{4.13}$$

where the indices i and j belong to the metal atoms and indices m and n refer to solution charges. α is the Ewald convergence parameter. The reciprocal-space energy U_{recip} according to the particle-particle-particle mesh formulation is

$$U_{recip} = \frac{1}{2} \sum_{\mathbf{r}_p \in \mathrm{M}} h^3 \rho_{\mathrm{M}}(\mathbf{r}_p) [\rho_{\mathrm{M}} \star G](\mathbf{r}_p), \tag{4.14}$$

where $\mathbf{r}_p$ is the 3-dimensional mesh positions in real space, h is the spacing between mesh points, and $[\rho_{\mathrm{M}} \star G](\mathbf{r}_p)$ is the finite convolution of the mesh based charged density ρ_{M} with the optimal influence function G [82].

The system Coulombic energy U is

$$U = U_{real} + U_{recip} + U_{self} + \sum_i q_i^v \phi_i^{set}, \qquad \text{where} \tag{4.15}$$

$$U_{self} = -\sum_m q_m^2 \frac{\alpha}{\sqrt{\pi}} + \sum_i (q_i^v)^2 \frac{\gamma/\sqrt{2} - \alpha}{\sqrt{\pi}} + q_i^v q_i^c \frac{2(\gamma - \alpha)}{\sqrt{\pi}} - (q_i^c)^2 \frac{\alpha}{\sqrt{\pi}}, \tag{4.16}$$

and ϕ_i^{set} is a user specified offset potential or voltage that permits a voltage difference to be maintained between two portions of the electrode.

The chemical potential for valence charge i is

$$\phi_i = \phi_i^{set} + \phi_i^{(k)} - \mu_i + \sum_j C_{ij}^v q_j^v + C_{ij}^c q_j^c + \sum_m q_m \frac{\mathrm{erf}(\gamma_i r_{im}) - \mathrm{erf}(\alpha r_{im})}{r_{im}}, \tag{4.17}$$

where $\phi_i^{(k)}$ is the electrostatic potential at i due to the reciprocal space terms and is

$$\phi_i^{(k)} = \sum_{\mathbf{r}_p \in \mathrm{M}} [\rho_{\mathrm{M}} \star G](\mathbf{r}_p) W(\mathbf{r}_i - \mathbf{r}_p), \tag{4.18}$$

where W is a charge assignment function [82]. C_{ij}^v and C_{ij}^c are Coulomb overlap integrals given by

$$C_{ij}^v = \frac{\mathrm{erf}(\gamma_{ij} r_{ij}) - \mathrm{erf}(\alpha r_{ij})}{r_{ij}} \qquad C_{ij}^c = \frac{\mathrm{erf}(\gamma_i r_{ij}) - \mathrm{erf}(\alpha r_{ij})}{r_{ij}}, \tag{4.19}$$

with $\gamma_{ij} = (\gamma_i^{-2} + \gamma_j^{-2})^{-1/2}$.

4.3 ECD Parameter Fit to Cu_{10} *Ab Initio* Data

I have applied the ECD method to a copper (111) electrode surface. This section reports the van der Waals parameters for water, chloride, and sodium ion interacting with a copper surface, in order to supplement the Coulombic interactions from electrode charge dynamics.

It should be clearly understood that in the fitting of the van der Waals potentials, Coulombic ECD interactions were not fit. That is, γ and q^c are characteristic of the metal and not a function of the approaching species. γ and q^c for Cu were chosen to be 0.816 $\mathring{A}^{-1}$ and 1 |e| respectively, based on the following rationales. I chose $q^c = 1\ |e|$ as this results in $q_i^v = -1\ |e|$, on average, corresponding to 1 conduction electron per copper atom. If the electrode, a face-centered-cubic copper crystal with lattice constant $a_o = 3.61496$ Å, is modeled as a free-electron gas with a positive background charge, the Fermi wave vector k_F is equal to 1.36 $\mathring{A}^{-1}$. At the Fermi level the probability that an available electron energy state is occupied is one-half. If I transform the ECD diffuse charge density (Eq. 4.1) to Fourier space and equate the probability that a given wave vector is occupied to the magnitude of the Fourier coefficients, I can relate γ to k_F according to $1/2 = \exp[-k_F^2/(4\gamma^2)]$. The resulting value of γ appears to be reasonable: the overall valence charge density undulates smoothly over the electrode and yet large local charge variations are possible due to the fact that the diffuse charge on each copper is confined mostly to the volume within the Weigner-Seitz radius (1.41 Å) [83].

Ab initio scans (energy *vs.* distance) of molecular and ionic interactions with copper clusters having an exposed (111) plane have been performed to obtain Cu-species interactions. The calculations were performed with GAUSSIAN98 [33] at the MP2 level of theory for a ten-copper-atom (Cu_{10}) cluster interacting respectively with sodium cation, chloride anion, and water. Details can be found in reference [34] on the water-copper scans as well as the split-valence basis set used for copper for all the calculations here. The basis set 6-31+G(d) was used for both sodium and chloride. On-top, bridge, and hollow routes [34] were probed in the case of chloride, whereas only the on-top site was calculated with sodium. In all of the *ab initio* results

presented here, the counter-poise (CP) correction is not included because the basis-set-superposition error (BSSE) is large, particularly for chloride, and the CP method may overcorrect BSSE in the case of metal clusters.

Three parameters were regressed for each site (H, O, Cl^-, and Na^+) interacting with copper atoms by fitting the modified-Morse potential, $U(r) = -\epsilon(1 - \{1 - \exp[-A(r - r^*)]\}^2)$, to the difference between the *ab initio* and ECD Coulombic interactions. The SPC/E water geometry and charges [35] are used for ECD calculations and simulations. The resultant modified-Morse parameters and the atomic partial charges are given in Table 4.1.

Table 4.1: Modified-Morse parameters for water, chloride ion, and sodium ion interacting with the Cu metal

	O	H	Cl^-	Na^+
ϵ, kJ/mol	5.000	0.8430	29.42	10.98
A, $\mathring{A}^{-1}$	1.350	1.303	1.409	0.9872
r^*, $\mathring{A}$	2.890	3.302	2.767	3.741
q_{site}, $\lvert e \rvert$	-0.8476	0.4238	-1.000	1.000

Shown in Fig. 4.4 are the *ab initio* data points and the ECD results for Cl^- approaching a Cu_{10} cluster over the on-top, bridge, and hollow sites. The sum of the ECD Coulombic and fitted van der Waals potentials agree very well with the *ab initio* results in both the repulsive and attractive regions (such agreement is not guaranteed even with three adjustable parameters). The agreement is also good for the calculations of Na^+ approaching the on-top site of the Cu_{10} cluster.

Fig. 4.5 shows the sum of Coulombic and fitted van der Waals potentials versus the *ab initio* data for three orientations of water approaching the Cu_{10} cluster. Nine

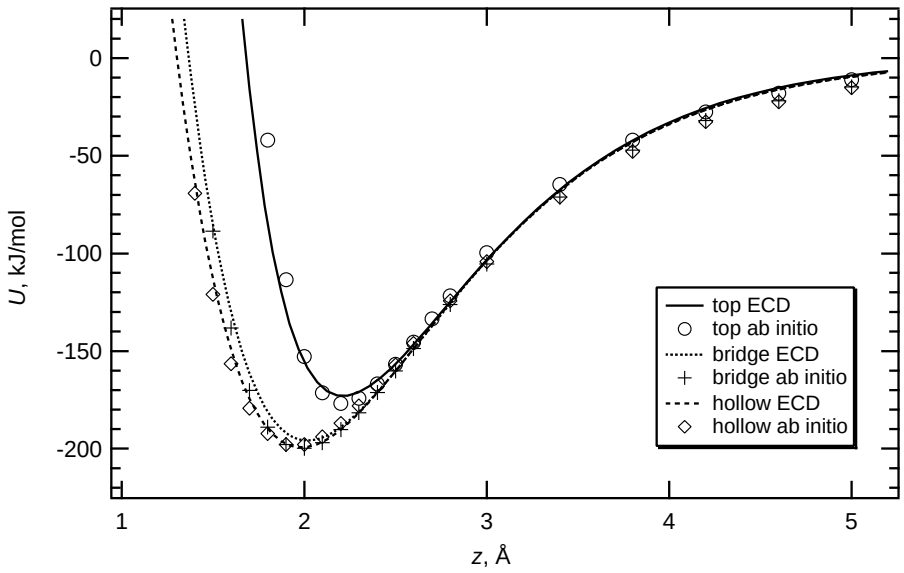

Figure 4.4: ECD and *ab initio* potential energy as a function of distance from the Cu_{10} (111) plane for Cl^-.

unique routes were calculated, but only three representative routes are shown. Fig. 4.5 (a), (b), and (c) represent the average, best, and worst fits, respectively, of the model to the water-Cu_{10} potential scans. The disagreement between the ECD and *ab initio* results may be due to a slightly different water geometry between the *ab initio* and ECD potential scans. The SPC/E water geometry was used to fit the *ab initio* scans as SPC/E water will be used as the solvent in the simulations. While the fits are not as good with water as with the ions, the ECD routine combined with a van der Waals potential satisfactorily reproduces the *ab initio* data.

Of the nine routes (hydrogens up, down, and parallel approaching the on-top, bridge, and hollow sites), the hydrogens parallel over the on-top site is the most energetically favorable as predicted by the *ab initio* uncorrected MP2 results [34]. Due to slight differences when fitting the quantum-mechanical results, the ECD result gives the most favorable route as the hydrogens parallel over the bridge site. Both the

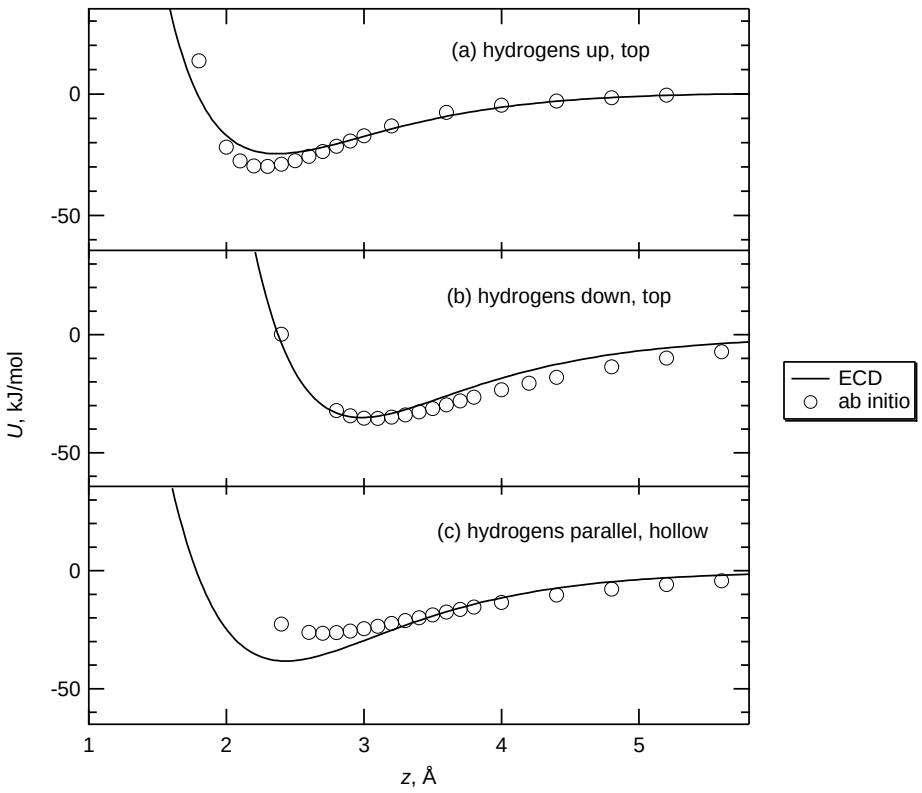

Figure 4.5: Interaction energy of several water approaches toward a 10 atom copper cluster. Distances are measured from the oxygen normal to the copper centers on the uppermost Cu(111) layer.

ab initio results and ECD fit predict that water adsorbs with the hydrogens parrallel to the copper surface in agreement with recent DFT calculations on platinum [84] and silver [85]. Authors of both studies state that the high-energy p atomic orbital on the oxygen originating from the lone pairs interacts most strongly with the metal surface. The p orbital's highest density is lateral to the plane containing the oxygen and two hydrogens.

4.4 Conclusion

I have developed a simple and robust method (ECD) to treat the charge mobility in a metal for use in molecular dynamics simulations. The electrode charge dynamics method is not limited to planar geometries and can easily be modified to treat, for example, the charge mobility in molecules subject to polarizability constraints. The ECD fit of the water, sodium, and chloride ion agree well with the short-range *ab initio* potential scans. In the next chapter I validate the ECD method and give predictions of the interaction of water, sodium, and chloride with larger metal cluster sizes. I also give details and simulation results of an electrochemical interface near a copper surface.

Chapter 5

ECD Validation, Predictions, and Interfacial Simulations

5.1 Introduction

Increased understanding of the interface between metals and liquid solutions (*i.e.* the electrochemical interface) is vital for the design and improvement of catalytic, corrosive, and electrochemical systems. The configuration of liquid species at the interface is intimately connected with mechanistic pathways of ion adsorption, metal dissolution, and metal deposition. Atomically detailed simulation techniques such as molecular dynamics have yielded insight into these kinds of problems. Simulations have been used to predict adsorbed water orientation, ionic distributions, ionic transport coefficients, atomically resolved electrostatic potential profiles, and interfacial differential capacitances [6, 15–19]. The ECD method increases the efficiency of metal-solution interfacial simulations as shown in this chapter.

Chapter 4 showed that the ECD model for copper correlates reasonably well the quantum-mechanical interaction potentials of Na^+, Cl^-, and water with a small Cu_{10} cluster. In this chapter I validate the method by comparing ECD results with other calculations, provide predictions of interaction energies with larger copper surfaces, and show molecular dynamics simulation results for an aqueous NaCl electrolyte and

neat water next to a planar (111) copper surface. This work represents a significant advance in molecular simulations of metal-solution interfaces.

5.2 ECD Validation

In essence, I use the ECD method and associated van der Waals potentials as an extrapolation scheme to obtain inexpensive approximate interactions between species and large metal surfaces. This section seeks to validate and test the ECD copper-surface model by comparing its predictions to image-charge results at long range and to larger cluster *ab initio* calculations.

In addition to the Cu_{10} cluster data, *ab initio* scans also have been calculated for a Cu_{18} cluster [86]. I compare the *ab initio* and ECD predicted energies of chloride and sodium ions and water near a Cu_{18} cluster. Additionally, this section shows the comparison between *ab initio* results and ECD predictions of a hydrated sodium ion near the Cu_{10} and Cu_{18} (111) cluster surfaces. ECD reproduces the image-charge result at long range and successfully predicts the *ab initio* energies at the larger cluster size. These results are presented in this section.

5.2.1 ECD and Image Charges

As stated previously, the simple image-charge potential correctly reproduces the energy of a charge interacting with a neutral metal surface or conducting sphere at long range (distances $> \sim 6$ Å). It is not possible to use the ECD method for a true semi-infinite metal. Therefore I compare the ECD model result with the theoretical (image-charge) result for a point charge approaching a conducting sphere (infinite dielectric constant).

In the ECD calculation, a negative and a positive unit charge are separately brought toward a neutral spherical cluster of simulated copper atoms. The distance from the central copper in the spherical cluster to the outer-most copper was less

than 7 Å with 135 copper atoms in the cluster. The nearest neighbor distances in the cluster correspond to the bulk fcc lattice, namely $a_o/\sqrt{2}$. The ECD interaction energy is then compared to the energy of interaction of a point charge q with a neutral sphere of infinite dielectric according to

$$U(r) = -\frac{q^2 a^3}{2r^2(r^2 - a^2)}, \tag{5.1}$$

where a is the sphere radius and r is the distance to the external charge from the center of the sphere.

Fig. 5.1 shows that the predicted ECD Coulombic energy agrees with the image-charge result at $r - a$ distances greater than about 5 Å. Radius a was adjusted until the ECD and image-charge results agreed at the furthest data point from the sphere, resulting in $a = 7.27$, Å. This value is consistent with a cutoff radius that could generate the corresponding cluster of 135 discrete atoms. Shown in the figure is the fact that the ECD routine predicts unique energies for the positive and negative unit charges at close range. Inset in the figure is a representation of the copper cluster when a negative charge is at distance $r - a = 5.73$, Å. Each copper is colored according to its net charge, $q^c + q_i^v$, where red is positive, blue negative, and white is neutral. This demonstrates that the ECD routine correctly generates the interaction of a point charge with a metal surface at long range, and is able to differentiate between positive and negative charges at short range in agreement with *ab initio* predictions.

5.2.2 Cluster-Size Results with ECD

Figure 5.2 shows the *ab initio* results for a Cu_{18} cluster [86] with water (hydrogens up), Cl^-, and Na^+ approaching the on-top site. Due to the large computational expense, only a few points could be calculated. The same level of theory and basis sets were used as in the Cu_{10} cluster calculations. Distances are measured normal from the surface plane of Cu nuclei to the oxygen, chloride, or sodium ion. The

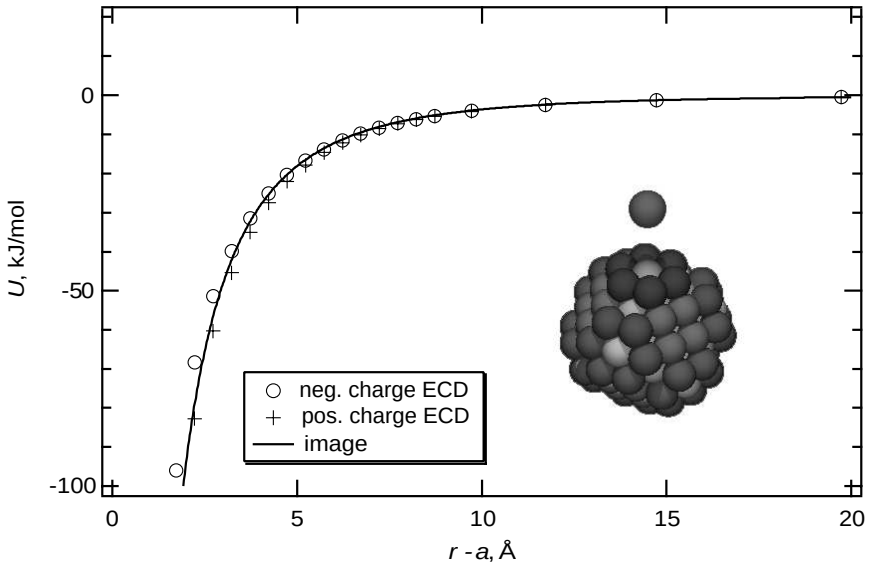

Figure 5.1: Comparison of ECD with image-charge method for a spherical copper cluster of effective radius $a = 7.27$ Å. Inset shows negative charge at position $r - a = 5.73$ Å with cluster atoms shaded according to net charge: black is positive, white is negative, and gray is neutral.

corresponding ECD predictions compare well with the *ab initio* results in terms of relative displacement of the potential from the Cu_{10} results. Note that this is a purely predictive result without any re-parameterization, *i.e.* parameters were fit to Cu_{10} data and then used to predict the Cu_{18} results. I conclude that the ECD model correctly predicts cluster size dependence. The Cu_{10} fits and Cu_{18} predictions are shown together with larger cluster size predictions in the figures in Section 5.3.

5.2.3 ECD and *Ab Initio* Results for Hydrated Na^+ Clusters Near Cu

I have also compared ECD model predictions to *ab initio* results for hydrated Na^+ near a Cu_{10} and Cu_{18} (111) surface, shown in Fig. 5.3. Calculations were performed for sodium only due to computational ease and because the BSSE is much smaller than with chloride.

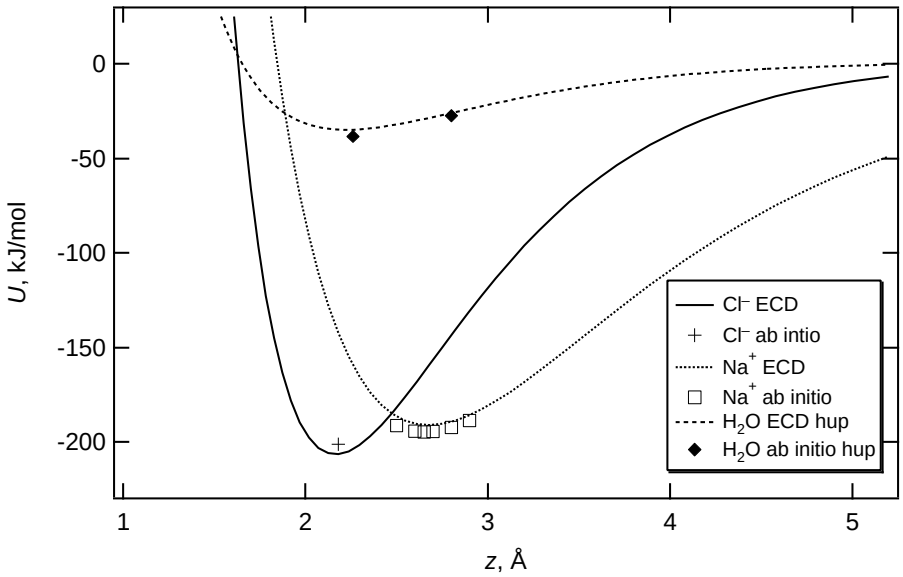

Figure 5.2: Interaction energy of water (hydrogens up), chloride, and sodium approaching the on-top site of a Cu_{18} cluster. This is a purely predictive result without any re-parameterization.

For the Cu_{10} cluster, sodium is hydrated with one to five water molecules. In the case of Cu_{18}, one or two water molecules surround the sodium ion. A. Karttunen and T. Pakkanen calculated the optimum geometry of the system at the Hartree-Fock level and the final energy at the MP2 level of theory [86]. In the geometry optimization, all water molecules were allowed to move freely while Na^+ motion was restricted to the direction normal to the surface. Na^+ was placed directly over an on-top and a hollow site for the Cu_{10} and Cu_{18} clusters respectively. The optimized hydration energy of the isolated sodium-water clusters was also computed. The energies given in Fig. 5.3 are the energies of the hydrated ion near a copper cluster, relative to an isolated copper cluster and isolated sodium-water cluster.

The sodium hydration energy of the ECD and the uncorrected *ab initio* calculations agree within 4% in all cases. This agreement in hydration energies (no surface present) between the *ab initio* and model result indicates the water and sodium model

represent well the cross interactions between H_2O and Na^+. While the energies in the presence of the copper surface for the two techniques compare less well, the ECD model correctly predicts the energetic trend with increasing water. The qualitative change in the ECD curve when 4 and 5 water molecules are present can be ascribed to the fact that 1 and 2 water molecules, respectively, are located between the sodium ion and the metal surface. The *ab initio* geometries show these water molecules to be distorted (HOH bisector angle is $\sim 105°$) from the geometry of the other hydrating water molecules that more closely resemble SPC/E water. The fact that the ECD model does not reproduce this geometry distortion, in addition to discrepancies in the water-copper interaction are the sources of the inaccuracies in Fig. 5.3.

As shown in the figure, the same calculations were performed using the ECD method, but the oxygen (in H_2O) and sodium ion positions were taken from the *ab initio* geometry optimization. I used SPC/E [35] water in the ECD calculations and located the SPC/E hydrogens as close as possible to the *ab initio* hydrogens. For the energy of Na^+ interacting with the water I used the parameters of sodium cation as listed in Table 2.1.

5.3 ECD Predictions

The previous section showed that ECD does reasonably well in predicting energies for situations for which it was not parameterized. This section discusses the ECD predictions of Na^+, Cl^-, and water on the (111) surface of copper clusters with 160 and 430 atoms–cluster sizes that are far from accessible to fully *ab initio* calculations. Additionally, I give the predicted interaction of Na^+, Cl^-, and water with a Cu_8 surface (two layers of 4 copper atoms) where the system (surface and approaching species) are periodically repeated. I also show molecular dynamics simulation results using ECD to simulate pure water and an electrolyte solution between two copper

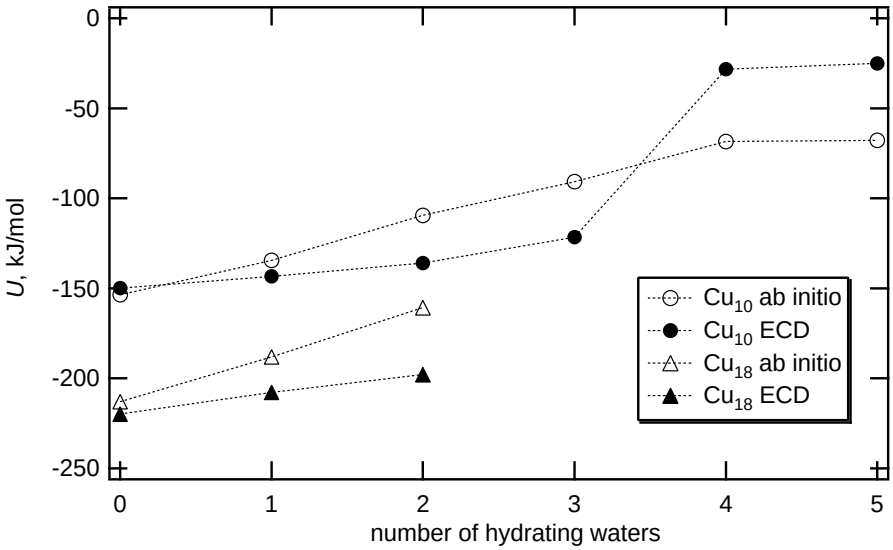

Figure 5.3: MP2 *ab initio* and ECD energies of a hydrated Na^+ atom near copper clusters. The position of the sodium ion relative to the cluster surface is at an optimum position when hydrated. These optimum geometries were found using Hartree-Fock level of theory in the *ab initio* case. The sodium ion is above the on-top and hollow site for Cu_{10} and Cu_{18} respectively.

electrodes. This is to provide insight into the water and ionic structure at the copper surface modeled with the ECD routine.

An advantage of periodically repeating the surface and approaching species is that the edge effects seen in cluster calculations are not present. Also, the periodic system more closely mimics the interaction with a surface. However, because the approaching species is also periodically repeated, the resulting calculations are of an infinite sheet of species interacting with an infinite surface and thus may not accurately reproduce the interaction of a single molecule interacting with a surface.

5.3.1 ECD Large-Cluster Predictions

Shown in Figure 5.4, 5.5, 5.6, and 5.7 are the ECD predicted energies for Na^+, Cl^-, and water with clusters of 160 and 430 atoms. Also shown are the results when the

species interact with a Cu_8 surface with the species and surface periodically repeated. Included in the figures are the Cu_{10} and Cu_{18} ECD and *ab initio* results for reference.

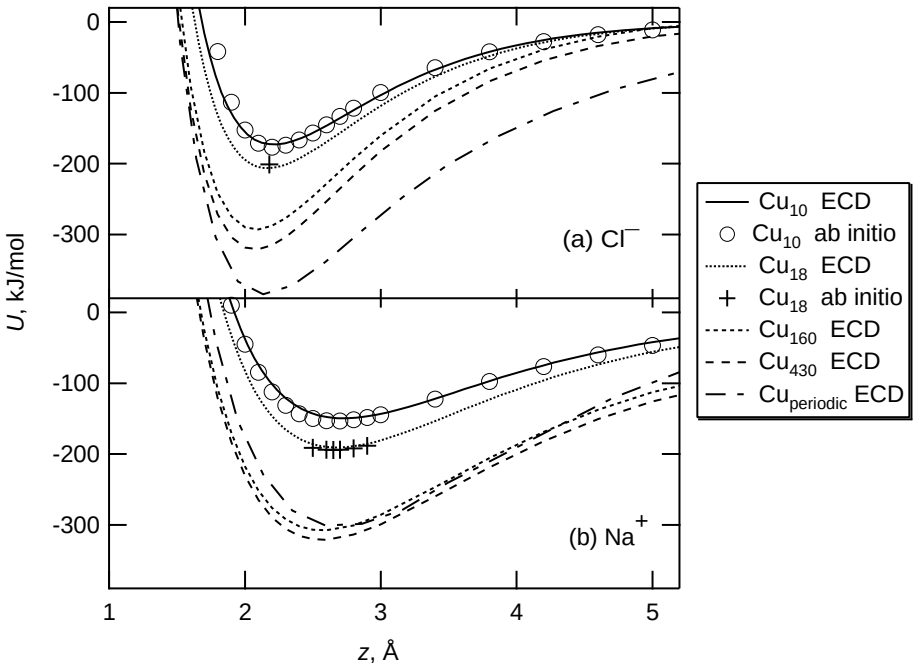

Figure 5.4: Interaction energy of chloride and sodium ion with copper clusters of differing size. The ions approach the on-top site of the (111) plane in all cases.

The Cu_{160} and Cu_{430} clusters are circular-disk in shape and have two metal layers with the (111) plane exposed. At these sizes (and in the periodic case), the interaction energy at the energy minimum is about 60% Coulombic for the ions and about 30% Coulombic for water (hydrogens up, on-top), with the remainder of the energy due to van der Waals site-site interactions. Note that the ECD interaction energy for water converges at a cluster size around 160 atoms while a much larger cluster size is

necessary for the ions. ECD predicts the most favorable water orientation to be hydrogens parallel for the Cu_{10} cluster, but for Cu_{430} there is slightly greater preference for hydrogens up with oxygen over the bridge site.

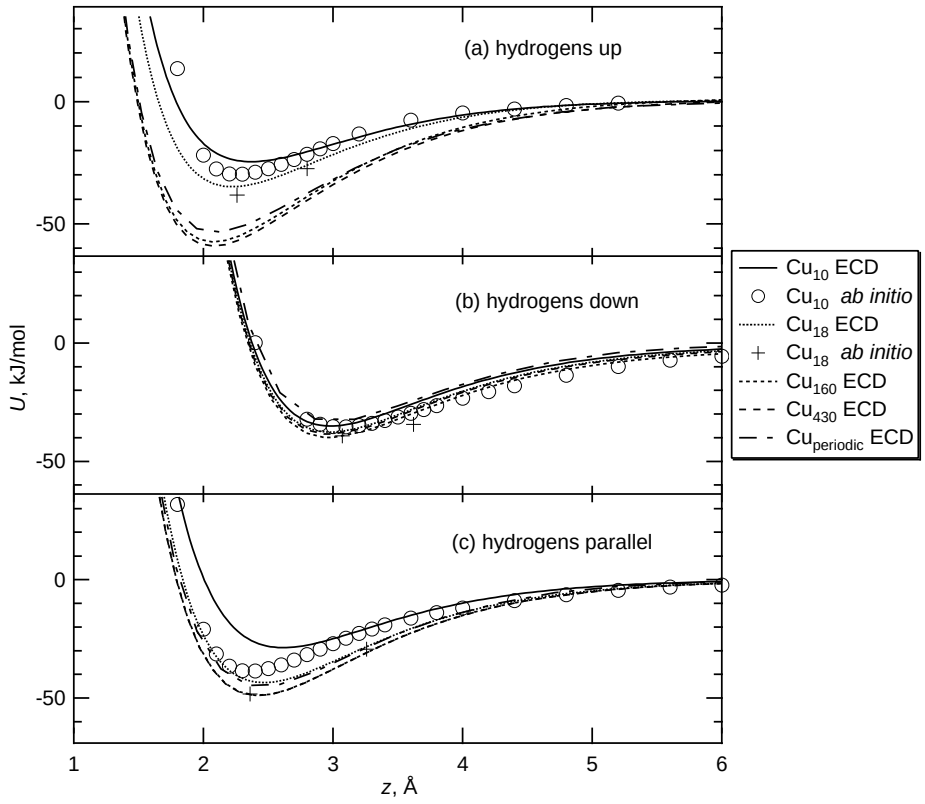

Figure 5.5: Interaction energy of water with copper clusters of differing size for water approaching the **top site**. Distances are measured from the oxygen normal to the copper centers in the exposed (111) plane.

In the periodic case, there are two layers of copper in the unit cell. Each copper layer consists of 4 Cu atoms. The periodic water and sodium energy is shifted closer to the Cu_{10} results relative to the Cu_{430} result. This is expected as there isn't as much charge to polarize relative to the Cu_{430} case. That is, the species coverage

of the surface is much greater for the periodic case (1 species to 4 exposed copper atoms) than for Cu_{430} (1 species for 211 exposed copper atoms). ECD predicts the most favorable water orientation in the periodic case to be hydrogens up at the on-top site. These predictions are consistent with the conventional picture that water chemisorbs to catalytic metal surfaces preferentially through the oxygen. Interestingly, this shift in behavior with cluster size, as predicted by ECD, could help resolve discrepancies between experimental results for extended surfaces and small-cluster *ab initio* calculations.

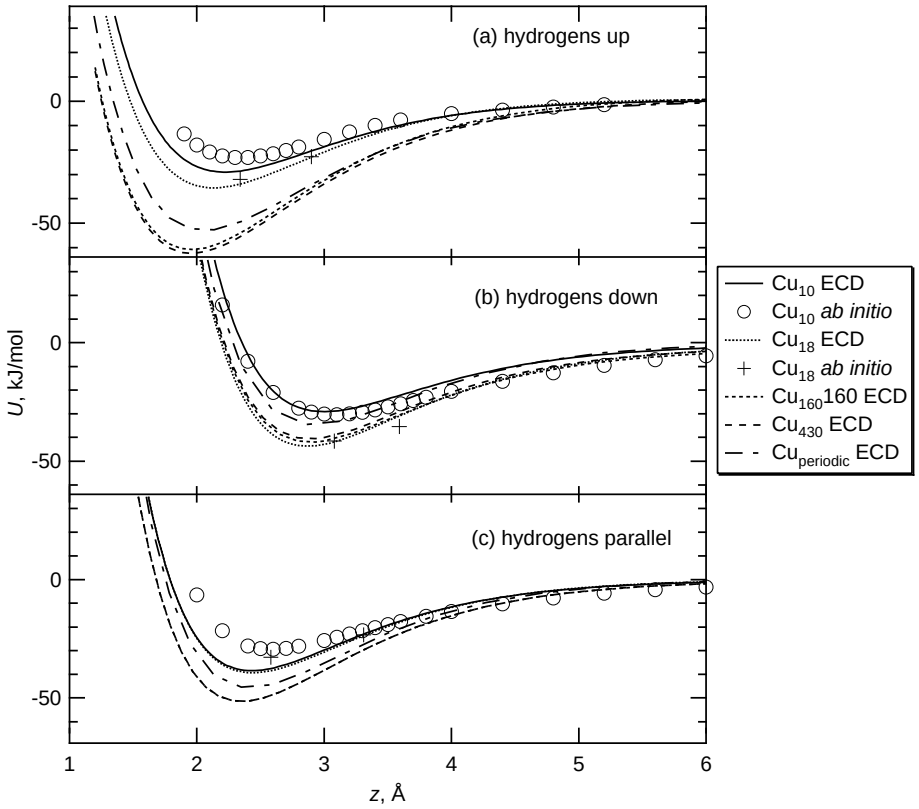

Figure 5.6: Interaction energy of water with copper clusters of differing size for water approaching the **bridge site**. Distances are measured from the oxygen normal to the copper centers in the exposed (111) plane.

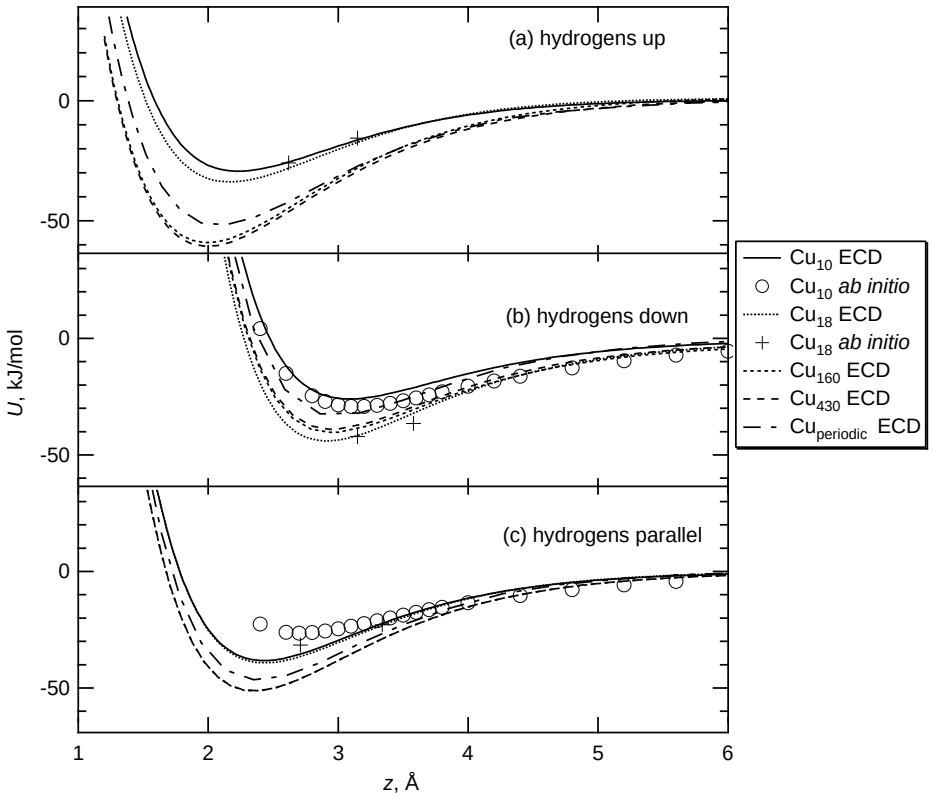

Figure 5.7: Interaction energy of water with copper clusters of differing size for water approaching the **hollow site**. Distances are measured from the oxygen normal to the copper centers in the exposed (111) plane.

5.3.2 MD Simulation Details and Results

The ECD model developed for the copper interface was employed in a series of molecular dynamics simulations to gain insight into the adsorbed water structure on the (111) copper surface as well as the surface sodium and chloride densities.

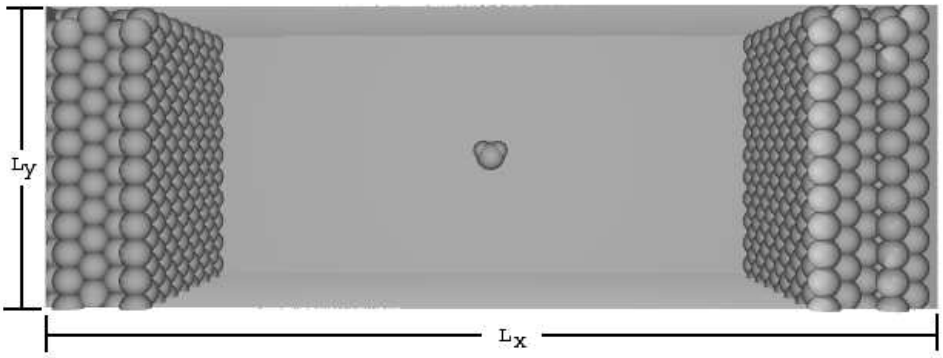

Figure 5.8: 3D representation of simulation cell with metal atoms on both sides and a single water molecule, shown to indicate scale, located in the middle of the fluid region.

Simulation Details

I simulated a sodium-chloride aqueous solution between two copper electrodes at various electric potentials and two different ionic concentrations. The copper electrodes were each 5 layers thick, with the (111) plane exposed. SPC/E water is used as the solvent and the ion-ion and ion-water potentials are given in Table 2.1. The cell dimensions are 97.7, 20.45, and 22.14 Å in the x, y, and z directions, respectively, for simulations with no ions present and 1200 water molecules. Simulations with ions were conducted in a cell of dimensions 101.5, 28.12, 30.99 Å with 80 sodium cations, 80 chloride anions, and 2340 water molecules. Metal atomic positions were fixed during the simulations, with 800 and 1540 total copper atoms for the smaller and larger cell, respectively. Shown in Fig. 5.8 is the larger cell geometry with a representative water molecule shown in the middle of the cell.

In fact, because of periodic boundary conditions, the two electrodes are joined across the boundary and form one metal slab. The offset potential ϕ_{set} in Eq. 4.17 allows us to set the voltage of the two electrode halves at different relative values. In every simulation the total charge on the both electrodes is zero. The total net

charge in the fluid region is also zero. The charges in the electrodes adjust so as to maintain the voltage difference, as well as to respond to local field changes due to the liquid. Because they constitute constant-potential surfaces, the electrodes behave as a Faraday cage. That is, they shield the usual interaction in a 3-D Ewald sum between periodic images of the unit cell in the direction normal to the electrodes. Effectively, I obtain a two-dimensional Ewald sum at no additional cost. Here, the P^3M method due to Hockney and Eastwood [29] is used to perform the Ewald reciprocal sum.

Each simulation run was equilibrated for 50,000 timesteps. Data were collected after equilibration for 200,000 timesteps or 400 ps for each run unless otherwise stated. With no ions present, 5 runs were simulated with 0, 1 and a 5 volt potential difference between the ideally polarizable electrodes (*i.e.*, no reactions are permitted) for a total of 15 runs. For simulations with ions, 6 runs were simulated with 0, 0.5 and a 1 volt potential difference between the electrodes for a total of 18 runs. The density of the water in the middle of the solution-filled region is 54 M for electrolyte simulations and 55 M for neat water. Ion concentrations in the middle of the solution-filled region are around 1.7 M.

Simulation Results

Shown in Fig. 5.9 is a graphical representation of the average charge on the electrode atoms as a function of the electrode layer when there is a 0 and 5 volt electrostatic potential difference between electrodes for water only in the cell. Notice the charge dipole in the metal center (at layers 5 and 6) that is required to generate the potential difference between the two electrode halves. When ions are present in the solution (with a zero potential drop across the fluid) the charge on the surface layers is equivalent to the charge without ions but the standard deviation of that charge is twice as large. The large average standard deviations in copper charges for

the surfaces layers indicate that these layers respond most strongly to the fluctuating electric fields due to the fluid.

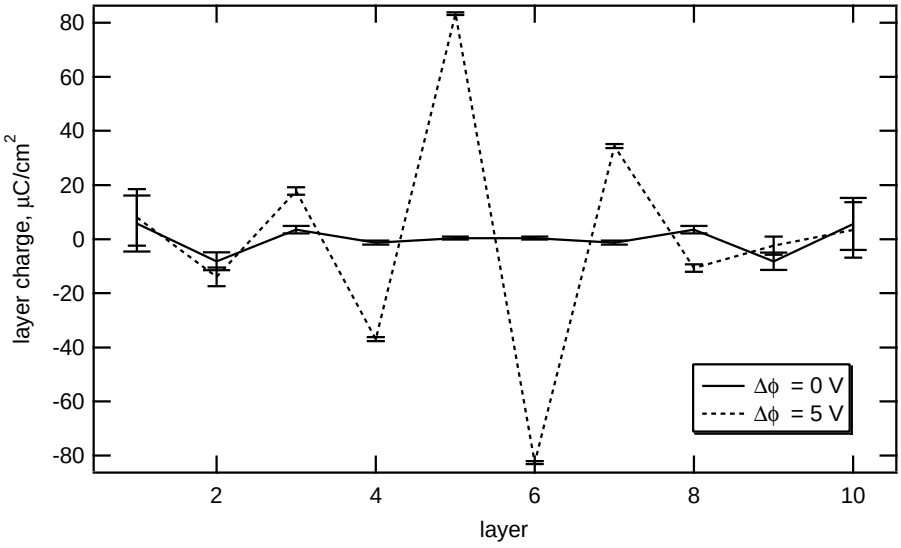

Figure 5.9: Average charge on the copper layers with layer 1 and 10 being the layers exposed to the respective solutions. Error bars show the average of the standard deviation of the charges, with the wider error-bar caps for case $\Delta\phi = 0\,\mathrm{V}$.

Fig. 5.10 shows the oxygen and hydrogen density profiles for water with ions present and with a uniform electrostatic potential across the electrodes. When a 1-volt potential difference is applied across the fluid, resulting changes in the local water density are small and cannot be visibly distinguished. However, the addition of ions to the solution does generate more noticeable differences in the density of the water nearest the surface as the contact-adsorbed ions displace some of the adsorbed water molecules. Such changes are shown in the results given in Chap. 6. As for the ion distributions, notable in Fig. 5.10 are strongly adsorbed chloride and sodium ions on the surface, in nearly equal numbers. There is a second peak for chloride next to the

first; however, with no corresponding sodium peak. The existence of this second peak results in the small amount of excess chloride on the surface of the charge-neutral electrode. As with the water density profile, the ion surface density changes little with imposed voltage between electrodes; most of the change occurs in the diffuse part of the double layer.

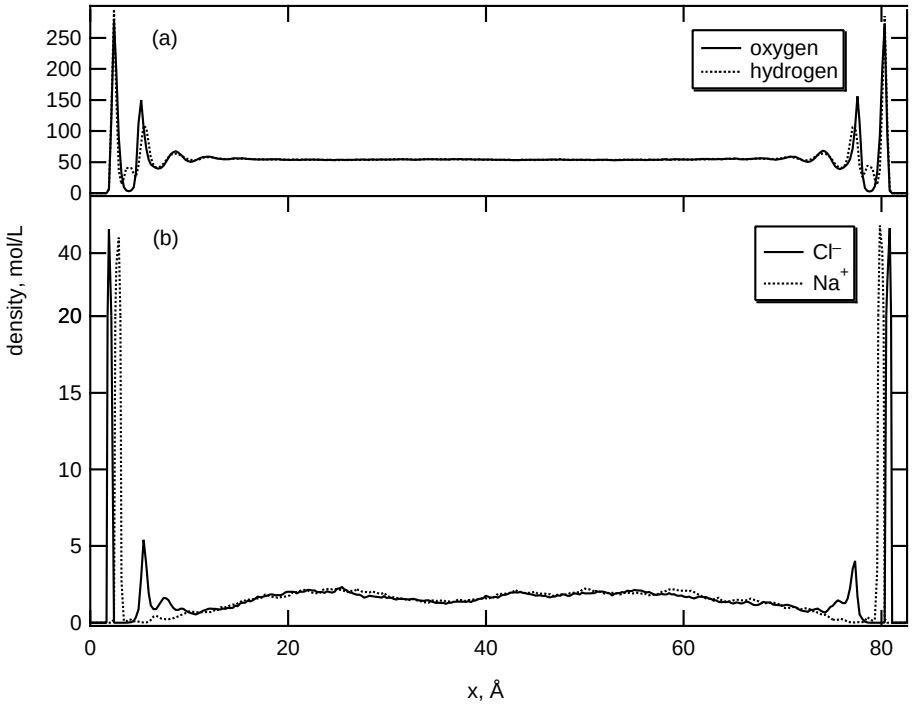

Figure 5.10: Average species density profiles for (a) water sites and (b) ions versus cell position for zero potential difference between the electrodes.

Fig. 5.11 gives the distributions of water dipole orientation in the surface-adsorbed layer (within 3.5 Å of the surface) as indicated by the cosine of the angle between the dipole vector and surface normal. The electrode potential difference is zero. The water molecules closest to the surface are strongly oriented with the dipole moment

parallel to the surface, with a slight hydrogen-up tendency. Although not shown, this distribution is virtually unchanged under a 5 V range of potential difference between the electrodes. To significantly orient the dipole of the water towards the surface would require a very strong electrode charge. As a consequence, the ECD model predicts a much larger barrier to flipping the surface-water dipole than does prior work with a nonpolarizable charged surface [15, 18]. However, the presence of ions in solution is strong enough to create a noticeable disruption to the neat-water dipole distribution.

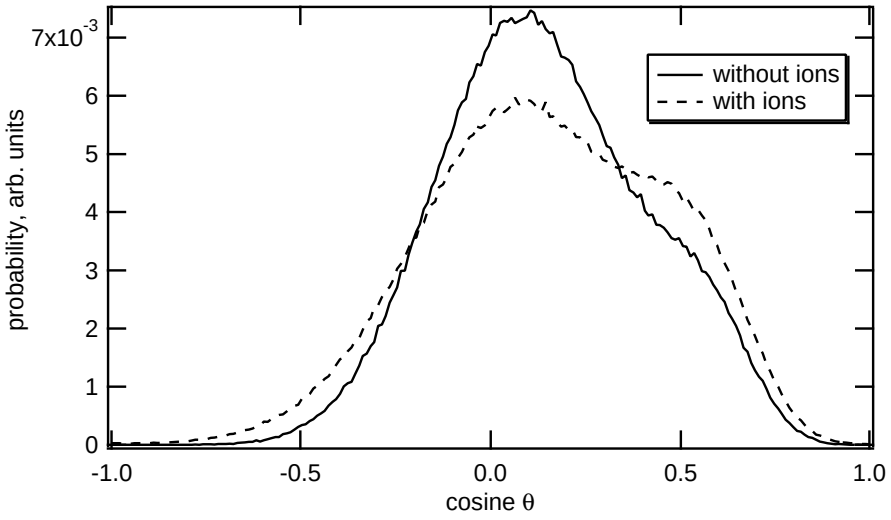

Figure 5.11: Probability of the cosine of the angle between the surface normal and the surface adsorbed (within 3.5 Å of the surface) water dipole moment.

The large surface density for water and narrow dipole distribution indicate that the water is highly structured near the surface. To gain some insight into this phenomenon, I rendered a snapshot of the first and second layers of water next to the

copper surface within a neat water solution. Fig. 5.12 shows a very ordered two-dimensional rhombus ice-like structure in the first layer. Although other interfacial simulations [10, 15, 71] do not see such a pronounced ordering of the surface layer, X-ray spectroscopy and DFT results [87] suggest that the surface adsorbed water forms "flat ice." In the model's ice-like layer here, the oxygen-oxygen nearest neighbor distance is about 2% smaller than the bulk liquid value of 2.79 Å. While there is a mismatch between the surface-water lattice and the underlying copper lattice, it appears that the water molecules somewhat prefer to occupy the bridge and hollow sites. This energetic preference is in agreement with the results obtained by Price and Halley [8].

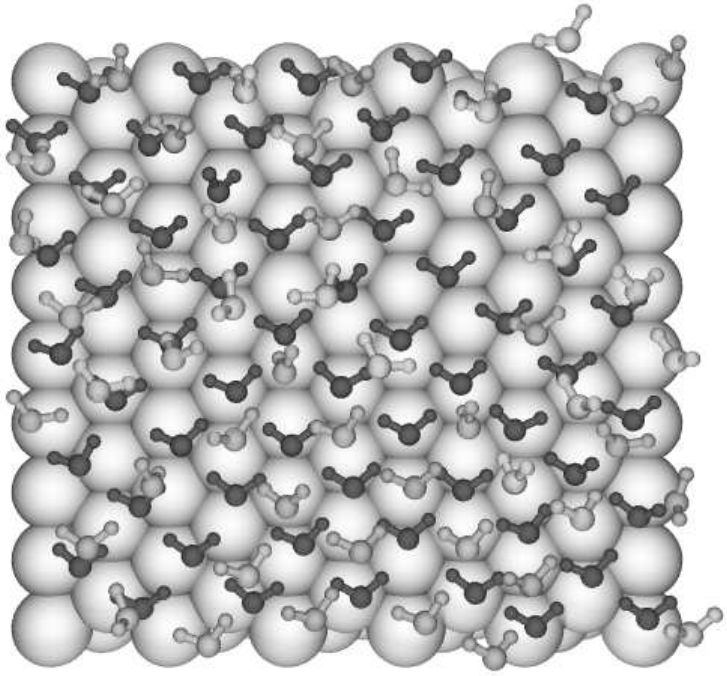

Figure 5.12: Snapshot of the first two water layers on the copper surface for a simulation of neat water. The darker colored water molecules indicate the layer closest to the surface.

Fig. 5.13 is a corresponding snapshot with ions present. Only one layer of adsorbed water and ions is shown. Sodium cations are shown in black and chloride anions are shown in white. As expected, the ions disrupt the regular array of the water near the surface. This is consistent with the ion-induced changes in Fig. 5.11.

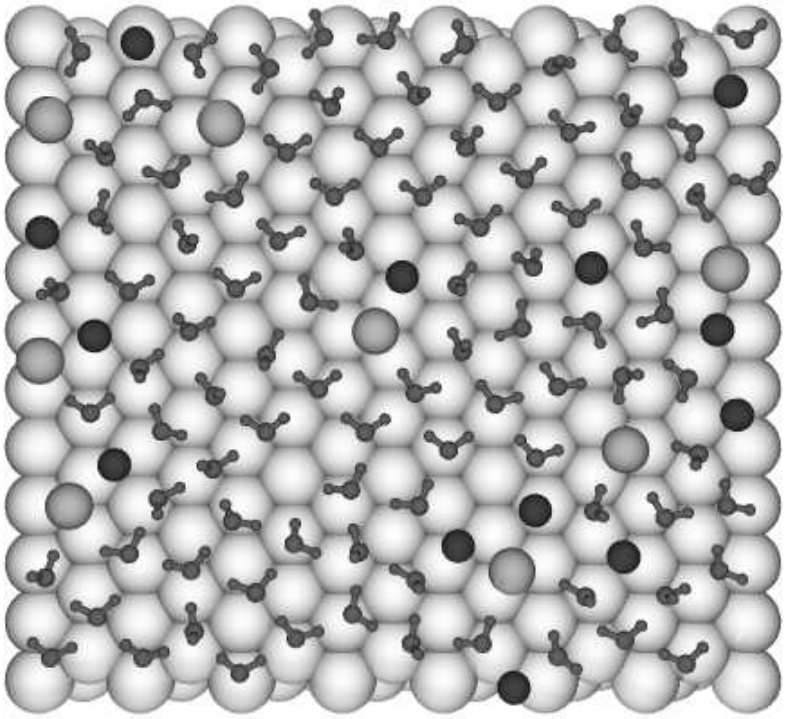

Figure 5.13: Snapshot of the water orientation on the copper surface with ions present. Chloride is shown in white and sodium ion in black.

Shown in Fig. 5.14 are the electrostatic potentials as a function of position, with and without ions present when the electrodes are the same potential. The convex shape of the electrostatic potential profile in the middle of the cell indicates that

there is an excess of sodium ion away from the surface, or a net positive ionic charge in the middle of the fluid ($\nabla^2\phi = -\rho/\epsilon$). Apparently the simulation cell is not large enough to contain the entire diffuse double layer. This is in stark contrast to earlier electrolyte simulations with static surface charges in that the distribution of ions and solvent generates a flat potential profile in the liquid within several Angstroms of the surface [18].

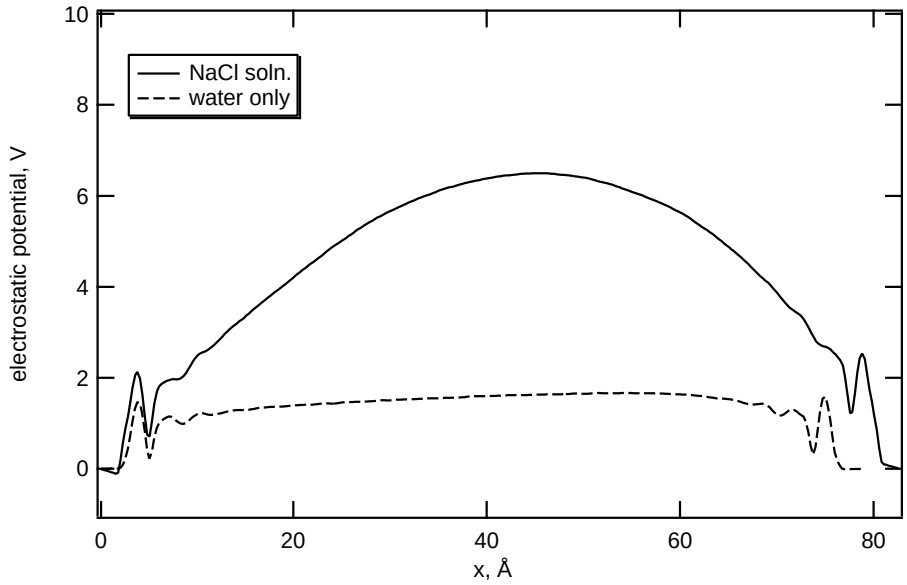

Figure 5.14: Electrostatic potential in the fluid for NaCl solution (solid line) and water only (dotted line). The two systems have different cell lengths which is the reason that the water only plot extends to x = 79 Å whereas the NaCl soln. plot continues to x = 82 Å.

The reader may notice that the average ion densities in Fig. 5.10 and the electrostatic potentials in Fig. 5.14 are not symmetric. This is a manifestation of slow relaxation of the double layer that requires longer simulation times than I used in order to generate the expected symmetry in the average properties. Again, the highly

responsive charges in the electrode for the ECD model tend to stabilize charge separation in the double layer to a much greater degree than has been observed in prior simulation work [18]. For example, with an electrolyte between electrodes at the same potential, the average charge-density difference between the two electrode halves averaged to +0.6 μC/cm^2 over a 2.4-ns simulation.

Because the diffuse region of the double layer is longer than half the length of the fluid-filled region, differential-capacitance calculations of the interface are not reliable. However, I did calculate a cell integral capacitance of 13 and 12 μF/cm^2 for the solutions with and without ions, respectively.

5.4 Conclusion

Electrode charge dynamics acts as a bridge between small-scale *ab initio* metal-cluster calculations and large-scale molecular dynamics simulations of metal surfaces of arbitrary geometry. ECD results of water, sodium ion, and chloride ion interacting with a copper surface agree well with the *ab initio* data. ECD large-cluster-size predictions of water adsorption geometry show trends that are in qualitative agreement with experimental results.

The use of ECD to simulate a water-NaCl solution near copper electrodes has revealed behavior with, in some instances, marked differences from prior simulation work. The simulations show the presence of a dense 2D ice-like rhombus structure of water on the surface that is relatively impervious to perturbation by typical electrode potentials/charges. The model predicts also that sodium and chloride ions are strongly adsorbed to the copper surface at both positive and negative electrode charge, but that there is generally an excess of chloride associated with the surface. Based on the potential profile in the cell, it appears the diffuse part of the double layer extends beyond 40 Å. Further work is required to assess the veracity of the simulations with

regard to double-layer properties and to refine the intermolecular potentials. Nevertheless, the approach described here for treating metal polarizability will permit more accurate representations of the electrochemical interface.

Chapter 6

Simulated $MPSA^-$ Behavior Near a Copper Surface

6.1 Introduction

In 1989, IBM showed that damascene copper plating can be used to fill micro-sized trenches or vias that electrically connect devices on an integrated circuit. In 1997, the first microprocessor using damascene plating technology was produced. This represented a significant advancement in the microelectronics industry as copper is more resistant to electromigration (a problem that leads to device failure) and more conductive than aluminum, the previously used material.

In the damascene plating process, copper is electrically deposited from solution in the presence of organic additives. Organic additives introduced into the deposition bath influence the behavior of the copper ions near the copper surface. Without the presence of the additives, seams or voids in the copper line can form resulting in device failure. Shown in Figure 6.1 are drawings representing cross-sections of trenches filled with electrodeposited copper. The sketch labeled (a) represents a common filling problem when no additives are used. Note the void in the trench that forms. When the appropriate additives are present at their optimal concentrations, copper (shown in gray) completely fills the trench as seen in sketch (b). The formation of a bump over

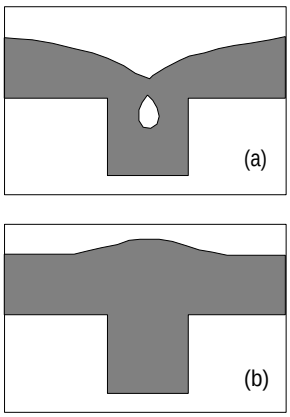

Figure 6.1: Drawings representing trench cross-sections after deposition of copper (shown in gray). Additives are not present in (a), but are present at their optimal concentrations in (b).

the feature indicates the rate of deposition in the bottom of the trench is accelerated relative to the sides or top. This 'bottom-up' filling is also termed 'superfilling.'

It has been postulated that superfilling of the trench results from accumulation of a catalytic or accelerator species in concave areas of the surface [88,89]. The increased accelerator concentration results in an increased deposition rate in the trench bottom and the formation of deposition bumps over the feature. It has also been put forward that the bottom of the trench is less accessible to species that inhibit deposition [90]. This diffusion-based theory can also account for the disparity in deposition rates at the top and bottom of the trench or via. Although additive action can be successfully modeled on a macroscopic scale, atomically resolved details of additive behavior are not known.

Typically, three or four additives are used in the damascene process. Chemicals labeled as accelerators, suppressors, and/or levelers are used to influence and obtain acceptable device interconnects. Bis(sodiumsulfopropyl) disulfide (SPS) in the presence of small quantities of chloride ion has been industrially labeled as an accelerator. A derivative of SPS existing in solution is 3-mercapto-propane-sulfonic acid (MPSA).

There is evidence that complexes of MPSA with cuprous ion $[Cu(I)(S(CH_2)_3SO_3H)_{ad}]$ are the source of the observed acceleration of copper deposition. In superfilling baths containing 3-mercapto-propane-sulfonic acid (MPSA) and chloride ions, MPSA plays an important role in the acceleration of copper electrodeposition [91, 92].

In additive baths where the composition of chloride ion is small (<1ppm), Tan has shown that SPS actually inhibits the rate of copper electrodeposition. When chloride is subsequently added, the rate is accelerated above the initial additive-free value [92]. The next chapter presents similar experimental results that show in the absence of chloride, MPSA also inhibits deposition but then accelerates deposition when chloride is subsequently added. Clearly, the interfacial layer near a copper surface is modified by addition of MPSA or SPS.

In an effort to atomically understand how three or four additives work in concert to cause superfilling, this work first presents evidence through molecular simulation and experiment how MPSA inhibits copper electrodeposition at a molecular level. The work also examines how chloride ion affects the interaction of MPSA with the copper surface. When chloride ions are added to the deposition bath, the orientation of surface adsorbed MPSA may be modified as chloride also adsorbs at the surface and may affect the surface behavior of MPSA directly or indirectly. I give insight into the MPSA behavior with and without chloride present through molecular simulation detailing the adsorption orientation and strength of $MPSA^-$. This work also investigates how changes in the chemical end groups of MPSA affect experimental chronoamperometry and simulation outcomes. Simulation details and results of species adsorption are found in this chapter. Chapter 7 treats the experimental work.

6.2 Simulated Species Adsorption at a Copper Surface

The intent of this work is to use molecular dynamics simulations to obtain the specific behavior of additives at the copper-solution interface and relate that behavior

to describe how MPSA inhibits electrochemical deposition of copper. As a preface to the discussion of these molecular dynamics simulations, it should be stated that I am not simulating the deposition process involving electron transfer events and copper surface incorporation. At a typical current density of 10 mA/cm^2, on average an atomic deposition 'event' occurs only every 180 μs on a 3 nm $\times$ 3 nm surface, whereas herein I report on simulation results that cumulatively last about 0.5 μs. I also don't allow for other reactions such as proton exchange events through the water solvent. The competition between solution species for energetically favorable positions near the surface contributes in large measure to the dynamics and structure of the interface. This competition of solution species for favorable sites may be accurately simulated at the time scales treated in this and other studies [6, 10, 16, 93], though proton and electron transfer effects on the simulated interfacial double layer are of increasing interest [94].

I desire a molecular understanding of how MPSA inhibits and accelerates (in the presence of chloride ion) copper electrodeposition. What are the answers to questions like, "How does chloride-ion addition accelerate the deposition rate?", and "How does chloride ion influence the adsorption or desorption of MPSA?", and "Does sodium chloride addition affect the distribution of copper ions near the sulfonate or thiol chemical groups of MPSA?". Through use of molecular dynamics and the electrode-charge-dynamics routine, this work shows that addition of sodium chloride results in a reduction in the adsorption strength of MPSA near copper surfaces of flat (111) or sawtooth geometry. Through this and other simulated and experimental results, I propose mechanistic details describing some of the actions of MPSA and chloride during electrodeposition of copper.

The behavior of MPSA and electrolyte solution species is recorded near a flat (111) surface of copper. However, during copper electrodeposition, the copper surface isn't exactly flat. Portions of the surface are pointed or indented. Such a rough surface

would disrupt the high-density 2-D solvent structure (Fig. 5.13) at a flat surface. This disruption could affect the surface adsorption of ionic or organic species. I therefore approximate the effect of peaks and troughs that exist on a realistic surface by simulating $MPSA^-$ near a 'sawtooth' surface. Molecular dynamics of such a variable surface geometry has been unavailable to typical image-charge type treatments of the charge dynamics in a metal.

This chapter presents the simulated adsorption results for water, ions, and $MPSA^-$. The adsorption energies calculated from the simulations are presented after the treatment of additional surface interaction potentials. I calculate the adsorption energy of the following ions, Cl^-, Cu^+, and Cu^{2+}. In addition to MPSA adsorption, the adsorption of TPT and $SSPSS^{2-}$ are also calculated. I obtain the adsorption energies from the potential of mean force (PMF) or from an approximation to the PMF, which I call an integrated mean force or IMF. Details of the PMF and IMF are found below.

Prior to reporting on the strength of MPSA adsorption and desorption and other pertinent simulated results, it is necessary to document how I resolve van-der-Waals interactions for copper ions, sulfate ions, and $MPSA^-$ interacting with the copper atoms in the surface. These additional quantum-mechanical calculations are used to parameterize the interatomic interaction with the copper surface atoms and allows for accurate treatment of surface corrugation. These calculations and regressions of potential parameters closely relates to the work discussed in Chap. 4 for water, chloride ion, and sodium ion.

6.2.1 Additional Surface-Interaction Potentials

In this section, the results from *ab initio* cluster calculations of bisulfate, sulfate, $MPSA^-$, and cuprous ions are presented. After presenting the respective potential scans, I give the effective modified-Morse parameters for sulfur, carbon, and oxygen atoms that when coupled with the electrode charge dynamics routine match well

with the *ab initio* copper cluster calculations for the sulfur-containing molecules. Additionally the parameters describing cupric and cuprous ions' interaction with the copper surface are listed. Below I treat each of the species in turn beginning with bisulfate and sulfate ions.

In the *ab initio* results shown in Figures 6.2, 6.3, 6.4, and 6.5 the same level of theory and basis sets were used as in previous cluster calculations. That is I used the MP2 level of theory and a split-valence Relativistic Effective Core Potential basis set augmented with a single set of f-type polarization functions [34, 38] to describe the copper atoms and ions in Gaussian98 [33]. For all other atomic species I used the 6-31+G(d) basis set in calculating interaction potentials. In the following subsections are shown the fits of the *ab initio* results using a modified-Morse potential while treating the dynamic charge distribution in the cluster with the same γ and q_i^c values as detailed in Chap. 4.

Bisulfate and Sulfate Surface Potentials

In Figures 6.2 (b) and 6.3 (b) I present the resultant Cu_{10}-cluster interaction potentials as obtained from first-principle quantum-mechanical calculations for bisulfate and sulfate ions. Two routes of approach were calculated and are labeled and shown pictorially in each figure. In each case the sulfur atom is directly over the top site of the cluster. The *ab initio* data is well represented by the ECD fit.

MPSA$^-$ Surface Potentials

In the case of $MPSA^-$, a methyl thiol and a sulfonate ion (HSO_3^-) approach the copper as they closely resemble the sulfonate and thiol functional groups on $MPSA^-$. The methyl thiol and sulfonate ion molecular approaches are much less costly than the full $MPSA^-$-Cu_{10} cluster calculations. I therefore calculate potential energy scans with methyl thiol and sulfonate ion approaching the copper cluster. I do include

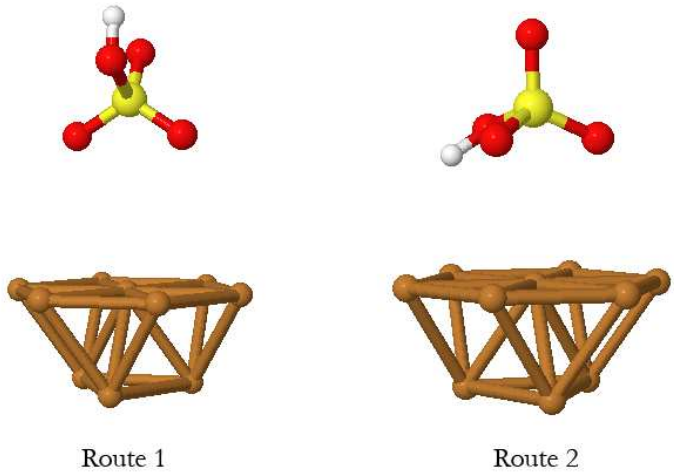

(a) Pictorial representation of bisulfate Cu scans.

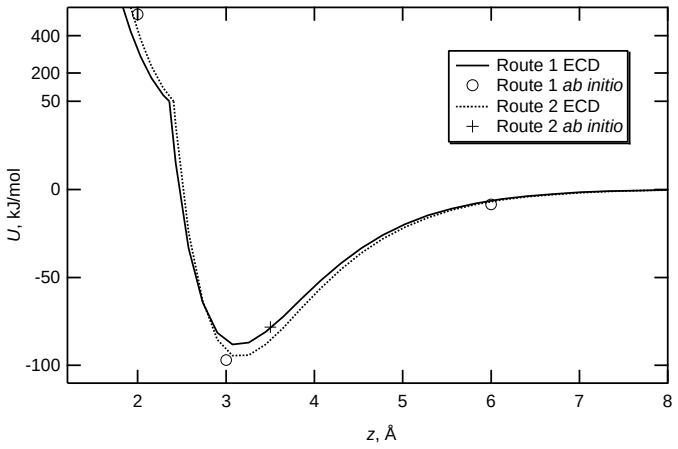

(b) Potential energies of bisulfate approaching a Cu_{10} cluster.

Figure 6.2: Potential energy and representation of bisulfate ion approaching a Cu_{10} cluster. Note that the ordinate changes scale at 50 kJ/mol causing an apparent kink in the potential energies.

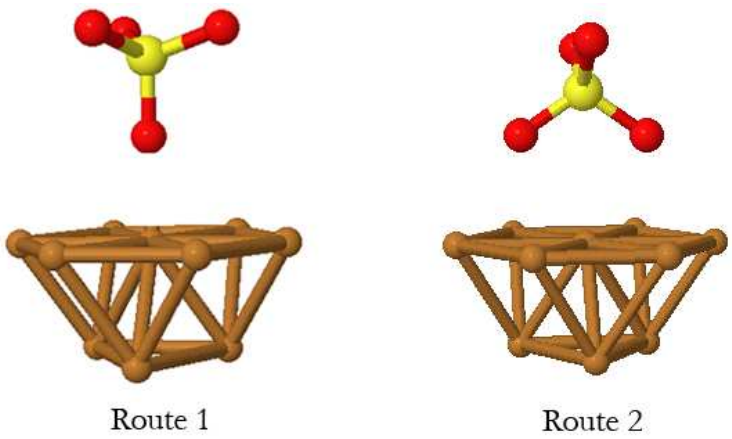

(a) Pictorial representation of sulfate Cu scans.

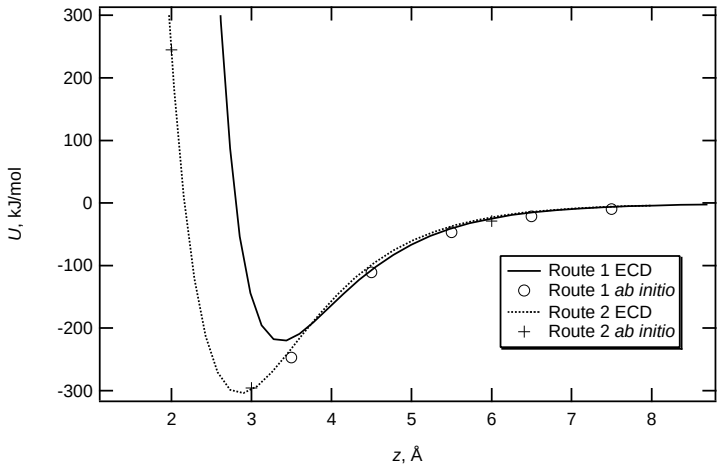

(b) Potential energies of sulfate approaching a Cu_{10} cluster.

Figure 6.3: Potential energy and representation of sulfate ion approaching a Cu_{10} cluster.

a few points with the whole $MPSA^-$ approaching the surface for comparison. In Figure 6.4 (a) are shown pictorial representations of the thiol, sulfonate, and $MPSA^-$ approaches. Not shown is the $MPSA^-$ approach when the thiol group is closest to the surface. Such an approach is equivalent to the methyl thiol approach but with the rest of the $MPSA^-$ included. In each approach a sulfur atom is directly above the top site.

From Figure 6.4 (b) it is apparent that the ECD fit well represents the *ab initio* data. The sulfonate approach is more energetically favored than the thiol approach as the highly charged sulfonate group is closer to the surface. The effect of including the entire $MPSA^-$ molecule is to slightly decrease the *ab initio* interaction energy.

Upon fitting the above scans to a modified-Morse potential for bisulfate, sulfate and $MPSA^-$ I found that I could assign modified-Morse parameters (there are three of them) for sulfur and oxygen atoms independent of where they are molecularly located. For example the sulfur and oxygen atoms in the bisulfate or sulfate or $MPSA^-$ ions could be accurately treated with the same modified-Morse parameters. Such a result speaks to the transferability of atomic van-der-Waals potentials in similar chemical groups within the ECD method.

Cupric and Cuprous Ion Surface Potentials

Figure 6.5 shows the *ab initio* results of a cuprous ion approaching a Cu_{10} cluster. The cuprous ion approaches the top, bridge, and hollow sites of the cluster. The lines on the figure represent the ECD data fit.

The present *ab initio* results for a cuprous ion approaching a Cu_{10} cluster indicate that the potential energy doesn't asymptotically approach zero but rather approaches a maximum at about 6 Å and then diverges at large separation distances (at $z =$ 10 Å the interaction energy of Cu^+ with Cu_{10} over the hollow site is -204 kJ/mol). The increase in *ab initio* binding energy with increasing separation distance is unexpected

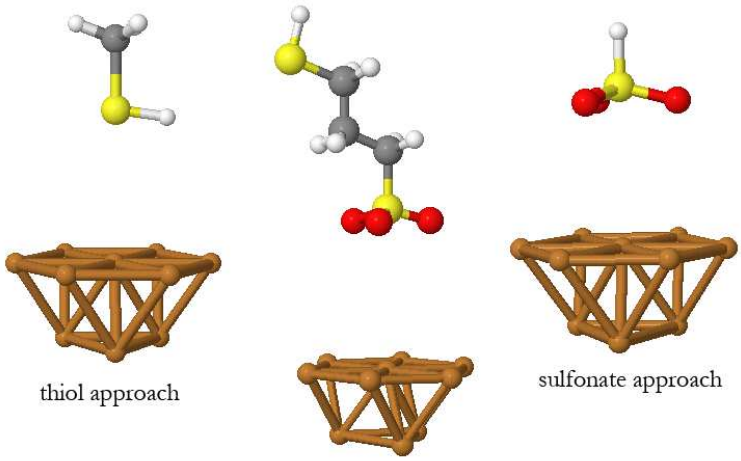

(a) Pictorial representation of $MPSA^-$ and derivatives approaching a Cu cluster.

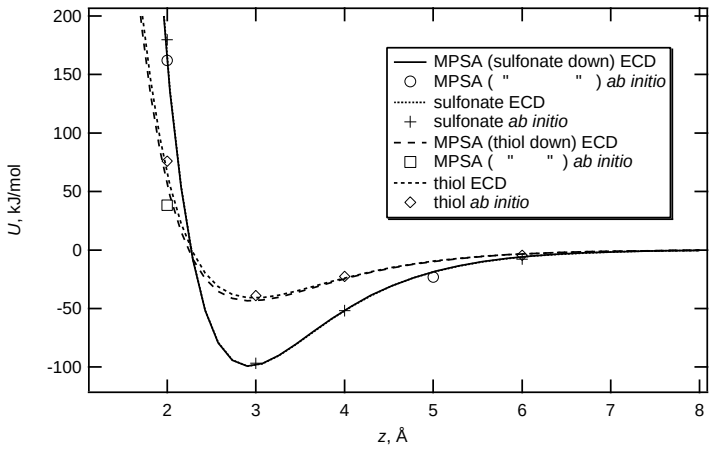

(b) Potential energies of MPSA and derivatives approaching a Cu_{10} cluster.

Figure 6.4: Potential energy and representations of $MPSA^-$ and derivatives approaching a Cu_{10} cluster. In each approach a sulfur atom is directly above the top site.

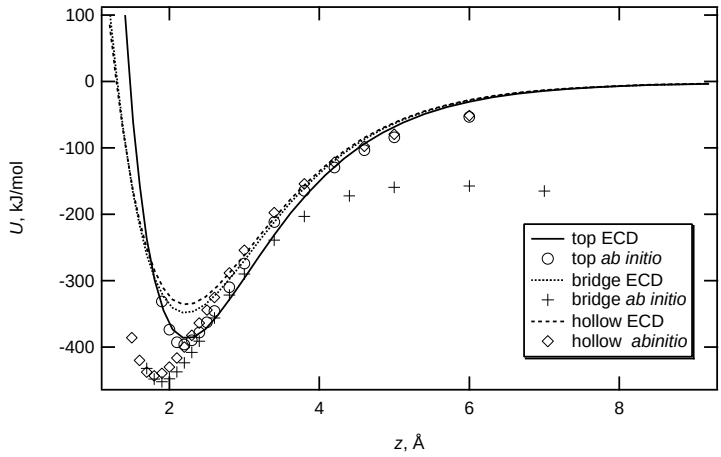

Figure 6.5: Potential energy of cuprous ion approaching a Cu_{10} cluster. The cuprous ion approaches the top, bridge, and hollow sites of the cluster.

and may be due to the inaccurate treatment of the cuprous ion with the basis functions that were used for a copper cluster. Further work is required to establish an accurate representation of the potential energy of Cu^+ and Cu^{2+} species interacting with a copper surface. Near the surface these *ab initio* results can serve as an approximation until more accurate methods and/or potentials are reported. The fitted ECD results do not diverge at large separation distances.

I summarize the above ECD data fit by presenting the modified-Morse potential parameters in Table 6.1. The parameters for Cl^-, Na^+ and water are given in Table 4.1. In the above regression I set the modified-Morse parameters (describing the interaction with the copper atoms) of a hydrogen atom bonded to a sulfur atom to the modified-Morse parameter values of hydrogen in a water molecule (Table 4.1). As the interaction of $MPSA^-$ with the copper surface is largely determined by the site charges, this assumption doesn't significantly affect the quality of fit. The charges on the approaching species are at the previously reported values in Chap. 2. As I had difficulty in obtaining *ab initio* potential energy scans for systems with non-singular

multiplicity (unpaired electrons), I assign the same cuprous-ion copper lattice atom potential to the cupric copper-lattice interaction as an approximation.

Table 6.1: Additional modified-Morse Cu-metal interaction parameters. Parameters for the other species (Cl^-, Na^+ and water) are given in Table 4.1.

	Cu ions	S	O_s[†]	CH_x
ϵ, kJ/mol	40.0	6.0	3.1	2.0
A, $Å^{-1}$	1.0	1.1	1.35	1.3
r^*, Å	3.1	3.5	3.2	3.2

[†] oxygen atoms bonded to a sulfur atom

6.2.2 Simulation Details

Here I give the details of the molecular dynamics simulations used to obtain effective adsorption/desorption profiles of several species approaching the copper (111) surface (flat or saw-toothed) with and without sodium and chloride ions present. In the simulations reported here, 1000 molecules are simulated in a unit cell of approximately 80 × 20 × 22 Å in the x, y, and z directions respectively with 10 (flat) or 11 (sawtooth surface) layers of copper atoms present. Figure 5.8 shows a pictorial representation of the unit cell with flat electrodes. Shown in Figure 6.6 is a representation of the unit cell with a sawtoothed surface.

When simulating an organic additive [MPSA, TPT (1,3-propanedithiol), or SSPSS (1,3-propanedisulfonic acid disodium salt)] near a copper (111) surface, I simulate one molecule of the additive in a water bath of 1000 total molecules. There are 36 bisulfate ions, 12 cupric ions, 12 cuprous ions, and when NaCl is present there are 24 Na^+ and 24 Cl^- ions in the solution. The simulations occur within the canonical ensemble

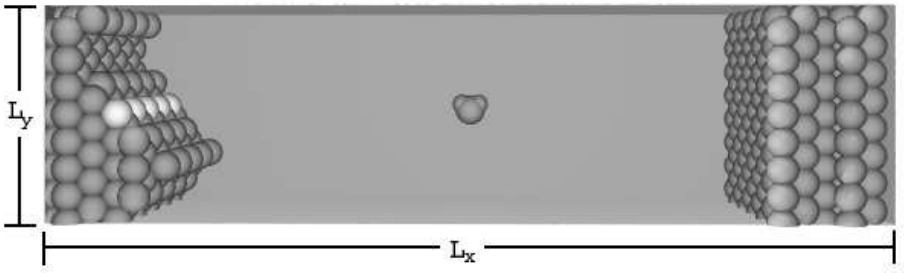

Figure 6.6: 3D representation of simulation cell with sawtooth surface. A single water molecule, shown to indicate scale, is located in the middle of the fluid region. The lightly-shaded surface copper atoms indicate the row at which adsorption/desorption events are recorded.

at a temperature of 298.15K. Each simulation of a forced adsorption and desorption event lasts 1.85 million time steps, with an adsorption/desorption profile being an average of 10-12 unique simulations with timesteps of size 2.0 fs. An electrostatic potential difference of 3.6 V is maintained between the two bounding copper surfaces so that the electrode at which forced adsorption and desorption events occur relate to experimental surface potentials.

I obtain the adsorption profiles of H_2O, Cl^-, Cu^+, Cu^{2+}, and $MPSA^-$ by forcing the molecule or ion toward and then away from the surface. The species begins its forced movement 8 Å from the surface. At discrete locations along its route, the species is held at a given position by artificially imposing a harmonic potential constraint on its location. How the species responds to the constraint is recorded and used to obtain the energy of adsorption or desorption. This is discussed in more detail in Sec. 6.3.1 below.

I equilibrate the system for several (48000) timesteps prior to collection of the adsorption and desorption data. At the beginning of a simulation, prior to forcing a particular species toward and then away from the surface, the molecules in the system

are randomly inserted in an elongated simulation cell. The fluid is then slowly compressed until the density of water in the center third of the fluid reaches 55 mol/L. This compression occurs within the first 20000 timesteps. An additional 28000 timesteps are simulated before data is collected. The molecular site of interest is constrained out away from the copper surface during the compression.

Although the overall ionic concentrations in the simulated solution are in excess of the experimental, this work's intent is to gauge the relative effects of sodium chloride on the adsorption of $MPSA^-$. Additionally, this work explicitly includes the solvent molecules to provide atomically resolved details of the interface. Such inclusion limits the dilution of any particular species to approximately 0.5 M (whereas the experimental additive concentrations are at millimolar concentrations), as more dilute concentrations demand an excessive increase in the number of solvent molecules and simulation time to obtain statistically significant results.

I have chosen to simulate an equal number of cupric and cuprous ions as an approximation to experimental interfacial concentration of Cu^+ and Cu^{2+}. Depending on the rate of copper deposition or dissolution, the interfacial ratio of the number of cupric to cuprous ions will vary.

The molecular interactions that govern the behavior of the simulated interfacial region have been previously discussed and presented. To briefly review, short-range Pauli repulsion and electron correlation effects are modeled with pair-wise-additive Lennard-Jones and modified-Morse potentials for solvent-solvent and solvent-surface interactions respectively. Coulombic interactions are treated within the Ewald framework using the particle-particle-particle-mesh (P^3M) methodology [29, 82, 95]. Short-range interactions are cutoff at 10 Å. Potential parameters for solvent-solvent interactions are detailed in Chapter 2 and those involving the copper surface are discussed above and in Chapter 4. The modified-Morse parameters for TPT and $SSPSS^{2-}$ use

the corresponding $MPSA^-$ values. The charges on the copper surface atoms dynamically adjust to the interfacial structure according to the electrode-charge-dynamics (ECD) routine [13].

6.3 Simulation Results

I find that the presence of sodium chloride in the simulated solution causes a decrease in the adsorption strength of $MPSA^-$. Such a result can relate to the experimentally observed acceleration of copper deposition by NaCl addition to additive containing electrolytes. I also find that the addition of sodium chloride reduces the work required to remove surface electrons. As an increase in the ease of surface-electron removal correlates to a reduction in the activation energy for copper-ion reduction, addition of chloride ions to an electrodeposition bath would increase the deposition rate. The significance of these findings will be discussed following a detailed presentation of the results.

Below I discuss (1) the ionic density near the flat copper surface, (2) the details and results of the energetics of ionic and organic species adsorption and desorption, (3) the distribution of cupric and cuprous ions around $MPSA^-$, and (4) the valence-charge work function of the surface of interest. Quantitative values as well as statistical significances in the difference between values are reported at a 95% confidence interval, unless stated otherwise. The conclusions section discusses how the simulated observations provide insight into possible mechanisms explaining the inhibition and acceleration of copper electrodeposition in the presence of MPSA.

6.3.1 Ionic and Water Profiles and Potential of Mean Force

In the adsorption or desorption of MPSA or other species, the molecule must pass through the double layer where large variations in density occur. I therefore profile the density of the molecular species as a function of its distance from the wall

to understand better the local properties in the interfacial layer. Shown below in Fig. 6.7 are ion and solvent densities near the positively and negatively charged walls without $MPSA^-$ present. The data in the figure represents an average of 18 unique simulation runs each of 500,000 total time steps with 48,000 equilibration steps.

Figure 6.7 shows the ion densities near flat copper (111) surfaces of net charge -0.39±0.03 and 0.53±0.03 $\mu C/cm^2$. These surface charges follow from the 3.6 V difference that I impose on the electrodes. The negative surface corresponds to the experimental working electrode during copper deposition. The centers of the exposed copper atoms are at position $x = 0$ Å. The charged surfaces represent counter electrodes that share the same electrolyte and are separated by 58.5 Å. Also shown in the figures are the water density profiles (normalized by the water density in the middle of the cell). Oxygen and hydrogen density profiles of water are offset vertically to make the graph more readable.

As water is the most abundant surface species, its structure is influential on the adsorption and orientational behavior of the ions and additives. In both Fig. 6.7(a) and 6.7(b), it is apparent that the orientation of the water layer closest to the surface is with the hydrogens parallel to the surface with a slight tipping of the hydrogens toward or away from the surface for negative and positively charged surfaces respectively. The orientation of the water in the second layer is similar for both positive and negative surfaces though the water density in the second layer is significantly reduced in the case of the positive surface. Also, the two high-density oxygen layers are closer to the positively charged surface than to the negative. As a region of low density separates the two water layers, I suspect that water is primarily bound to other water molecules in the same layer while interactions with adjacent layers play a secondary role. Such 2-D water 'sheets' near the solid surface can be seen in Figs. 5.12 and 5.13.

The water plays a significant role in determining the preferred location of ions in the double layer. In both Fig. 6.7(a) and 6.7(b) the second layer of bisulfonate ions

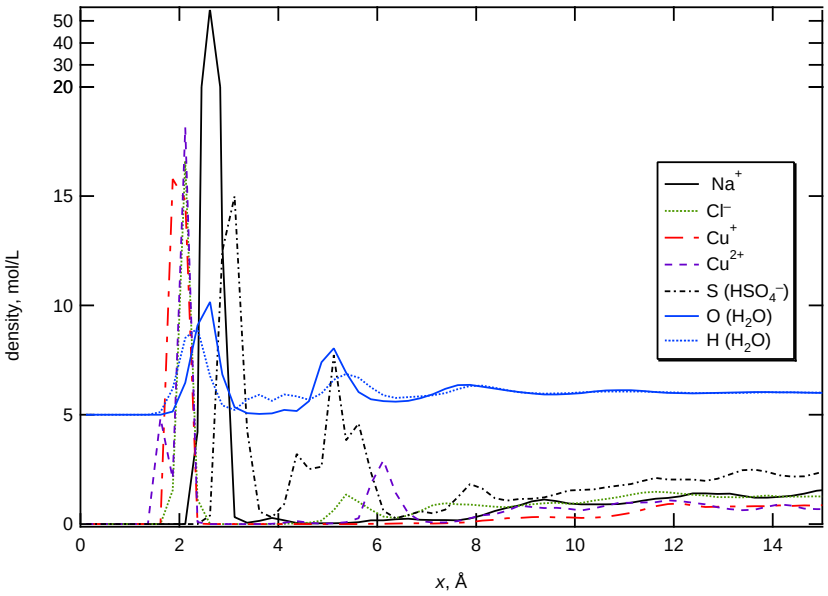

(a) Surface charged at -0.39±0.03 μC/cm^2

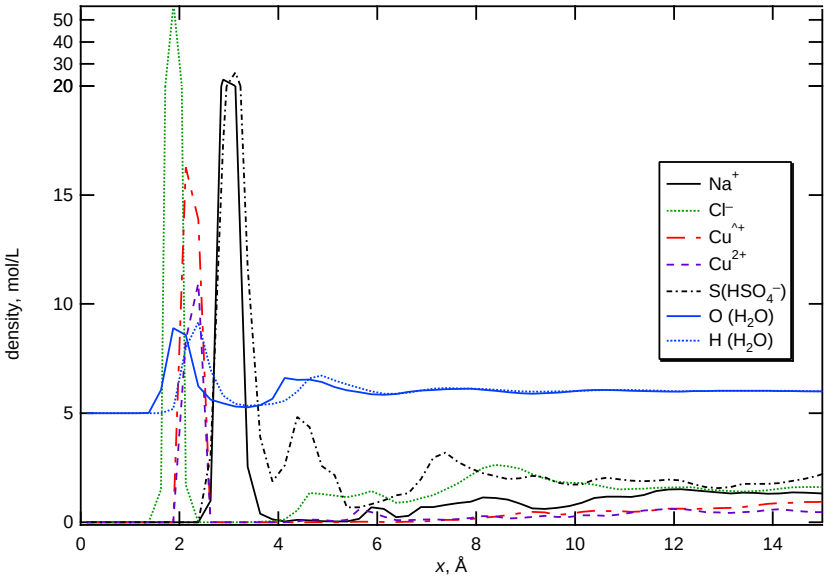

(b) Surface charged at 0.53±0.03 μC/cm^2

Figure 6.7: Density of water and ions near charged Cu(111) surfaces. The charged surfaces share the same electrolyte and are separated by 58.5 Å. The centers of the exposed copper atoms are at zero Å. Also shown in the figure is the water density (normalized by the water density in the middle of the cell). Oxygen and hydrogen density profiles of water are offset vertically for clarity.

is clustered in the second water layer. Also, the most abundant ionic species at the surface (sodium for negatively-charged and chloride for positively charged surfaces) is located at the same position as the first oxygen peak. This suggests that the molecules in the interfacial layer respond together in seeking out a favorable interfacial response to the charge on the surface.

The copper and chloride ion densities near the surfaces show the existence of surface copper-chloride complexes. Near the positively charged surface, the copper ions are Coulombically repulsed resulting in the location of the copper ions pushed out away from the chloride ions. At the negative surface, the chloride and copper peaks coincide.

As the cupric ion is more highly charged than the cuprous ion, it would be expected that the cupric ion would be more abundant at the surface as the Coulombic interactions with the surface are greater for cupric ion. The fact that the less positively charged cuprous ion concentration is equivalent to (at the negative surface) and 50% more prevalent than (at the positive surface) the cupric concentration in the immediate vicinity of the surface indicates that differences in hydration strength strongly influence ionic surface behavior. Thus it is critical to rigorously account for the atomistic details of the solvent especially near the interface.

From the site densities and electrode charge, the electrostatic potential through the fluid can be found using Poisson's equation. Two boundary conditions are needed to solve the second order differential equation: first the potential at a given point is specified and second the difference in the average potential between the two electrodes is known. In Figure 6.8, the electrostatic potential and the gradient of the electric field are shown. The gradient of the electric field is proportional to the charge density in the fluid. The region between $x = -9.4$ to $x = 0$ Å is occupied by the negative electrode; the positive electrode is located between $x = 58.6$ and $x = 68.0$ Å. The fluid region is between $x = 0$ and $x = 58.6$ Å.

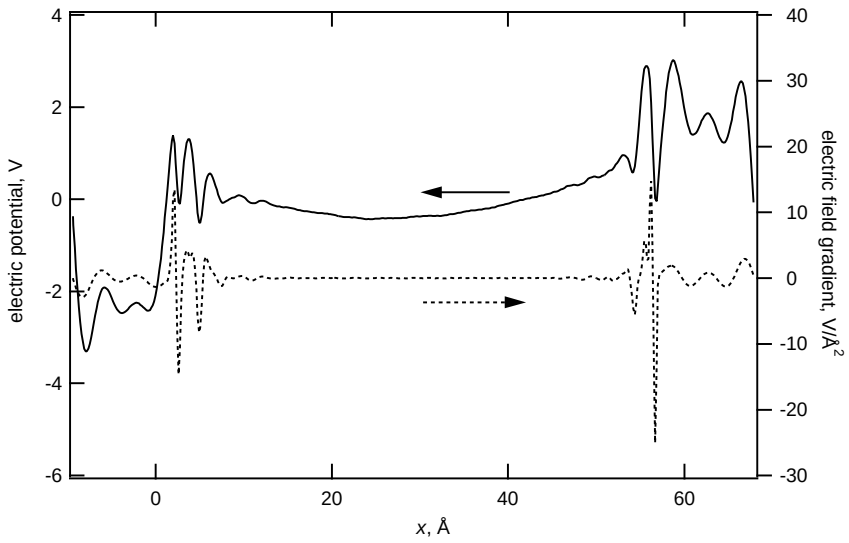

Figure 6.8: Electrostatic potential profile and electric-field gradient profile of the system with charged copper surfaces. The gradient of the electric field is proportional to the charge density in the fluid. The fluid region is between $x = 0$ and $x = 58.6$ Å.

From the solution-charge density that is proportional to the electric-field gradient shown in Fig. 6.8, the reader can see that a positively-charged fluid layer is nearest the negative surface (near $x = 0$ Å) and a negatively-charged fluid layer is nearest the positive surface (near $x = 58.6$ Å). Somewhat unexpected is the 5 charged layers in solution, oscillating from positive to negative, near the negative surface, while there is similarly only 3 such layers of fluid near the positive surface. This outcome correlates with the water density fluctuations near the two unique surfaces, *i.e.* there are more fluctuations in the water density at the negatively charged interface. This observation further shows that the response of water near positively and negatively-charged surfaces is asymmetric, as I (Sec. 3.3.3) and others have previously observed [19].

There is a 3.6 V potential drop between electrodes as seen at the left and right sides of the figure. (The spatial oscillations in the electrode potential are artifacts of

the discrete ECD model and don't accurately reflect the electric potential oscillations in a real metal.) The electric potential is periodic; that is, there isn't a residual electric field propagating through the system. This signifies that the electrodes do indeed behave as a Faraday cage and shield the fluid from effects of 3D periodically repeated slabs of fluid as discussed in Sec. 5.3.2. The electric potential in the middle of the fluid is relatively flat indicating that the solution species properly shield the charge on the electrodes.

When an ion or other species moves toward and adsorbs at the solid-liquid interface, it must pass through areas of large variations in electric field and density. Perhaps the interfacial layer should be called a barrier layer. Normally reactants have one activation barrier to overcome to become products. From the results shown and discussed above, an ion passing from the solution to the solid surface must overcome multiple barriers. These barriers can be quantified through calculation of the potential of mean force. In cases where the distribution of ions relative to a surface is well known, the effective adsorption energy can be computed from the density profile as discussed in the next section. The potential of mean force calculations and other results that follow are calculated at the negative surface as it is the surface where copper is deposited during copper electrodeposition.

Potential-of-Mean-Force Considerations

The reversible work theorem [96] relates density profiles ρ, like those above, to the potential of mean force (PMF) W:

$$W = -RT\ln(\rho/\rho_o), \tag{6.1}$$

where ρ_o is the density at a point of reference. In this case the PMF is a measure of the free energy of adsorption or desorption. Often it is difficult to obtain the PMF

using equilibration methods due to the infrequent sampling in regions of low probability. For instance, obtaining the energy barrier to surface adsorption of chloride is difficult because chloride ions rarely cross that barrier. Due to the simulation size and length, the additives don't sufficiently sample the space near the copper surface. Thus equilibrium methods aren't used to obtain the PMF.

Umbrella sampling is a common method to bias the system to force sampling in low probability areas [24, 97, 98]. Umbrella sampling involves imposing a biased potential, usually harmonic, on the system and recording how the system responds. Here I force the molecule toward and away from the surface by imposing a harmonic potential U_h:

$$U_h = \frac{1}{2} k_h (x - x_o)^2, \tag{6.2}$$

where k_h is the harmonic potential constant equal to 150 kJ/mol, x is the distance from the surface, and x_o is the set-point position. When approaching the sawtooth surface, an additional harmonic potential of constant $k_h/2$, fixes the position in the y direction, so that the site is above the lightly shaded copper atoms in Fig. 6.6. The chosen value of k_h was a compromise: it needs to be large enough that the atom samples the area near x_o, yet not too large that the time step size must be significantly reduced to maintain numerical stability. The species of interest is moved toward and then away from the surface by discretely and sequentially changing x_o. In this way I collect information about the adsorption/desorption energy of organic additives and ions.

Ideally, the solute molecule would be forced to take the same path of adsorption or desorption as naturally occurs in a reversible situation. Any differences between the adsorption and desorption energies indicate that an irreversible path was taken. In order to force the solute molecule to move in a reversible manner, a very detailed understanding of the adsorption pathway must be known *a priori*. Because of the collective structure of the overall fluid and the hydration of the solute molecule, the

set of variables describing the reaction coordinate for adsorption at the surface is large and complex. Thus in an effort to mitigate hysteresis in the adsorption/desorption profiles, I constrain the temperature of the fluid near the solute to 596 K for a short period. The heating of the fluid speeds relaxation of the fluid near the solute and better establishes local equilibrium. The fluid (within 12 Å of the solute molecule) is maintained at this increased temperature for 5000 time steps, beginning immediately upon the resetting of x_o. The elevated-temperature region is then restored to the background temperature. An additional 5000 steps of equilibration are simulated (with the entire fluid thermostated at 298 K) prior to 20000 steps of data collection. From the average position at each x_o value I can obtain the average force (<force> = -k_h(<x> - x_o). Successive values of x_o are separated by 0.2 Å. This averaged force is integrated to give an integrated mean force (IMF) profile for both adsorption and desorption.

Shown in Figure 6.9 is the IMF and PMF of water. The 95% confidence interval for the IMF is shown in gray and the dotted line with the points represents the PMF as found from Eq. 6.1. The IMF and PMF agree within statistical uncertainties. There also isn't a significant difference in the IMF profiles between the adsorption or desorption paths. This indicates that the forced path of approach used to calculate the IMF is reversible. It will be seen that in cases where the size of the approaching species is increased or the hydration energy is significantly greater than that of water, hysteresis is observed in the IMF profiles.

6.3.2 Adsorption and Desorption Energies

I present here the integrated mean force or apparent binding energy of chloride, cuprous, cupric, $SSPSS^{2-}$, and $MPSA^{-}$ ions and TPT near the simulated negatively-charged copper surface. In the case of $SSPSS^{2-}$, $MPSA^{-}$, and TPT I set the harmonic potential to act on either the sulfur belonging to the thiol group or the sulfur belonging

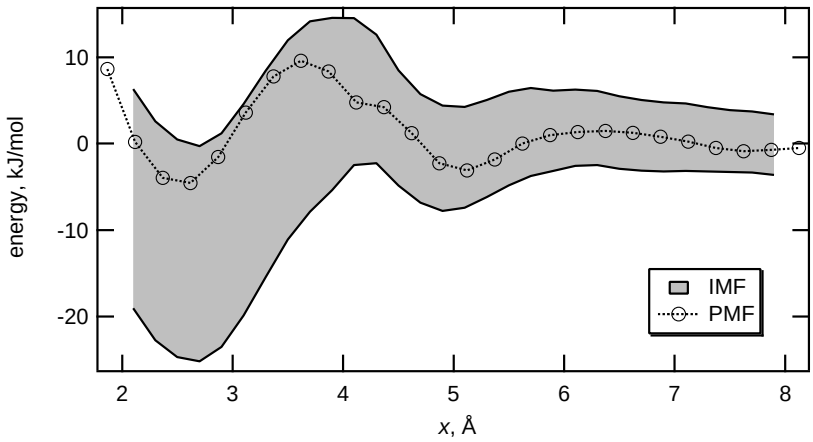

Figure 6.9: Potential of mean force and integrated mean force of water at a flat copper (111) surface in the presence of sodium, chloride, copper, and bisulfate ions. The 95% confidence interval for the IMF is shown in gray. The line with circles indicates the PMF.

to the sulfonate group. The remainder of the sites are free to adjust and respond accordingly. I begin by first discussing the adsorption/desorption energies of the organic molecules. Discussion of the results for monatomic ions concludes this subsection.

MPSA$^-$ Results

Here I discuss the effects that a few factors have on the adsorption energy of the previously mentioned organic additives. These three factors are (1) sodium chloride presence, (2) surface structure (flat versus a sawtooth surface), and (3) chemical functionality (thiol versus sulfonate adsorption). I show that when sodium chloride is included in the bath, the organic adsorption energy is reduced by $\sim$10 kJ/mol. I also find that the organic adsorption energies aren't significantly different (at 95% confidence) with a change in surface structure or when the thiol versus the sulfonate approaches the surface. Below, the results of the 28 IMF scans are summarized followed by a discussion of the significance of the results.

Table 6.2: Adsorption energies (kJ/mol) of thiol or sulfonate sites of $MPSA^-$, TPT, and $SSPSS^{2-}$ in their forced movement toward or away from the flat or sawtooth surface, with (NaCl) or without (∅) sodium chloride present. In the cases when the site is forced away from the surface, the minimum in the potential well closest to the surface is reported. For thiol and sulfonate that distance is ∼2.7 and 3.0 Å, respectively. In the routes where the site forcibly approaches the surface, the energy is reported at the same position as in the removal. Uncertainties at the 95% confidence level are in parentheses.

flat surface

	thiol				sulfonate			
	toward		away		toward		away	
	NaCl	∅	NaCl	∅	NaCl	∅	NaCl	∅
$MPSA^-$	10(10)	4(7)	-27(12)	-53(10)	6(21)	-9(19)	-82(19)	-70(18)
TPT	-14(12)	-13(8)	-40(15)	-47(10)	-	-	-	-
$SSPSS^{2-}$	-	-	-	-	69(18)		-75(19)	

sawtooth surface

	thiol				sulfonate			
	toward		away		toward		away	
	NaCl	∅	NaCl	∅	NaCl	∅	NaCl	∅
$MPSA^-$	25(13)	4(14)	-46(16)	-24(16)	33(19)	20(16)	-51(16)	-75(17)
TPT	38(18)	0(12)	-25(15)	-35(12)	-	-	-	-
$SSPSS^{2-}$	-	-	-	-	36(25)		-87(30)	

Rather than reproducing all 28 IMF profiles in graphical format, I summarize the results in Table 6.2 and in Figure 6.10. These results are calculated from the integrated mean force as the potential of mean force is unavailable as there is only one $MPSA^-$ molecule in that system (the molecular dynamics simulations are such that just one solute wouldn't efficiently sample the interfacial fluid structure that is required for an accurate PMF curve). Listed in the table are the adsorption energies of thiol or sulfonate sites of $MPSA^-$, TPT, and $SSPSS^{2-}$ in their forced movement toward or away from the flat or sawtooth surface, with (NaCl) or without (∅) sodium chloride present. In the cases when the site is forced away from the surface, the minimum in the potential well closest to the surface is reported. For thiol and sulfonate that distance is ∼2.7 and 3.0 Å, respectively. In the routes where the site forcibly approaches the surface, the energy is reported at the same position as in the removal. Each square in Table 6.2 contains data collected over some 18 million simulated steps.

If the toward and away routes are averaged to approximate the reversible binding case, the most favorable circumstance is when $MPSA^-$ is near the flat surface when sodium chloride ions aren't present. The IMF of this instance is shown in Figure 6.10. Also shown in the figure is the approach and removal of TPT near a flat surface in the presence of NaCl. These curves are representative of the other 24 adsorption/desorption profiles.

In all of the cases (with and without NaCl present, near a flat or a sawtooth surface, or when thiol versus sulfonate is forced to and away from the surface), there is a statistically significant difference between the profiles when the site is forced to approach the surface versus being forced away from it. This hysteresis effect is greater for sulfonate scans, but on average there is a -67±21 kJ/mol difference. As mentioned, prior to collection of data reported here, I reduced the speed at which the site approaches or is removed from the surface and briefly heat the fluid surrounding

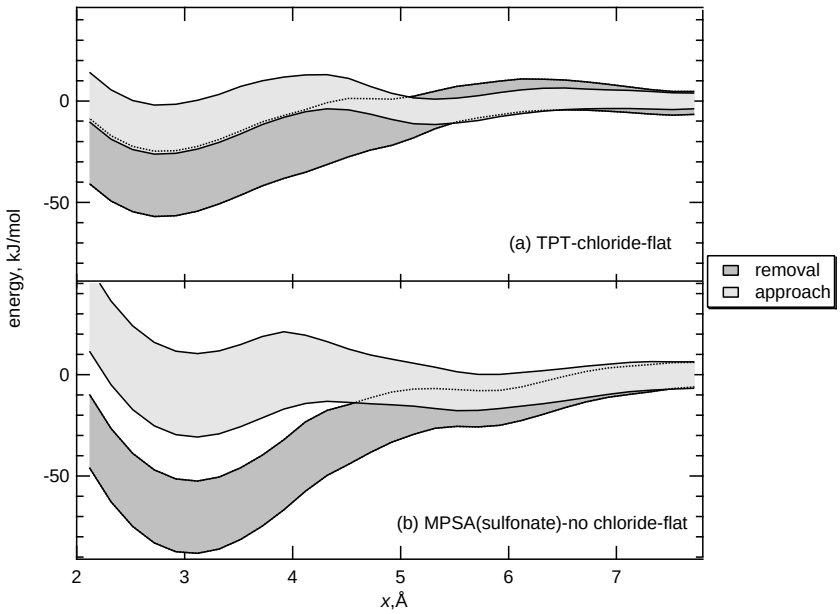

Figure 6.10: Integrated mean force profiles for (a) TPT near a flat surface in the presence of NaCl and (b) $MPSA^-$ near the flat surface when sodium chloride ions aren't present. The width of the curves represent a 95% confidence interval about the mean.

the site. These efforts resulted in a reduction of the observed hysteresis. A significantly longer simulation time would be required to achieve a completely reversible situation. The climbing-image nudged-elastic-band method of Henkelman *et al.* [98] appears to facilitate the reaching of such a fully reversible situation. Despite some hysteresis observed in the adsorption results, the effects of sodium chloride addition on adsorption energy can be quantitatively approximated using the integrated mean force profiles of adsorption and desorption.

The adsorption energy of an organic additive studied here ($MPSA^-$, TPT, and $SSPSS^{2-}$) is -19 ± 8 kJ/mol. There isn't a statistically significant difference between the binding energy of thiol versus sulfonate. Thus the simulations don't resolve which end of $MPSA^-$ prefers to adsorb at a flat or sawtooth copper surface. Experimentally, alkanethiols (such as MPSA or TPT) can form self-assembled monolayers (SAM) on

copper and gold surfaces [99, 100], through the binding of the thiol sulfur to the surface. It may be that the reduction of thiol to a chemically bound sulfide species, a phenomenon not incorporated in my model, strengthens the thiol adsorption energy.

Comparing the binding energies of each route on the flat versus the sawtooth surface (*e.g.* $MPSA^-$ in the presence of NaCl with the thiol forced toward and away from the flat versus rough surface), no statistically significant difference in adsorption energy is observed. When adsorption occurs at the flat surface, the species may favorably interact with the surface as well as the charged fluid layer to enhance the strength of adsorption. Since at the sawtooth surface these distinct fluid layers are disrupted, it may be expected that the adsorption energy would be reduced relative to a flat surface. It may also be that the ions occupy more of the sawtooth surface sites and thus block the adsorption of the organic species. The resolution of the IMF potential profiles is not able to differentiate between these effects.

Including sodium chloride in the simulations causes a reduction in the organic additive binding energy by 10 ± 9 kJ/mol. Thus when including chloride, $MPSA^-$, TPT, or $SSPSS^{2-}$ surface concentrations are reduced at the flat (111) or sawtooth copper surface. This result provides a means to arrive at a mechanistic description of chloride effects in a copper-deposition bath in the presence of MPSA. For instance, as chloride readily occupies surface sites and adsorbs in close proximity to the copper surface (Fig. 6.7(a)), the chloride ions may act as a charge barrier to thiol or sulfonate adsorption as these groups are also negatively charged. Section 6.3.3 discusses the effects that sodium-chloride addition has on the simulated potential of the surface.

The conclusions made in the above three paragraphs were based on comparisons of the adsorption energies at a 95% confidence interval. If that level of confidence is significantly reduced (to 40% confidence), the adsorption at a flat surface is preferred over adsorption at a sawtooth surface by about 10 kJ/mol and sulfonate adsorption is preferred over thiol adsorption also by about 10 kJ/mol.

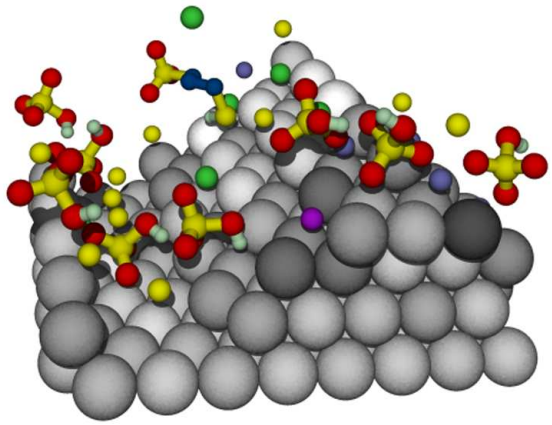

Figure 6.11: Snapshot of $MPSA^-$ near the sawtooth copper surface. Oxygen atoms are colored red, sulfur colored yellow, hydrogen colored white, carbon colored dark blue, sodium colored yellow, chloride colored green, cuprous ions colored light blue, and cupric ions are colored purple. For clarity water isn't shown. The charge on the copper atoms is indicated by the shade of the atoms. Those atoms darkly shaded are negative and lighter shaded atoms are positive; gray is neutral.

Shown in Figure 6.11 is an example snapshot of $MPSA^-$ in a favorable adsorption configuration at a sawtooth surface when sodium chloride is present. Oxygen atoms are colored red, sulfur colored yellow, hydrogen colored white, carbon colored dark blue, sodium colored yellow, chloride colored green, cuprous ions colored light blue, and cupric ions are colored purple. For clarity water isn't shown. The charge on the copper atoms is indicated by the shade of the atoms. Those atoms darkly shaded are negative and lighter shaded atoms are positive; gray is neutral. Note that the chloride atoms induce areas of net positive charge and the cupric ion induces a net negative area of charge at the surface.

Chloride and Copper-Ion Results

Previously it was shown that the water IMF agreed with the water PMF. In the case of copper and chloride ions, the IMF over-predicts the binding energy. The

calculated binding energy for chloride ion is 140 kJ/mol at 2 Å from the surface. If the IMF binding energy is used to estimate the chloride ion surface density (found from the reversible work function), the expected surface density of chloride would be on the order of 10^{17} mol/L. That correlates to a chloride surface atomic density of about 10^{14} atoms/Å^2, whereas the exposed copper atom density at a hexagonally close-packed surface is about 0.2 atoms/Å^2. The discrepancy is greater in the case of cupric and cuprous ions. Clearly the binding energy for Cl^-, Cu^+, and Cu^{2+} predicted by integrating the mean force does not relate well to the reversible work function [96].

Thus in the calculation of the IMF for ions, the ion (1) is forced to move too quickly toward and away from the surface, (2) traverses the wrong path of adsorption/desorption, and/or (3) isn't allowed to establish local equilibrium with the interfacial solvent structure. The more strongly hydrated the species that is moved toward and away from the surface, the more time that is required to allow the fluid to relax as the effective size of the molecule is increased by the tightly-bound hydrating molecules. Also, the faster the forced movement through the fluid the less time the fluid has to adjust, resulting in a larger degree of apparent hysteresis. As discussed previously in the document, there are also very dense layers near the surface. Adsorption/desorption events entail structural changes to these layers that could be difficult to equilibrate. The heating of the fluid as well as slowing the forced movement through the fluid reduces the observed hysteresis between adsorption and desorption paths but does not eliminate it and in the case of ions the hysteresis is still too large to permit quantitative accuracy in adsorption energies.

Shown in Figure 6.12 are the data points used to calculate the integrated mean force for 9 unique site approaches. The plots show the site location (x) versus the set-point position (x_o). The difference between the diagonal line ($x = x_o$) and the site positions is a measure of the biasing force on the site. If the data points lie far away

from the diagonal line, the less reliable are the resultant IMF curves because the force at a particular x_o was found with the site actually significantly removed from x_o.

The agreement between the water IMF and the PMF follows from the fact that none of the locations of the water oxygen deviate greatly from the set-point locations. Also from Fig. 6.12 (a) there is little disagreement between the data for the approach and removal routes. This results in negligible differences between the toward and away IMF water profiles.

In contrast to the water scans, copper and chloride ion locations deviate much more from the set-point positions. There are also larger discrepancies in the positions for the approach and removal scans. It is for these reasons that there is hysteresis in the ion IMF profiles and discrepancies between the ion IMF and PMF potentials.

The ion behavior during forced movement through the interfacial region reflects the large forces from ion-surface and ion-solvent interactions that exist near the surface. For instance, the cupric scans in Fig. 6.12 (d) indicate that there are two closely-spaced locations of high stability at distances very close to the surface. The two locations may correspond to (1) the favorable interplay between the charged surface and the adsorbed chloride ions at $x = 2$ Å and (2) the enhanced ion-surface interaction as the cupric atom settles into a valley of the corrugated copper surface at about $x = 1.8$ Å.

Figure 6.12 (e) and (f) show the data for a sulfur atom of TPT and $SSPSS^{2-}$ near the flat copper surface with Na^+ and Cl^- present. These scans represent the cases of the least and greatest apparent hysteresis in the various IMF scans of TPT, $MPSA^-$, or $SSPSS^{2-}$. The TPT scan in Fig. 6.12 (e) doesn't differ greatly from the water scan in terms of the deviance from the diagonal or the disagreement between the toward and away routes. When a sulfonate group of $SSPSS^{2-}$ is forced to the surface, it requires effort to apparently squeeze other species out from under the large chemical group. On the desorption scan, it seems to take time to fill the void left, as

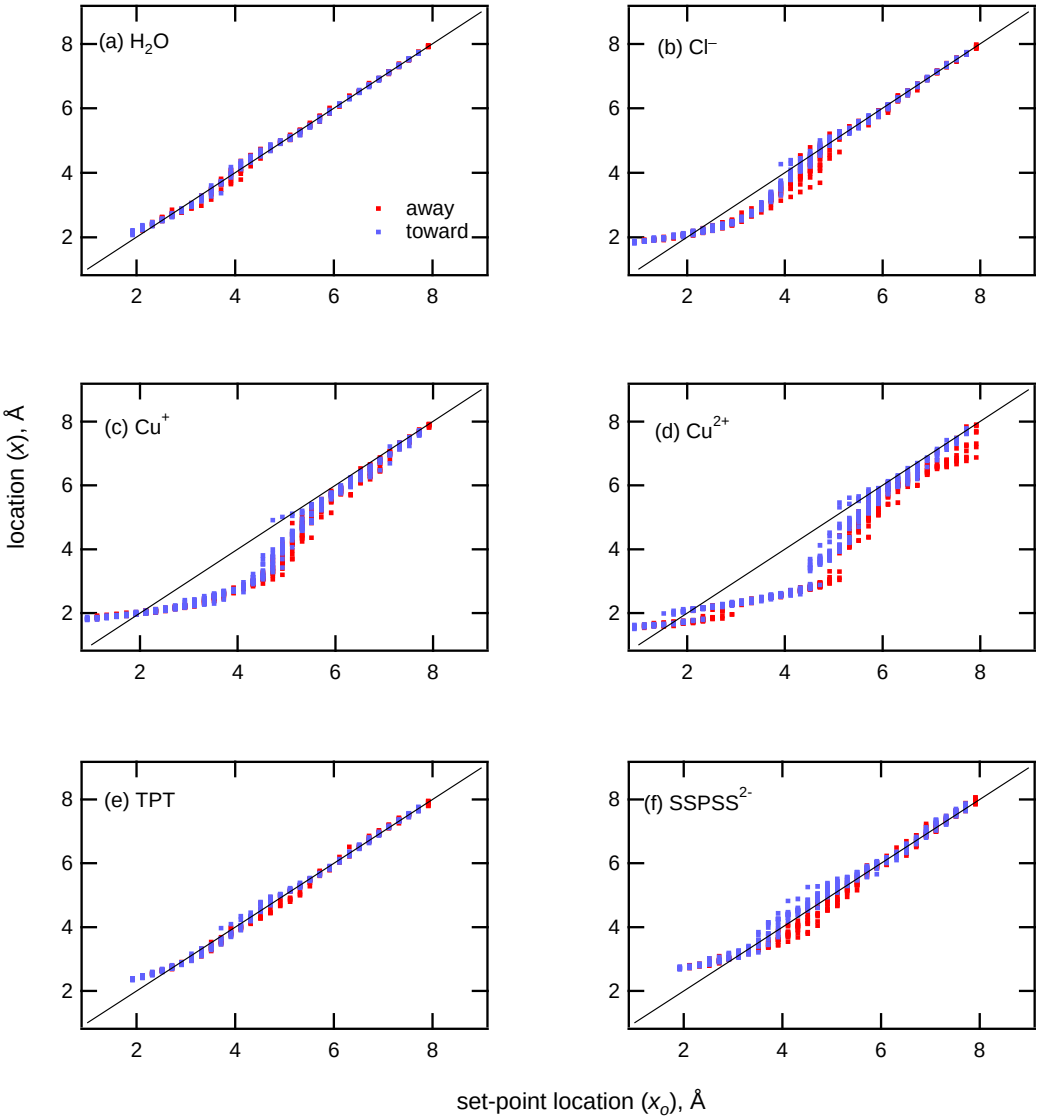

Figure 6.12: Integrated-mean-force raw data for water, ions, and two organic adsorption and desorption events. The plots show the site location (x) versus the set-point position (x_o) for (a) the oxygen atom of water, (b) Cl^- ions, (c) cuprous ion, (d) cupric ion, (e) a sulfur atom of TPT, and (f) a sulfur atom of $SSPSS^{2-}$. The difference between the diagonal line ($x = x_o$) and the site positions is a measure of the biasing force on the site. Blue and red points distinguish between when the site is forced toward and away from the surface respectively. All of the data were collected with sodium chloride present near the flat (111) copper surface.

reflected by the blue dots being above the diagonal and the red dots being below the diagonal in Fig. 6.12 (f). In general, Figure 6.12 gives evidence that the averages of the toward and away IMF curves closely approach the reversible PMF potentials for water, $MPSA^-$, TPT, and $SSPSS^{2-}$ molecules.

6.3.3 Simulated Electrode Work Function

In the electrode charge dynamics routine, the surface charges dynamically adjust to equilibrate the chemical potential of valence charge amongst metal atoms. The work function is equivalent to this chemical potential in the electrode relative to vacuum (ϕ in Eq. 4.10), and is a measure of the amount of work required to remove an electron from the metal out to infinity. It adjusts in response to changes in the environment of the metal. Changes in the work function are easier to compute reliably than changes in the simulated adsorption/desorption energies because the electrostatic potential of the metal fluctuates less than the forces on individual solute molecules.

The electrostatic potential of the metal can be referenced to the standard hydrogen electrode or a saturated mercurous-sulfate reference electrode (SSE) by subtracting the work function of the reference electrode from the simulated work function. I approximate the work function of the standard hydrogen electrode to be 4.6eV [101,102] (or 4.0 eV for SSE). I offset the potential of the two simulated metal electrodes by 3.6 V. This 3.6 V offset was obtained empirically in order for the simulated negative electrode to be at an electrode potential similar to the experimental working electrode. During experimental deposition of copper, copper ions are reduced at the working electrode. This working electrode is negatively charged. Likewise the simulated working electrode is negative.

Shown in Figure 6.13 is the electrostatic potential of the simulated working electrode relative to the SSE reference when the metal interface is perturbed. The work

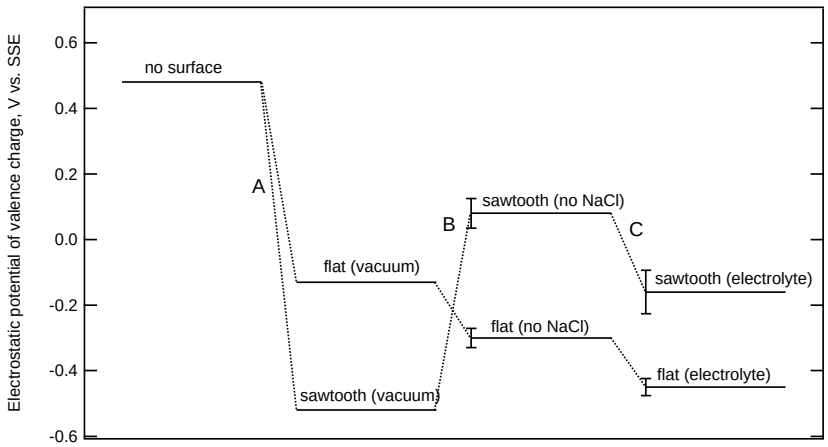

Figure 6.13: Electrostatic potential of the negative electrode relative to the SSE reference when the metal interface is perturbed. Error bars represent the 95% confidence level about the mean value. The work function can be obtained by merely adding 4.0 V to the values found at the ordinate. The labels A, B, and C indicate transitions from one case to another and are labeled to aid the reader in the discussions found in the text.

function can be obtained by merely adding 4.0 V to the values found at the ordinate. Upon creation of an interface (with $\sim$70 Å separating the two metal surfaces) the work required to remove an electron is reduced. This step change in the work function is labeled as transition A in Fig. 6.13. The work required to remove an electron from the sawtooth surface is less than the flat due to the increase in exposed copper atoms resulting in an increase in the sawtooth surface energy.

When an aqueous electrolyte containing copper and bisulfate ions is introduced to fill the vacuum separating the electrode halves (transition B in the figure) the fluid should stabilize the charge on the electrode thereby increasing the work function, making it more difficult for electrons to be removed from the metal. Addition of electrolyte reduces the work function in the case of the flat electrode, which isn't an intuitive result. It may be that the water orientation at the flat surface is such

that long-range order in the fluid (evidenced by two well-defined layers of increased density) can be established and thus decrease the electrode work function due to the dipole orientation in the two water layers. Those regions of well-defined dipolar layers don't exist near the sawtooth surface.

When sodium chloride is included in the electrolyte (transition C in Fig. 6.13) the simulated work function is reduced (relative to the solution lacking sodium-chloride) for both the flat and sawtooth surface geometries. This result indicates that sodium chloride causes a statistically significant change in the ease of surface electron removal. As apparent in Fig. 6.7(a), the chloride ion exists very near the metal surface. As multiple chloride ions adsorb at the negative surface the energy of the negatively charged surface increases. This increase makes it easier for negative charge or electrons to exit the surface and participate in reactions. Experimentally, it is observed that with chloride addition, the rate of copper reduction increases. A reduction in the surface work function can explain how chloride, by itself, increases the copper deposition rate.

A statistically significant difference in the simulated electrostatic metal potentials isn't observed when adding the organic additives studied here. The reason for this is likely due to the relatively small surface area the organic additive occupies when adsorbed at or near the surface. The fluid that influences the metal work function most is that fluid that is closest to and most abundant at the surface.

Experimentally, the open circuit for a 0.24 M $CuSO_4 \cdot 5H_20$ and a 1.8 M H_2SO_4 basic electrolyte is -0.41 V vs. SSE (Chapter 7). This value corresponds well to the simulated case when sodium chloride is included in the fluid at a flat (111) copper surface (Fig. 6.13). This is due to the 3.6 V offset between simulated electrodes that is empirically imposed. I also point out that the ECD model of a bulk copper electrode (still negatively charged, 3.6 V below the positve electrode) gives a work function value of about 4.5 eV which agrees with the experimental work function for

most common metals. This gives credence to the ECD model as it exhibits properties similar to those of a real metal surface.

6.3.4 Copper-Ion Distributions about MPSA

As discussed in Chapter 7, experimentally it has been shown that MPSA accelerates copper deposition in the presence of chloride ions. The acceleration is greater than that which occurs when sodium chloride is added to a MPSA-free bath [92]. At an atomically resolved level, how does MPSA accelerate copper deposition? It may be that the sulfonate group of MPSA acts as a transfer agent to facilitate copper ion reduction near the surface which is similar to the function of sulfonate moieties in cationic exchange membranes such as Nafion® used in the fuel-cell industry.

As the fluid structure near $MPSA^-$ is known in the simulations, I can obtain the distribution of cupric or cuprous ions about the thiol or sulfonate groups of $MPSA^-$. The effects of sodium chloride on that distribution can also be resolved. The simulated structure of MPSA and the surrounding fluid can be related to the MPSA behavior near the experimental copper surface.

Figure 6.14 shows the distribution of copper-ions around the thiol and sulfonate groups of MPSA. The curves indicate the cumulative count of ions from the sulfur atom up to the distance shown at the abscissa. Data were collected around the sulfur of $MPSA^-$ that is forced toward and away from the surface as described above in obtaining the IMF curves.

The most significant effect seen in Fig. 6.14(a) is that upon addition of chloride ions to the bath, the number of copper ions, cupric or cuprous, near $MPSA^-$ decreases. This outcome isn't as significant when the ions are near the thiol group of MPSA. Apparently, sodium chloride addition attenuates the binding energy of copper atoms to sulfonate. It may be that without sodium chloride present, the copper ions are not optimally bound to the sulfonate, but upon addition of sodium chloride

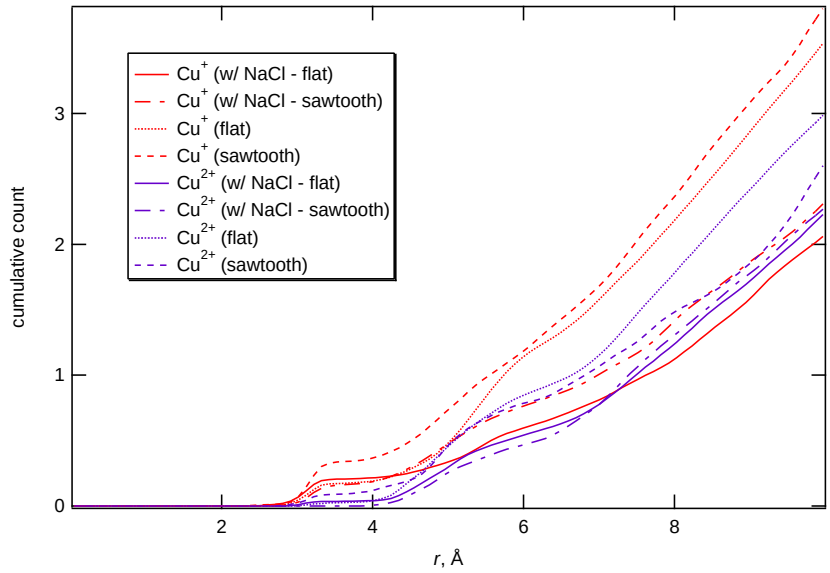

(a) Copper-ion distribution about sulfonate

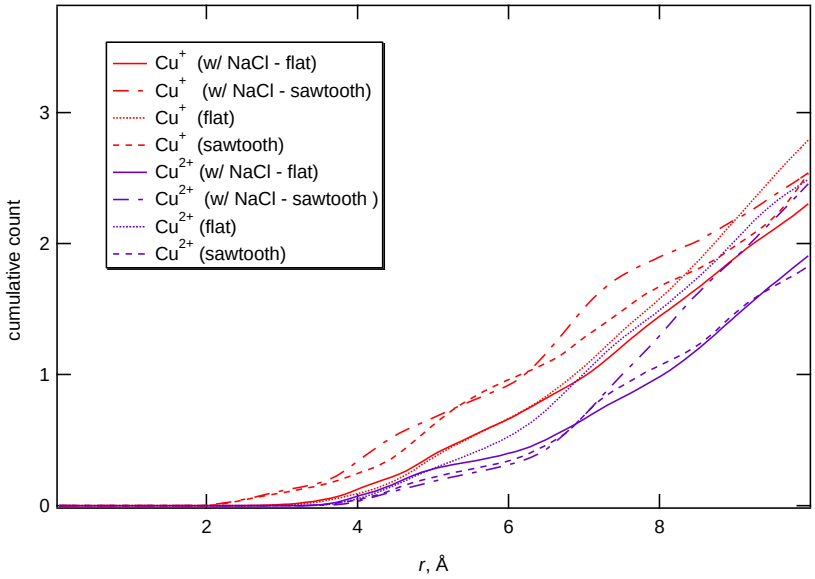

(b) Copper-ion distribution about thiol

Figure 6.14: Copper-ion distribution about the sulfonate and thiol head groups of MPSA. The curves indicate the cumulative count of ions up to a particular distance from the sulfur atom. Data were collected around the sulfur of MPSA that is forced toward and away from the surface as described above in obtaining the IMF curves.

the sulfonate group is better able to assist the transfer of copper ions to the surface. This attenuation of the copper ion binding energy to the sulfonate moiety can be likened to the tuning of chemical binding to metal surfaces in heterogeneous catalysis development. For instance, platinum facilitates the dissociation of oxygen (O_2). The oxygen isn't bound so tightly to the surface that it can't surface diffuse and react, yet it is bound strongly enough to cleave the oxygen-oxygen bond. Other metals aren't as active due to too strongly or too weakly binding with the oxygen.

It is apparent from Fig. 6.14(a) that at 6 Å from the sulfur atom with NaCl present, cupric ions are slightly more abundant near the sulfonate and cuprous ions slightly more abundant near the thiol. Thus, if the MPSA is near the surface (with the thiol group closest to that surface), cupric ions may move from the sulfonate to the surface and be reduced to cuprous ions and then be held near the surface by the thiol group of MPSA. This would provide more opportunity for the cuprous ion to be further reduced to a copper atom.

Figure 6.14(a) shows that cuprous ions are more abundant than cupric ions in the immediate vicinity of the thiol or sulfonate sulfur. This is likely due to the increased hydration strength of cupric relative to the cuprous ion as the cupric and cuprous ions differ only in charge. Again this speaks to the important role water plays as it would otherwise be expected that the more positively charged cupric ions would be nearer the negatively charged oxygen atoms of the sulfonate group.

6.4 Conclusions

Section 6.2.1 describes the *ab initio* potential energy scans of copper ions, bisulfate and sulfate ions, and $MPSA^-$ approaching a Cu_{10} metal cluster. I found that through use of the electrode charge dynamics routine, the *ab initio* quantum-mechanical data can be satisfactorily fit with a small set of intermolecular potential parameters (Table 6.1). The qualitative strength of adsorption at a neutral Cu_{10} cluster is $Cu^+ >$

$Cl^- > Na^+ > HSO_4^- > MPSA^- > H_2O$. At the copper surface in solution, negatively charged at a potential similar to experiment, the adsorption strength is reduced and follows the same order as the *ab initio* results for those species for which the adsorption strength was calculated (Cu^+, Cl^-, $MPSA^-$, and H_2O).

The water structure at the interface plays a critical role in determining interfacial properties. From the species density profiles at a flat interface, chloride adsorbs both at positive and negative surfaces. High frequency oscillating layers of net negative and net positive charge exist at the surface. To obtain accurate species profiles immediately in the vicinity of the solid-liquid interface, the solvent molecules must be explicitly included.

When sodium chloride is included in the simulated electrolyte, the binding energy of $MPSA^-$ (-19 ± 8 kJ/mol) at a flat or sawtooth surface is reduced by 10 ± 9 kJ/mol. Sodium chloride addition also attenuates the sulfonate-copper ion interaction and causes a decrease in the electrode work function. Such a decrease in the work function signifies that electrons can more easily move from the metal to reacting species at the surface. The proposed surface function of NaCl and thiol and sulfonate groups in an electrodeposition bath are summarized in Table 6.3.

Table 6.3: Proposed surface function of sodium chloride, thiol, and sulfonate in an electrodeposition bath.

species/group	function
thiol	surface adhesion
sulfonate	attract copper ions, facilitate ion transfer
NaCl	reduce MPSA adhesion, reduce surface ϕ, attenuate copper-ion attraction to sulfonate

In the next chapter, I present results showing how alkanethiol addition to a copper sulfate sulfuric-acidic electrolyte affects the rate of copper electrodeposition. The alkanethiol additives are MPSA, TPT, and SSPSS. Chapter 7 also shows that addition of sodium chloride to the deposition bath accelerates deposition. Then Chapter 8 compares and combines the simulation and experimental outcomes to address mechanistic questions dealing with the inhibition and acceleration of copper deposition through use of the additives MPSA and chloride ion.

Chapter 7

Chronoamperometry Studies of MPSA, SSPSS, and TPT

7.1 Introduction

This chapter shows how addition of MPSA (3-mercaptopropanesulfonic acid sodium salt) and derivatives of MPSA influence the rate of copper deposition on a rotating disk electrode under galvanostatic (constant electric current) conditions. I simply recorded the electric potential as a function of time as additives are added to the deposition bath while depositing copper at 10 mA/cm^2. At constant current the electrode potential is a measure of the kinetic overpotential, or the ease with which the reaction procedes. Changing the additives in the deposition bath results in a change in the overpotential for deposition depending on whether the additives inhibit or accelerate the reaction. Insight into the action of the thiol end versus the sulfonate end of MPSA can be obtained by adding different additives into the deposition bath and recording the change in overpotential.

Accelerated copper deposition rates have been attributed to an adsorbed cuprous-thiolate complex (Cu(I)-S-(CH_2)-SO_3H) [2, 103, 104]. This study confirms a previous study [92], that shows that chloride ions play an integral role in that acceleration.

Moreover, I and Tan [92] show that in the absence of chloride ions, MPSA inhibits rather than accelerates deposition.

It may be that the thiol molecular group at the end of MPSA causes the observed inhibition of copper deposition (in the absence of chloride ions) by adsorbing to the surface and occupying locations where copper deposition would otherwise occur. In order to investigate this hypothesis I changed the sulfonate group on MPSA to a thiol group (1,3-propanedithiol), or changed the thiol group to sulfonate (1,3-propanedisulfonic acid disodium salt) and observed the resultant effects on the deposition rate. Based on the acceleration or inhibition of deposition, I made inferences about which molecular group is responsible for causing the inhibition.

The next section briefly reviews copper deposition in the presence of thiol-containing additives similar to MPSA. Then I present experimental chronoamperometry results of additive solutions containing derivatives of MPSA, namely 1,3-propanedithiol (TPT) and 1,3-propanedisulfonic acid disodium salt (SSPSS). The experimental results show that the thiol end group of MPSA or TPT is responsible for inhibiting deposition. This and other conclusions are given in the final section.

7.2 Review of Copper Deposition in the Presence of Thiols

In copper electrodeposition, surface association of a cupric or cuprous ion is an important deposition step as reduction occurs by reaction with electrons supplied by the surface. Those surface sites that are higher in energy, such as steps or kinks, are where adsorption is most likely to occur. A deposition event occurs upon cuprous-ion reduction and lattice incorporation. Chemicals added to the electrodeposition bath can play an active role in inhibiting deposition by occupying high-energy surface sites, impeding the transfer of copper ions to the surface, or adversely modifying the structure of the solid-liquid interface.

A self-assembled monolayer (SAM) is an array of molecules that are attached to a surface. Alkanethiol monolayers have been used to selectively block deposition events in high-resolution patterned electrodeposition [105]. As MPSA, a thiol-containing compound, can inhibit copper electrodeposition it is relevant to discuss the literature results of electrodeposition in the presence of SAMs.

Copper deposition on a gold substrate in the presence of a self-assembled monolayer results in a copper deposit structure similar to that obtained by simply increasing the current density [106]. In other words, when short alkanethiol compounds such as propanethiol are surface adsorbed in the form of a SAM, the number density of galvanostatically deposited copper clusters increases and crystalline size decreases. This indicates that the thiol-containing compound may occupy high-energy surface sites, inhibiting copper deposition at those locations. Under galvanostatic conditions, such inhibition would cause an increase in the overpotential and lead to the 'activation' of other sites resulting in an increase in the number of deposition growth centers. In keeping with this picture of inhibition by thiol adsorption, White and Abruna found that 1,3-propanedithiol completely inhibits underpotential deposition of copper on Pt(111) [107].

Copper electrodeposition in the presence of thiol-containing SAMs has also shown that if the alkanethiol is of sufficient length, deposition occurs on the surface of the monolayer. Thus the SAM is incorporated into the growing deposit [106]. Similarly Hagenstrom *et al.* concluded that bulk deposition of silver 'originates almost exclusively at step edges burying the underlying self-assembled monolayer' [108]. In contrast, when propanethiol is used to form the SAM, the thickness of the SAM is such that underpotential deposition and stripping of copper can occur through the SAM layer. The SAM acts as a co-adsorbate during electrodeposition [109]. From these and other studies [110] it is evident that, in the presence of SAMs, reduction of copper can occur at the metal or SAM surface.

Below I report on details and specifics of inhibition by addition of thiol-containing MPSA and TPT to a chloride-free electrolyte solution. I show that the thiol group is integral in inhibiting copper deposition.

7.3 Experimental RDE Study

The rate r_d at which copper is deposited is related to the electric current i passed through the electrochemical cell by $r_d = i/n\mathcal{F}$, where $\mathcal{F}$ is Faraday's constant and n is the number of electrons required to reduce the metal ion to the metallic state. In the case of cupric ions, n is 2. The cell electric potential difference drives the current or rate of electrodeposition, much like the pressure drop drives the flow of fluid through a pipe.

In the results below, I deposit copper under galvanostatic conditions where the rate of deposition remains constant. This keeps the mass-transfer effects constant. I then record how the driving force (electrode potential) responds upon addition of MPSA or a derivative of MPSA. Upon introduction of an additive to the bath, if the electric potential becomes more negative (the difference between the open circuit potential and the deposition potential increases) the additive has inhibited deposition as the driving force required to deposit copper has increased. Likewise, acceleration is exhibited by a more positive value of the electric potential. Below I present the results beginning by first giving the experimental details.

7.3.1 Experimental Details

I electrodeposited copper onto a platinum rotating disk electrode (RDE) in a 100 mL electrolyte solution of 0.24 M $CuSO_4{\cdot}5H_2O$ and 1.8 M H_2SO_4. A Nafion® membrane separated the counter electrode, a copper rod, from the 5mm diameter working electrode. The reference electrode was a saturated mercurous sulfate electrode (SSE). The temperature of the solution during electrodeposition was maintained

at room temperature (24 ± 1° C) by an aqueous bath. The RDE rotation rate was 400 rpm throughout the experiments. In the electrolyte solution there was < 1 ppm Cl^-. A GAMRY PC4 potentiostat was used to control and record the potential and current. High-purity Milli-Q (16-18 MΩ resistance) water was used to ensure solution integrity.

The electrolyte and additive solutions were de-aerated with N_2 gas for 30 min prior to electrodeposition using a glass frit. Just prior to the onset of deposition, the glass frit was removed; however, nitrogen gas continued to be introduced to the vapor space above the electrolyte. Galvanostatic copper deposition at 10 mA/cm^2 reached steady state before additives were introduced into the deposition bath. Additives were added to arrive at desired ppm concentrations by addition of 0.5 or 1 mL of the additive diluted in Milli-Q water.

7.3.2 Chronoamperometry Results

Shown in Figure 7.1 are the 10 mA/cm^2 chronoamperometry results when 1 ppm (by weight) MPSA, TPT, or SSPSS (all acquired from Sigma-Aldrich) are added to the electrolyte. Also shown are the electric potential variations when 50 ppm NaCl (Columbus Chemical Industries, ACS grade) was subsequently introduced to the deposition bath. When the thiol-containing compounds MPSA or TPT are introduced to the electrolyte, copper deposition is inhibited. Note the similar strengths by which deposition is inhibited upon addition of either thiol-containing additive. When SSPSS is introduced to the chloride free bath very slight acceleration is evident. In cases where a sulfonate group is in solution (MPSA or SSPSS), subsequent chloride addition results in acceleration above the initial, additive-free electrolyte.

As seen in Fig. 7.1, inclusion of the thiol-containing compounds MPSA and TPT results in inhibition. When the thiol molecular group is absent, as in SSPSS, I see that additive addition to the electrolyte conversely results in slight acceleration. When

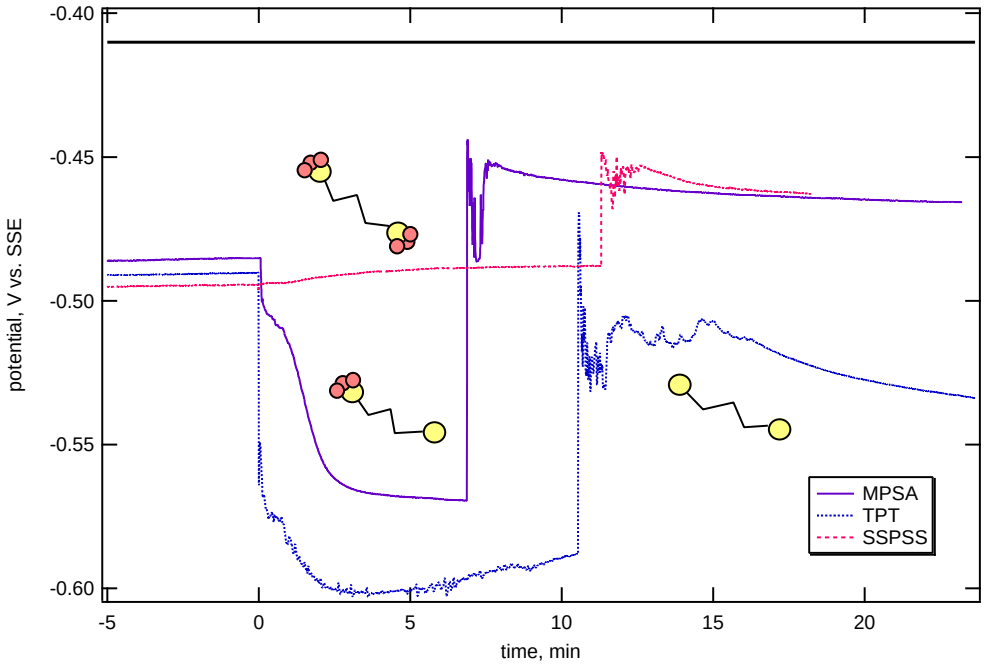

Figure 7.1: Electrostatic potential variations when 1 ppm MPSA, SSPSS, or TPT are added followed by 50 ppm NaCl addition to the electrolyte. Organic additives are added at time zero. The sharp rises in the electric potential curves at times between 7 and 12 minutes indicate the addition of NaCl. The line at -0.41 V represents the open circuit potential value. Copper is deposited at 10 mA/cm^2.

sodium chloride is added to an electrolyte containing MPSA, TPT, or SSPSS, copper electrodeposition is accelerated. Only addition of those molecules that contain sulfonate (MPSA and SSPSS) result in acceleration greater than the initial, additive-free case.

7.4 Conclusions

From the above results, I conclude that inhibition is primarily due to the presence of the thiol chemical group of MPSA. Thiol induced inhibition may be caused by the formation of surface sulfides that occupy high-energy surface sites [111]. Addition of the thiol-containing short-chained compounds of MPSA and TPT cause inhibition of copper deposition in a chloride-free electrodeposition bath. Addition of SSPSS (1,3-propanedisulfonic acid) results in slight acceleration.

The inhibiting species appears to be active at the surface. Tan found that the inhibiting molecule was not easily water-rinsed from the cathodic surface [92]. The miscibility of TPT (1,3-propanedithiol) in water is very small relative to the miscibility of MPSA. Thus, the thiol molecular group is somewhat hydrophobic and the interactions between it and the solution would therefore tend to localize it at the electrode surface relative to the bulk solution. Incidentally, this may explain why thiol adsorbs more strongly experimentally even though in vacuum, *ab initio* results give a smaller adsorption energy for thiol than for sulfonate. The self-assembled monolayer studies (Section 7.2), the rinsing experiments [92], the miscibility of TPT, and the molecular dynamics results all reinforce the premise that the inhibiting species is active at the surface.

From the simulated and these experimental results, thiol-containing MPSA or TPT appears to be bound to the surface, occupying surface active sites. The bound molecules are presumed to block the reduction of copper ions and so results in the observed inhibition. When chloride ions are added, the binding energy of MPSA and

TPT is reduced. This frees surface sites where copper reduction can take place and so results in acceleration. Chloride also influences the work function of the interface resulting in facilitated deposition. Additionally, trace amounts of chloride ions can also catalyze the reduction of cupric ions in solution [112–115].

Sulfonate groups of MPSA and SSPSS facilitate the deposition of copper. This may occur by holding the copper cations near the surface, thus increasing the copper-ion surface concentration resulting in acceleration. This idea of the sulfonate binding with the copper cations coincides with the cationic action of the sulfonate groups in a Nafion® exchange membrane. Also, sodium chloride addition to the sulfonate containing MPSA bath results in greater acceleration than acceleration solely by chloride addition. This suggests that in addition to the acceleration caused by sodium chloride alone and in addition to the NaCl caused reduction in the MPSA induced inhibition, NaCl interacts with MPSA or TPT to facilitate its action of acceleration.

Chapter 8

Summary

In this work I have investigated how MPSA (3-mercaptopropane sulfonic acid) influences copper electrodeposition using *ab initio* quantum calculations, molecular-dynamic simulations, and experimental chronoamperometry studies. This work has shown that chloride interacts strongly with the system to reverse the rate inhibiting effects of thiol-containing compounds. The evidence suggests that sulfonate aids copper-ion movement to the surface. Below I merge the conclusions from the molecular simulations reported here with related experimental work. The next section summarizes the process of obtaining, and significance of, the molecular-dynamic results.

8.1 Molecular Models Summary

The intra- and inter-molecular potentials determine the outcome of the simulated system behavior. Thus it is imperative to accurately represent the potential energy surface (PES) of the system. Through use of combining rules, *ab initio* calculations, semi-empirical models, and the electrode charge dynamics routine, I satisfactorily represent the PES with surprisingly few parameters. Interatomic potential parameters in solution are given in Chap. 2, and solution-electrode parameters are found in Chaps. 4 and 6.

The electrode charge dynamics (ECD) routine bridges the gap between small-scale quantum-mechanical calculations of metal clusters to large-scale simulations of metal surfaces of arbitrary geometry. Specifically, the ECD method accurately reproduces small metal cluster quantum-mechanical results. It also accurately represents the interaction of a charge with a metal surface. The ability to treat both the short- and long-range charge-metal interactions without artificial patches represents a significant addition to molecular simulation. By "patches" is meant a scheme whereby the image-charge potential is used at long distances and an *ab initio*-derived potential is used at short range, with a smooth transition between the two.

As the molecular solvent water is most abundant in the cell, hydration of the solute and electrode dominate system interactions. Although I have chosen to use the rigid SPC/E model of water, I did investigate the effects of intramolecular vibrational modes on solid-liquid interfacial characteristics. Chap. 3 reports on the effects of including solvent intramolecular modes of vibration using the rRESPA routine. Allowing the hydrogen-oxygen bonds and hydrogen-oxygen-hydrogen angle to vibrate decreases the ion hydration near the surface resulting in increased amounts of ions adsorbed at the surface.

8.2 Simulation Summary

Through the molecular simulations reported here I have shown the existence of a two-dimensional high-density ice layer that exists on a flat (111) copper surface in qualitative agreement with experiment [7,116]. In the area nearest the surface, significant property variations are evident in the fluid. Thus, near solid-liquid interfaces, it is imperative to include atomically resolved solvent molecules to properly account for large variations in density or dielectric constant.

Aqueous simulations of copper ions, bisulfate ions, and sodium chloride near a (111) flat copper surface show adsorption of chloride ions at a negative surface and

show evidence of copper-chloride ion association. The concentration of ions at the surface is significantly greater than in the bulk.

I also have shown from the simulations that $MPSA^-$ is attracted to the surface and upon sodium chloride addition, the binding energy is reduced. Chloride also reduces the work function of the copper metal. The sulfonate may aid in the transfer of species to the interface in a way that is similar to sulfonate function in cationic exchange membranes like Nafion®. I observe a reduction in the copper-ion binding energy to sulfonate when sodium chloride is included in the solution. Thus chloride also attenuates the copper-ion binding to sulfonate and thus may increase the effectiveness of sulfonate to aid in accelerating copper deposition.

8.3 Mechanism of MPSA Inhibition and Acceleration

In the experimental results presented in the previous chapter, I conclude that the thiol group of MPSA is responsible for inhibition of copper deposition. This may occur as the thiol binds to the active surface sites and thus reduces the ease of copper-ion reduction as it blocks ion transfer to the copper surface. I also show experimental results indicating that the sulfonate group of MPSA can cause acceleration.

I summarize the simulation and experimental conclusions pictorially in Figure 8.1. The procession from the upper to the lower representation in the figure indicates some of the effects of chloride as well as the action of the thiol and sulfonate groups. The solid half-circle drawn around the sulfonate group indicates possible excessive binding of copper ions to the sulfonate. The dashed half-circle indicates that sulfonate (in the presence of sodium chloride) may be better able to facilitate copper-ion reduction. The reduction in the work function of the surface by chloride addition isn't represented in the figure.

This explanation of the action of MPSA (with and without chloride present) during copper deposition inhibition is a simple one and logically follows from principles

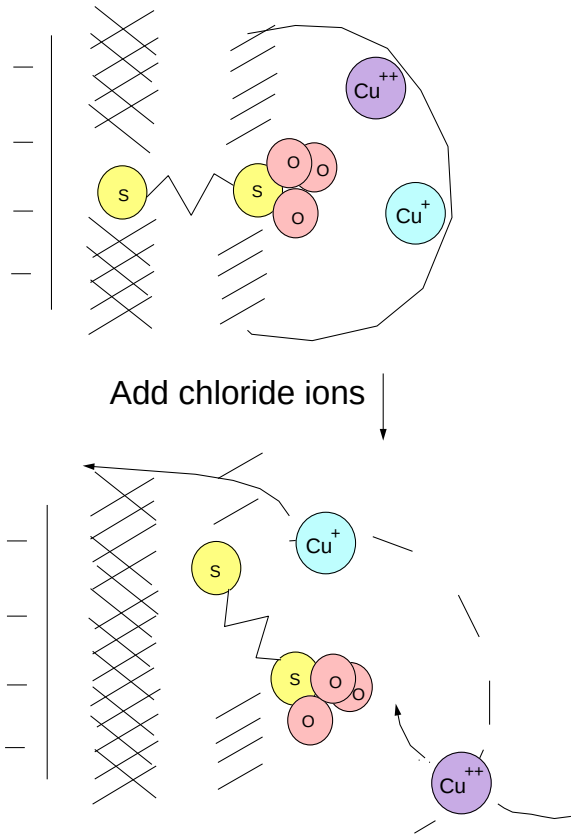

Figure 8.1: Pictorial summary of the simulation and experimental conclusions. The procession from the upper to the lower representation in the figure indicates some of the effects of chloride as well as the action of the thiol and sulfonate groups. The solid half-circle drawn around the sulfonate group indicates possible excessive binding of copper ions to the sulfonate. The dashed half-circle indicates that sulfonate may be better able to facilitate copper-ion reduction. The cross-hatched lines signify the two layers of highly dense fluid near the surface.

involved in self-assembled monolayers, cationic-exchange membranes, and catalysis. The mechanism is different than that previously suggested by Zhukauskaite *et al.* [117] and others [104, 118] that require favorable configurations of multiple molecules and don't explicitly indicate the influence of sodium chloride on the action of MPSA or SPS (bis-3-sodium sulfopropyl disulfide, a dimer of MPSA).

8.4 Summary and Future Prospects

The water structure at an electrochemical interface greatly influences surface-ion adsorption in aqueous systems. In this work I found that a dense layer of water exits at a Cu(111) flat surface. In this dense layer the water molecules hydrogen bond primarily to other water molecules in the same layer. This results in a highly organized sheet of water at the aqueous-Cu(111) interface. This dense surface layer of water must be disrupted in order for ions to contact adsorb at the metal surface. This work investigated the water and ion structure at the interface for various systems using *ab initio* and an effective routine I developed to treat the charge mobility in the metal.

In addition to providing insight into the water and ion interfacial structure, I used quantum-mechanics and the electrode charge dynamics routine (in molecular simulations) to show the effect of sodium chloride on (1) the adsorption strength of MPSA, (2) the work function of the copper surface, and (3) the distribution of ions near MPSA. These molecular dynamics results were then used and augmented with experimental results to explain qualitatively a possible mechanism for the accelerating effects of sodium chloride and organic additive addition to a copper deposition bath. The molecular dynamic simulations were not able to quantitatively validate the proposed mechanism. For example the specific movement of the MPSA (in the presence of NaCl) near the copper surface that results in an enhanced rate of copper ion reduction was not discovered. This inability of the molecular simulations to resolve

the dynamics of the facilitated transfer and reduction of copper ions through MPSA is due to the small number of atoms simulated over a short time interval relative to experimental conditions.

In order for molecular simulation to accurately reflect the specific steps of molecular-level processes like MPSA-assisted copper deposition in the presence of sodium chloride, the scale of molecular simulations must increase. Interfacial properties that are determined by the motion and interactions of many molecules (*e.g.* species density profiles or electrostatic potential profiles) can presently be resolved; however, some mechanisms like how MPSA affects the copper-ion distribution near the surface are not effectively determined. An increase in simulation size and time scale would decrease the variability in simulated outcomes such as adsorption energies and allow for more dilute concentrations to be simulated.

Instead of treating the entire system atomically, a focused computational effort of the regions of most importance (or most variation) can be done. This type of computation would combine molecular dynamics outcomes with more coarse-grained models. For example, the solvent nearest the electrode (< 10 Å) could be atomically resolved whereas out away from the surface the solvent could be modeled as a continuum thus allowing a larger interfacial area to be effectively simulated.

Ultimately, the system behavior is determined by the molecular interactions. Whether modeling the interface at a molecular or macroscopic scale, the molecular interactions describing the fluid behavior must be included accurately. Thus it is important that *ab initio* and other quantum calculation schemes reliably reproduce the potential energy between atoms in the systems of interest. Herein the interaction potentials of the copper ions with the solution and copper surface were approximated as the *ab initio* results for Cu^{+} and Cu^{2+} were questionable. Here the copper atom is the heaviest atom (with 29 electrons) and was the only atomic species for which

I used psuedopotentials that represent the inner core of electrons. Perhaps this approximation lead to the observed discrepancies in the *ab initio* results. More accurate first-principles calculations would result in more reliable simulated outcomes. Moreover, the calculations should be obtained in the same environment (solid, liquid, or gas phase) in which they intend to be used.

Further opportunities to build upon this work include simulating hydronium ions explicitly (as the experimental solution is acidic) and investigating the process of copper ion movement from the solution, through the double layer, reduction near the surface, and incorporation into the metal lattice. At the scale of molecular simulation, this transfer of copper from solution into the metal lattice is a rare event. Effective schemes that focus on rare events (like climbing-image nudged-elastic band [98] or blue-moon molecular simulation [119]) can be accurately coupled with *ab initio* calculations and molecular simulation to investigate at a fundamental level the nuances of deposition or dissolution events.

The hydration of ions and the metal surface determines the interfacial structure. Although SPC/E water has been used to reproduce experimental water behavior in the bulk, the water models discussed in this work, whether flexible or rigid, have not been verified for use at an electrochemical interface. Here I used a rigid model as the bulk properties of SPC/E water have been established at conditions used in this work and for the reason that simulating a flexible model increases computational costs. The water structure in molecular simulations of electrochemical interfaces needs to be more extensively verified.

The desired control over materials is increasingly being forced to smaller dimensions. We need to better understand molecular details of interfaces. Realistic molecular simulation can provide those atomically resolved details. As such, more accurate molecular simulations implementing and developing efficient methods will be a growing arena in materials and engineering research.

Bibliography

[1] L. Kesmodel and L. Falicov, "Electronic potential in a metal close to a surface edge," *Solid State Communications*, vol. 16, no. 10–11, pp. 1201–1204, 1975.

[2] P. Vereecken, R. Binstead, H. Deligianni, and P. Andricacos, "The chemistry of additives in damascene copper plating," *IBM Journal of Research and Development*, vol. 49, no. 1, pp. 3–17, 2005.

[3] G. Gouy *Journal de Physique*, vol. 9, no. 4, p. 457, 1910.

[4] D. Chapman *Philosophical Magazine*, vol. 25, p. 475, 1913.

[5] O. Stern *Zeitschrift für Elektrochemie*, vol. 30, p. 508, 1924.

[6] I.-C. Yeh and M. L. Berkowitz, "Aqueous solution near charged Ag(111) surfaces: comparison between a computer simulation and experiment," *Chemical Physics Letters*, vol. 301, pp. 81–86, 1999.

[7] M. F. Toney, J. N. Howard, J. Richer, G. L. Borges, J. G. Gordon, O. R. Melroy, D. G. Wiesler, D. Yee, and L. B. Sorensen, "Distribution of water molecules at Ag(111)/electrolyte interface as studied with surface x-ray scattering," *Surface Science*, vol. 335, pp. 326–332, 1995.

[8] D. L. Price and J. Halley, "Molecular dynamics, density functional theory of the metal-electrolyte interface," *Journal of Chemical Physics*, vol. 102, no. 16, pp. 6603–6612, 1995.

[9] S. Izvekov, M. R. Philpott, and R. I. Eglitis, "*Ab initio* simulations of metal cluster surrounded by electrolyte," *Journal of The Electrochemical Society*, vol. 147, no. 6, pp. 2273–2278, 2000.

[10] S. Izvekov and G. A. Voth, "*Ab initio* molecular dynamics simulation of the Ag(111)–water interface," *Journal of Chemical Physics*, vol. 115, no. 15, pp. 7196–7206, 2001.

[11] S. Izvekov, A. Mazzolo, K. VanOpdorp, and G. A. Voth, "*Ab initio* molecular dynamics simulation of the Cu(110)–water interface," *Journal of Chemical Physics*, vol. 114, no. 7, pp. 3248–3257, 2001.

[12] P. S. Crozier, D. Henderson, R. L. Rowley, and D. D. Busath, "Model channel ion currents in NaCl-extended simple point charge water solution with applied-field molecular dynamics," *Biophysical Journal*, vol. 81, no. 6, pp. 3077–3089, 2001.

[13] C. G. Guymon, R. L. Rowley, J. N. Harb, and D. R. Wheeler, "Simulating an electrochemical interface using charge dynamics," *Condensed Matter Physics*, vol. 8, no. 2, pp. 335–356, 2005.

[14] D. R. Wheeler, *Molecular Simulations of Diffusion in Electrolytes*. PhD thesis, University of California, Berkeley, 2002.

[15] E. Spohr, "Molecular simulation of the electrochemical double layer," *Electrochimica Acta*, vol. 44, pp. 1697–1705, 1999.

[16] M. R. Philpott and J. N. Glosli, *Molecular Dynamics Simulation of Interfacial Electrochemical Processes: Electric Double Layer Screening*, vol. 656(13) of *ACS Symposium Series*, pp. 11–30. American Chemical Society, 1997. in *Solid-Liquid Electrochemical Interfaces*, edited by G. Jerkiewicz, M. P. Soriaga, K. Uosaki, and A. Wieckowski.

[17] D. Boda, K.-Y. Chan, and D. Henderson, "Monte Carlo simulation of an ion-dipole mixture as a model of an electrical double layer," *Journal of Chemical Physics*, vol. 109, no. 17, pp. 7362–7371, 1998.

[18] C. G. Guymon, M. L. Hunsaker, J. N. Harb, D. Henderson, and R. Rowley, "Effects of solvent model flexibility on aqueous electrolyte behavior between electrodes," *Journal of Chemical Physics*, vol. 118, no. 22, pp. 10195–10202, 2003.

[19] P. S. Crozier, R. L. Rowley, and D. Henderson, "Molecular dynamics calculations of the electrochemical properties of electrolyte systems between charged electrodes," *Journal of Chemical Physics*, vol. 113, no. 20, pp. 9202–9207, 2000.

[20] D. Boda, D. Gillespie, W. Nonner, D. Henderson, and B. Eisenberg, "Computing induced charges in inhomogeneous dielectric media: Application in a Monte Carlo simulation of complex ionic systems," *Physical Review E*, vol. 69, p. 046702, 2004.

[21] T. O. Drews, E. G. Webb, D. L. Ma, J. Alameda, R. D. Braatz, and R. C. Alkire, "Coupled mesoscale–continuum simulations of copper electrodeposition in a trench," *AIChE Journal*, vol. 50, no. 1, pp. 226–240, 2004.

[22] E. Spohr, "Molecular dynamics simulations of water and ion dynamics in the electrochemical double layer," *Solid State Ionics*, vol. 150, pp. 1–12, 2002.

[23] P. Bopp and K. Heinzinger, "MD studies of electrolyte solution|liquid mercury interfaces," *Journal of Electroanalytical Chemistry*, vol. 450, pp. 165–173, 1998.

[24] D. Frenkel and B. Smit, *Understanding Molecular Simulation From Algorithms to Applications*. Academic Press, 2002.

[25] M. Allen and D. Tildesley, *Computer Simulation of Liquids*. Oxford University Press, 1989.

[26] R. L. Rowley, *Statistical Mechanics for Thermophysical Property Calculations*. Prentice-Hall, 1994.

[27] J. Jalkanen, T. Pakkanen, Y. Yang, and R. Rowley, "Interaction energy surfaces of small hydrocarbon molecules," *Journal of Chemical Physics*, vol. 118, no. 12, pp. 5474–5483, 2003.

[28] D. R. Wheeler and R. L. Rowley, "Shear viscosity of polar liquid mixtures via non-equilibrium molecular dynamics: water, methanol, and acetone," *Molecular Physics*, vol. 94, no. 3, pp. 555–564, 1998.

[29] R. Hockney and J. Eastwood, *Computer Simulation Using Particles*. Bristol: Institute of Physics, 1988.

[30] M. Kawata, M. Mikami, and U. Nagashima, "Computationally efficient method to calculate the Coulomb interactions in three-dimensional systems with two-dimensional periodicity," *Journal of Chemical Physics*, vol. 116, no. 8, pp. 3430–3448, 2002.

[31] I.-C. Yeh and M. L. Berkowitz, "Ewald summation for systems with slab geometry," *Journal of Chemical Physics*, vol. 111, no. 7, pp. 3155–3162, 1999.

[32] P. S. Crozier, R. L. Rowley, E. Spohr, and D. Henderson, "Comparison of charged sheets and corrected 3D Ewald calculations of long-range forces in slab geometry electrolyte systems with solvent molecules," *Journal of Chemical Physics*, vol. 112, no. 21, pp. 9253–9257, 2000.

[33] M. Frisch, G. Trucks, H. Schlegel, G. Scuseria, M. Robb, J. Cheeseman, V. Zakrzewski, J. Montgomery, Jr., R. Stratmann, J. Burant, S. Dapprich, J. Millam, A. Daniels, K. Kudin, M. Strain, O. Farkas, J. Tomasi, V. Barone, M. Cossi, R. Cammi, B. Mennucci, C. Pomelli, C. Adamo, S. Clifford, J. Ochterski, G. Petersson, P. Ayala, Q. Cui, K. Morokuma, D. Malick, A. Rabuck, K. Raghavachari, J. Foresman, J. Cioslowski, J. Ortiz, B. Stefanov, G. Liu, A. Liashenko, P. Piskorz, I. Komaromi, R. Gomperts, R. Martin, K. Fox, T. Keith, M. Al-Laham, C. Peng, A. Nanayakkara, C. Gonzalez, M. Challacombe, P. Gill, B. Johnson, W. Chen, M. Wong, J. Andres, C. Gonzalez, M. Head-Gordon, E. Replogle, and J. Pople, "Gaussian 98." Gaussian, Inc. Pittsburgh PA, 1998. Revision A.6.

[34] H. Ruuska, R. L. Rowley, and T. A. Pakkanen, "MP2 study on water adsorption on cluster models of Cu(111)," *Journal of Physical Chemistry B*, vol. 108, no. 8, pp. 2614–2619, 2004.

[35] H. Berendsen, J. Grigera, and T. Straatsma, "The missing term in effective pair potentials," *Journal of Physical Chemistry*, vol. 91, pp. 6269–6271, 1987.

[36] J. L. Fulton, M. M. Hoffmann, J. G. Darab, and B. J. Palmer, "Copper(I) and copper(II) coordination structure under hydrothermal conditions at 325 °C: An x-ray absorption fine structure and molecular dynamics study," *Journal of Physical Chemistry A*, vol. 104, pp. 11651–11663, 2000.

[37] C. F. Schwenk and B. M. Rode, "New insights into the Jahn-Teller effect through ab initio quantum-mechanical/molecular-mechanical molecular dynamics simulations of Cu(II) in water," *CHEMPHYSCHEM*, vol. 4, pp. 931–943, 2003.

[38] M. Dolg, U. Wedig, H. Stoll, and H. Preuss, "Energy-adjusted *ab initio* pseudopotentials for the first row transition elements," *Journal of Chemical Physics*,

vol. 86, no. 2, pp. 866–872, 1987.

[39] W. L. Jorgensen, J. D. Madura, and C. J. Swenson, "Optimized intermolecular potential functions for liquid hydrocarbons," *Journal of the American Chemical Society*, vol. 106, pp. 6638–6646, 1984.

[40] G. A. Kaminski, R. A. Friesner, J. Tirado-Rives, and W. L. Jorgensen, "Evaluation and reparametrization of the OPLS-AA force fields for proteins via comparison with accurate quantum chemical calculations on peptides," *Journal of Physical Chemistry B*, vol. 105, pp. 6474–6487, 2001.

[41] R. W. Impey, M. L. Klein, and I. R. McDonald, "Structural and dynamic properties of lithium sulphate in its solid electrolyte form," *Journal of Chemical Physics*, vol. 82, no. 10, pp. 4690–4698, 1985.

[42] A. Vishnyakov and A. V. Neimark, "Molecular dynamics simulation of nafion oligomer solvation in equimolar methanol–water mixture," *Journal of Physical Chemistry B*, vol. 105, no. 32, pp. 7830–7834, 2001.

[43] D. Spangberg and K. Hermansson, "Many-body potentials for aqueous Li^+, Na^+, Mg^{2+}, and Al^{3+}: Comparison of effective three-body potentials and polarizable models," *Journal of Chemical Physics*, vol. 120, no. 10, pp. 4829–4843, 2004.

[44] G. Halász, A. Vibók, S. Suhai, and I. Mayer, "Toward a BSSE-free description of strongly interacting systems," *International Journal of Quantum Chemistry*, vol. 89, pp. 190–197, 2002.

[45] A. Ignaczak and J. Gomes, "Quantum calculations on the adsorption of halide ions on the noble metals," *Journal of Electroanalytical Chemistry*, vol. 420, pp. 71–78, 1997.

[46] A. Ignaczak, J. Gomes, and S. Romanowski, "The potential of mean force on halide ions near the Cu(100) surface," *Journal of Electroanalytical Chemistry*, vol. 450, pp. 175–188, 1998.

[47] R. R. Nazmutdinov and M. Shapnik, "Contemporary quantum chemical modelling of electrified interfaces," *Electrochimica Acta*, vol. 41, no. 14, pp. 2253–2265, 1996.

[48] A. Ignaczak, "DFT calculations of the interaction of alkali ions with copper and silver," *Journal of Electroanalytical Chemistry*, vol. 495, pp. 160–168, 2001.

[49] A. Ignaczak and J. Gomes, "A theoretical study of the interaction of water molecules with the Cu(100), Ag(100) and Au(100) surfaces," *Journal of Electroanalytical Chemistry*, vol. 420, pp. 209–218, 1997.

[50] E. Spohr, G. Toth, and K. Heinzinger, "Structure and dynamics of water and hydrated ions near platinum and mercury surfaces as studied by MD simulations," *Electrochimica Acta*, vol. 44, no. 14, pp. 2131–2144, 1996.

[51] L. Bosio, R. Cortes, M. Denoziere, and G. Folcher *Coll. Phys. C7*, vol. 50, p. 23, 1989.

[52] A. Lyubartsev, K. Laasonen, and A. Laaksonen, "Hydration of Li^+ ion. An *ab initio* molecular dynamics simulation," *Journal of Chemical Physics*, vol. 114, no. 7, pp. 3120–3126, 2001.

[53] G. Toth, "*Ab initio* pair potential parameter set for the interaction of a rigid and a flexible water model and the complete series of the halides and alkali cations," *Journal of Chemical Physics*, vol. 105, no. 13, pp. 5518–5524, 1996.

[54] D. Laria and R. Fernández-Prini, "Molecular dynamics study of water clusters containing ion pairs: From contact to dissociation," *Journal of Chemical Physics*, vol. 102, no. 19, pp. 7664–7673, 1995.

[55] A. Kohlmeyer, C. Hartnig, and E. Spohr, "Orientational correlations near interfaces, computer simulations of water and electrolyte solutions in confined environments," *Journal of Molecular Liquids*, vol. 78, pp. 233–253, 1998.

[56] E. Oyen and R. Hentschke, "Molecular dynamics simulation of aqueous sodium chloride solution at the NaCl(001) interface with a polarizable water model," *Langmuir*, vol. 18, pp. 547–556, 2002.

[57] P. S. Crozier, R. L. Rowley, and D. Henderson, "Molecular-dynamics simulations of ion size effects on the fluid structure of aqueous electrolyte systems between charged model electrodes," *Journal of Chemical Physics*, vol. 114, no. 17, pp. 7513–7517, 2001.

[58] I. G. Tironi, R. M. Brunne, and W. F. van Gunsteren, "On the relative merits of flexible versus rigid models for use in computer simulations of molecular liquids," *Chemical Physics Letters*, vol. 250, pp. 19–24, 1996.

[59] O. Teleman, B. Jönsson, and S. Engström, "A molecular dynamics simulation of a water model with intramolecular degrees of freedom," *Molecular Physics*, vol. 60, no. 1, pp. 193–203, 1987.

[60] S. J. Stuart, R. Zhou, and B. J. Berne, "Molecular dynamics with multiple time scales: The selection of efficient reference system propagators," *Journal of Chemical Physics*, vol. 105, no. 4, pp. 1426–1436, 1996.

[61] M. Tuckerman, B. Berne, and G. Martyna, "Reversible multiple time scale molecular dynamics," *Journal of Chemical Physics*, vol. 97, no. 3, pp. 1990–2001, 1992.

[62] N. G. Fuller and R. L. Rowley, "The effect of model internal flexibility upon NEMD simulations of viscosity," *International Journal of Thermophysics*, vol. 21, p. 45, 2000.

[63] Y. Yang. PhD thesis, Brigham Young University, 2001.

[64] D. Eisenberg and W. Kanzman, *The Structure and Properties of Water*. London: Oxford University Press, 1969.

[65] C. C. Liew, H. Inomata, and K. Arai, "Flexible molecular models for molecular dynamics study of near and supercritical water," *Fluid Phase Equilibria*, vol. 144, pp. 287–298, 1998.

[66] B. Guillot and Y. Guissani, "How to build a better pair potential for water," *Journal of Chemical Physics*, vol. 114, no. 15, pp. 6720–6733, 2001.

[67] J. Postma, *MD of H_2O*. PhD thesis, University of Groningen, 1985.

[68] E. Spohr, "Computer simulation of the structure of the electrochemical double layer," *Journal of Electroanalytical Chemistry*, vol. 450, pp. 327–334, 1998.

[69] E. Spohr, *Computer Simulation of the Structure and Dynamics of Water Near Metal Surfaces*, vol. 656(13) of *ACS Symposium Series*, pp. 31–44. American Chemical Society, 1997. in *Solid-Liquid Electrochemical Interfaces*, edited by G. Jerkiewicz, M. P. Soriaga, K. Uosaki, and A. Wieckowski.

[70] W. Schmickler and D. Henderson, "New models for the structure of the electrochemical interface," *Progress in Surface Science*, vol. 22, no. 4, pp. 323–420, 1986.

[71] A. Ignaczak and J. Gomes, "Simulations of liquid water in contact with a Cu(100) surface," *Journal of Molecular Structure (Theochem)*, vol. 464, pp. 227–238, 1999.

[72] G. Evangelakis, E. Vamvakopoulos, D. Pantelios, and N. Papanicolaou, "Coverage dependent self-diffusion on Cu(111) by molecular dynamics," *Surface Science*, vol. 425, pp. L393–L399, 1999.

[73] C. Ursenbach, A. Calhoun, and G. A. Voth, "A first-principles simulation of the semiconductor/water interface," *Journal of Chemical Physics*, vol. 106, no. 7, pp. 2811–2818, 1997.

[74] R. I. Masel, *Principles of Adsorption and Reaction on Solid Surfaces*. John Wiley & Sons, Inc, 1996.

[75] R. Allen, J.-P. Hansen, and S. Melchionna, "Electrostatic potential inside ionic solutions confined by dielectrics: a variational approach," *Physical Chemistry Chemical Physics*, vol. 3, p. 4177, 2001.

[76] A. K. Rappé and W. A. Goddard III, "Charge equilibration for molecular dynamics simulations," *Journal of Physical Chemistry*, vol. 95, pp. 3358–3363, 1991.

[77] S. W. Rick, S. J. Stuart, and B. J. Berne, "Dynamical fluctuating charge force fields: Application to liquid water," *Journal of Chemical Physics*, vol. 101, no. 7, pp. 6141–6156, 1994.

[78] W. H. Press, B. P. Flannery, S. A. Teukolsky, and W. T. VetterlingJohn, *Numerical recipes: the art of scientific computing*, vol. 1. Cambridge University Press, 1986.

[79] S. Nose, "A molecular-dynamics method for simulation in the canonical ensemble," *Molecular Physics*, vol. 52, no. 2, pp. 255–268, 1984.

[80] D. R. Wheeler, N. G. Fuller, and R. L. Rowley, "Non-equilibrium molecular dynamics simulation of the shear viscosity of liquid methanol: adaptation of the

Ewald sum to Lees-Edwards boundary conditions," *Molecular Physics*, vol. 92, no. 1, pp. 55–62, 1997.

[81] D. R. Wheeler and J. Newman, "A less expensive Ewald lattice sum," *Chemical Physics Letters*, vol. 366, no. 5–6, pp. 537–543, 2002.

[82] M. Deserno and C. Holm, "How to mesh up Ewald sums. I. A theoretical and numerical comparison of various particle mesh routines," *Journal of Chemical Physics*, vol. 109, no. 18, pp. 7678–7693, 1998.

[83] R. Borg and G. Dienes, *The physical chemistry of solids*. San Diego: Academic Press, 1992.

[84] T. Ohwaki, K. Kamegai, and K. Yamashita, "Electric field effects on the adsorption, charge transfer and vibrational state at metal electrodes: A DFT study on H_2O/Pt(111), H_2O/Pt(100) and $(H_2O)_2$/Pt(111)," *The Chemical Society of Japan*, vol. 74, pp. 1021–1029, 2001.

[85] C. G. Sanchez, "Molecular reorientation of water adsorbed on charged Ag(111) surfaces," *Surface Science*, vol. 527, pp. 1–11, 2003.

[86] Tapani A. Pakkanen. Private communication, 2004.

[87] R. Ludwig, "How does water bind to metal surfaces: hydrogen atoms up or hydrogen atoms down?," *Angewandte Chemie-International Edition*, vol. 42, no. 30, pp. 3458–3460, 2003.

[88] T. Moffat, D. Wheeler, M. Edelstein, and D. Josell, "Superconformal film growth: Mechanism and quantification," *IBM Journal of Research and Development*, vol. 49, no. 1, pp. 19–36, 2005.

[89] A. C. West, "Theory of filling of high-aspect ratio trenches and vias in presence of additives," *Journal of The Electrochemical Society*, vol. 147, no. 1, pp. 227–232, 2000.

[90] P. Andricacos, C. Uzoh, J. Dukovic, J. Horkans, and H. Deligianni, "Damascene copper electroplating for chip interconnections," *IBM Journal of Research and Development*, vol. 42, no. 5, p. 567, 1998.

[91] T. Moffat, D. Wheeler, and D. Josell, "Electrodeposition of copper in the SPS-PEG-Cl additive system," *Journal of The Electrochemical Society*, vol. 151, no. 4, pp. C262–C271, 2004.

[92] M. Tan, *An Experimental Study of the Behavior of Additives (Cl^-, PEG, and SPS) During Acidic Copper Electrodeposition.* PhD thesis, Brigham Young University, 2004.

[93] E. Spohr, "Some recent trends in computer simulations of aqueous double layers," *Electrochimica Acta*, vol. 49, no. 1, pp. 23–27, 2003.

[94] F. Grun, M. Jardat, P. Turq, and C. Amatore, "Relaxation of the electrical double layer after an electron transfer approached by Brownian dynamics simulation," *Journal of Chemical Physics*, vol. 120, no. 20, pp. 9648–9655, 2004.

[95] M. Deserno and C. Holm, "How to mesh up Ewald sums. II. An accurate error estimate for the particle-particle-particle-mesh algorithm," *Journal of Chemical Physics*, vol. 109, no. 18, pp. 7694–7701, 1998.

[96] D. Chandler, *Introduction to Modern Statistical Mechanics.* Oxford University Press, 1987.

[97] B. Roux, "The calculation of the potential of mean force using computer simulations," *Computer Physics Communications*, vol. 91, pp. 275–282, 1995.

[98] G. Henkelman, B. Uberuaga, and H. Jonsson, "A climbing image nudged elastic band method for finding saddle points and minimum energy paths," *Journal of Chemical Physics*, vol. 113, p. 9901, 2000.

[99] T. Ang, T. Wee, and W. Chin, "Three-dimensional self-assembled monolayer (3D SAM) of *n*-alkanethiols on copper nanoclusters," *Journal of Physical Chemistry B*, vol. 108, no. 30, pp. 11001–11010, 2004.

[100] C. Bain, E. Troughton, Y.-T. Tao, J. Evall, G. Whitesides, and R. Nuzzo, "Formation of monolayer films by the spontaneous assembly of organic thiols from solution onto gold," *Journal of the American Chemical Society*, vol. 111, pp. 321–335, 1989.

[101] J. O. Bockris and S. Khan, *Surface electrochemistry*. Plenum Press, 1993.

[102] A. B. Anderson and T. V. Albu, "Ab initio determination of reversible potentials and activation energies for outer-sphere oxygen reduction to water and the reverse oxidation reaction," *Journal of the American Chemical Society*, vol. 121, pp. 11855–11863, 1999.

[103] J. Healy, D. Pletcher, and M. Goodenough, "The chemistry of the additives in an acid copper electroplating bath. Part III. the mechanism of brightening by 4,5-dithiaoctane-1,8-disulphonic acid," *Journal of Electroanalytical Chemistry*, vol. 338, no. 1–2, pp. 179–187, 1992.

[104] J. Kim, S.-K. Kim, and Y. Kim, "Catalytic behavior of 3-mercapto-1-propane sulfonic acid on Cu electrodeposition and its effect on Cu film properties for CMOS device metallization," *Journal of Electroanalytical Chemistry*, vol. 542, pp. 61–66, 2003.

[105] T. Moffat and H. Yang, "Patterned metal electrodeposition using an alkanethiolate mask," *Journal of The Electrochemical Society*, vol. 142, no. 11, p. L220, 1995.

[106] E. D. Eliadis, R. G. Nuzzo, A. A. Gewirth, and R. C. Alkire, "Copper deposition in the presence of surface-confined additives," *Journal of the Electrochemical Society*, vol. 144, no. 1, pp. 96–105, 1997.

[107] J. White and H. Abruna, "Influence of competing adsorbates on the underpotential deposition of copper on Pt(111)," *Journal of Electroanalytical Chemistry and Interfacial Electrochemistry*, vol. 300, no. 1–2, pp. 521–542, 1991.

[108] H. Hagenstrom, M. Esplandiu, and D. Kolb, "Functionalized self-assemble alkanethiol monolayers on Au(111) electrodes: 2. Silver electrodeposition," *Langmuir*, vol. 17, no. 3, pp. 839–848, 2001.

[109] M. Nishizawa, T. Sunagawa, and H. Yoneyama, "Underpotential deposition of copper on gold electrodes through self-assembled monolayers of propanethiol," *Langmuir*, vol. 13, no. 20, pp. 5215–5217, 1997.

[110] W. Deng, D. Fujita, L. Yang, H. Nejo, and C. Bai, "Multilayer formation of copper ions(Cu^{2+}) deposited onto self-assembled monolayers of alkanedithiols on Au(111) surfaces," *Japanese Journal of Applied Physics*, vol. 39, pp. L751–L754, 2000.

[111] D. Stoychev and P. Stefanov, "Sulfide formation in electrodeposition of bright copper coatings in the presence of sulfur-containing brighteners," *Russian Journal of Electrochemistry*, vol. 30, no. 3, pp. 349–352, 1994.

[112] M. Goodenough and K. Whitlaw, "Studies of copper deposition for high aspect ratio printed-circuit boards," *Transactions of the Institute of Metal Finishing*, vol. 67, pp. 57–62, 1989.

[113] M. Peykova, E. Michailova, D. Stoychev, and A. Milchev, "Galvanostatic studies of the nucleation and growth-kinetics of copper in the presence of surfactants," *Electrochimica Acta*, vol. 40, no. 16, pp. 2595–2601, 1995.

[114] J. J. Kelly, C. Tian, and A. C. West, "Leveling and microstructural effects of additives for copper electrodeposition," *Journal of The Electrochemical Society*, vol. 146, no. 7, pp. 2540–2545, 1999.

[115] Z. Nagy, J. Blaudeau, N. Hung, L. Curtiss, and D. Zurawski, "Chloride ion catalysis of the copper deposition reaction," *Journal of the Electrochemical Society*, vol. 142, no. 6, pp. L87–L89, 1995.

[116] L. Cheng, P. Fenter, K. Nagy, M. Schlegel, and N. Sturchio, "Molecular-Scale density oscillations in water adjacent to a mica surface," *Physical Review Letters*, vol. 87, no. 15, p. 156103, 2001.

[117] N. Zukauskaite and A. Malinauskas, "Electrocatalysis by a brightener in copper electrodeposition," *Soviet electrochemistry*, vol. 24, no. 12, pp. 1564–1566, 1988.

[118] D. Simkunaite and A. Steponavicius, "Chronopotentiometric investigation of acidic $CuSO_4$ solution containing accelerating additive - DDDS," *Chemija*, vol. 3, pp. 42–49, 1996.

[119] E. Carter, G. Ciccotti, J. Hynes, and R. Kapral, "Constrained reaction coordinate dynamics for the simulation of rare events," *Chemical Physics Letters*, vol. 156, no. 5, pp. 472–477, 1989.

Appendix A

Example Ewald Calculation

The following pages are a reproduction of a Mathcad worksheet using the Ewald sum to calculate the interaction energy of a water molecule with an ECD model of a copper surface. The system is periodically repeated. The results of the calculation are plotted in Figs. 5.5, 5.6, and 5.7.

Mathcad Implementation of Ewald Method for charge equilibration model of periodic (111) fcc copper slab next to test particles

$ORIGIN := 1$

unit cell size in Angstroms $a0 := 3.61496$ $volt := 14.4$ volt.Angstrom/e

vacuum gap in Angstroms $gap := 18$ $F := 96.485$ kJ/mol/eV

number of electrode layers $NL := 2$

voltage diff between electrode halves $\Delta V := 0.$

core charges in |e| $qc := 1$

valence-charge inverse widths $\gamma := 0.816$ $\gamma ij := \gamma \cdot 2^{-0.5}$

Ewald parameters $\alpha := 0.9 \cdot \gamma ij$ $rcut := \frac{3.5}{\alpha}$

$hcut := 10 \cdot \alpha$ $rcut = 6.74$

Total number of Cu atoms $NP := NL \cdot 4$

vectorize core charges $i := 1 .. NP$ $qcvec_i := qc$

Total charge on cell copper atoms in |e| $totQ := 0$

function to generate positions of periodic layers of Cu atoms

$$R := \left| \begin{array}{l} \text{for } i \in 1 .. NP \\ \quad z \leftarrow \dfrac{-\text{floor}\left(\dfrac{i-1}{4}\right) + \text{floor}\left(\dfrac{NP-1}{4}\right)}{\sqrt{3}} \\ \quad pos^{\langle i \rangle} \leftarrow \begin{pmatrix} 0 \\ 0 \\ z \end{pmatrix} \cdot a0 \text{ if } \text{mod}(i,4) = 1 \\ \quad pos^{\langle i \rangle} \leftarrow \begin{pmatrix} \frac{1}{\sqrt{2}} \\ 0 \\ z \end{pmatrix} \cdot a0 \text{ if } \text{mod}(i,4) = 2 \\ \quad pos^{\langle i \rangle} \leftarrow \begin{pmatrix} \frac{1}{\sqrt{8}} \\ \sqrt{\frac{3}{8}} \\ z \end{pmatrix} \cdot a0 \text{ if } \text{mod}(i,4) = 3 \\ \quad pos^{\langle i \rangle} \leftarrow \begin{pmatrix} \sqrt{\frac{9}{8}} \\ \sqrt{\frac{3}{8}} \\ z \end{pmatrix} \cdot a0 \text{ if } \text{mod}(i,4) = 0 \\ \quad pos^{\langle i \rangle} \leftarrow pos^{\langle i \rangle} + \begin{pmatrix} \frac{1}{\sqrt{8}} \cdot \text{mod}\left(\text{floor}\left(\frac{i-1}{4}\right), 3\right) \\ \frac{1}{\sqrt{24}} \cdot \text{mod}\left(\text{floor}\left(\frac{i-1}{4}\right), 3\right) \\ 0 \end{pmatrix} \cdot a0 \\ pos \end{array} \right.$$

positions and charges of SPC/E water

$$qT := \begin{pmatrix} -0.8476 \\ 0.4238 \\ 0.4238 \end{pmatrix}$$

number of test particles $NT := 3$

$dhh := 1.633$ $dohh := 0.577$

Initial unrotated site positions

O H1 H2

$$Rsite := \begin{pmatrix} 0 & 0 & 0 \\ 0 & 0.5 \cdot dhh & -0.5 \cdot dhh \\ 0 & dohh & dohh \end{pmatrix}$$

define m routes by rotation and position of water relative to copper cluster

$$r_{top} := \begin{pmatrix} 0 \\ 0 \\ 0 \end{pmatrix} \cdot a0 \qquad r_{bridge} := \begin{pmatrix} \frac{1}{\sqrt{32}} \\ \sqrt{\frac{3}{32}} \\ 0 \end{pmatrix} \cdot a0 \qquad r_{hollow} := \begin{pmatrix} \frac{1}{\sqrt{8}} \\ \frac{1}{\sqrt{24}} \\ 0 \end{pmatrix} \cdot a0$$

$$Rbase(m) := \left| \begin{array}{l} ch \leftarrow floor\left(\frac{m-1}{3}\right) \\ r_{top} \text{ if } ch = 0 \\ r_{bridge} \text{ if } ch = 1 \\ r_{hollow} \text{ otherwise} \end{array} \right.$$

set rotation of water for m routes:

$$\theta(m) := \left| \begin{array}{l} ch \leftarrow mod(m-1, 3) \\ 0 \cdot deg \text{ if } ch = 0 \\ 180 \cdot deg \text{ if } ch = 1 \\ 90 \cdot deg \text{ otherwise} \end{array} \right. \qquad \phi(m) := \left| \begin{array}{l} 22.8 \cdot deg \text{ if } m = 3 \\ 240 \cdot deg \text{ if } m = 6 \\ 30 \cdot deg \text{ if } m = 8 \\ 202.8 \cdot deg \text{ if } m = 9 \\ 60 \cdot deg \text{ otherwise} \end{array} \right. \qquad \chi(m) := 0 \cdot deg$$

asimuthal transformation matrix

$$rotate(\theta, \phi, \chi) := \begin{pmatrix} \cos(\phi)\cdot\cos(\theta)\cdot\cos(\chi) - \sin(\phi)\cdot\sin(\chi) & -\cos(\phi)\cdot\cos(\theta)\sin(\chi) - \sin(\phi)\cdot\cos(\chi) & \cos(\phi)\cdot\sin(\theta) \\ \sin(\phi)\cdot\cos(\theta)\cdot\cos(\chi) + \cos(\phi)\cdot\sin(\chi) & -\sin(\phi)\cdot\cos(\theta)\cdot\sin(\chi) + \cos(\phi)\cdot\cos(\chi) & \sin(\phi)\cdot\sin(\theta) \\ -\sin(\theta)\cdot\cos(\chi) & \sin(\theta)\cdot\sin(\chi) & \cos(\theta) \end{pmatrix}$$

Function to locate water sites given z position of oxygen and route index

$$RT(zt, m) := rotate(\theta(m), \phi(m), \chi(m)) \cdot Rsite + \left[\begin{pmatrix} R_{1,4} \\ R_{2,4} \\ R_{3,4} + zt \end{pmatrix} + Rbase(m) \right] \cdot (1 \quad 1 \quad 1)$$

$$Rview := augment(R, RT(2,1))^T$$

Side view

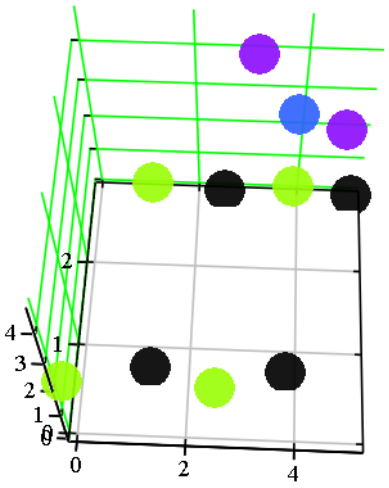

Top view

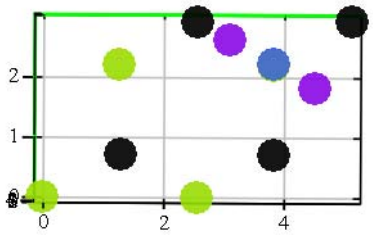

$\left(\text{Rview}^{\langle 1\rangle}, \text{Rview}^{\langle 2\rangle}, \text{Rview}^{\langle 3\rangle}\right)$

$\left(\text{Rview}^{\langle 1\rangle}, \text{Rview}^{\langle 2\rangle}, \text{Rview}^{\langle 3\rangle}\right)$

cell basis matrix: each column is (x,y,z) of unit-cell basis vector

$$H := \begin{pmatrix} \sqrt{2} & \frac{1}{\sqrt{2}} & 0 \\ 0 & \sqrt{\frac{3}{2}} & 0 \\ 0 & 0 & \frac{NL-1}{\sqrt{3}} + \frac{gap}{a0} \end{pmatrix} \cdot a0$$

$$H = \begin{pmatrix} 5.112 & 2.556 & 0 \\ 0 & 4.427 & 0 \\ 0 & 0 & 20.087 \end{pmatrix}$$

Calc minimum number of unit cells required to adequately cover rcut

$$\text{minr}(\text{ncells}) := \left| \begin{array}{l} \text{minr2} \leftarrow 1000 \\ \text{for } n \in -\text{ncells}..\text{ncells} \\ \quad \left| \begin{array}{l} \text{r2n} \leftarrow \begin{pmatrix} n \\ \text{ncells} \\ 0 \end{pmatrix} \cdot \left[H^{T} \cdot H \cdot \begin{pmatrix} n \\ \text{ncells} \\ 0 \end{pmatrix} \right] \\ \text{minr2} \leftarrow \text{r2n} \quad \text{if} \quad \text{r2n} < \text{minr2} \\ \text{r2n} \leftarrow \begin{pmatrix} \text{ncells} \\ n \\ 0 \end{pmatrix} \cdot \left[H^{T} \cdot H \cdot \begin{pmatrix} \text{ncells} \\ n \\ 0 \end{pmatrix} \right] \\ \text{minr2} \leftarrow \text{r2n} \quad \text{if} \quad \text{r2n} < \text{minr2} \end{array} \right. \\ \sqrt{\text{minr2}} \end{array} \right.$$

$$\text{ncells} := \left| \begin{array}{l} n \leftarrow 0 \\ \text{while} \quad \text{minr}(n) < \text{rcut} \\ \quad n \leftarrow n + 1 \\ n \end{array} \right.$$

$\text{ncells} = 2$

Real-Space Energy and C matrices,

including γ self terms and correction

$$\text{Ureal}(qvh, zt, m) :=$$

$Rtest \leftarrow RT(zt, m)$

$U \leftarrow 2 \cdot \left(\frac{\gamma ij}{\sqrt{\pi}} \cdot qvh \cdot qvh + \frac{2 \cdot \gamma}{\sqrt{\pi}} \cdot qc \cdot \sum qvh \right)$

$qt \leftarrow qvh + qc$

for $i \in 1 .. NP$

  for $j \in 1 .. NP$

    $\Delta R \leftarrow R^{\langle i \rangle} - R^{\langle j \rangle}$

    for $n1 \in -ncells .. ncells$

      for $n2 \in -ncells .. ncells$

        for $n3 \in -1 .. 1$

          $Rijn \leftarrow \left| \Delta R - H \cdot \begin{pmatrix} n1 \\ n2 \\ n3 \end{pmatrix} \right|$

          $U \leftarrow U + \frac{qc \cdot qc}{Rijn} - \frac{qt_i \cdot qt_j \cdot \text{erf}(\alpha \cdot Rijn)}{Rijn} \ldots + qvh_i \cdot \left(\frac{qvh_j \cdot \text{erf}(\gamma ij \cdot Rijn)}{Rijn} + 2 \cdot \frac{qc \cdot \text{erf}(\gamma \cdot Rijn)}{Rijn} \right)$ if $Rijn < rcut \wedge Rijn > 0$

  for $j \in 1 .. NT$

    $\Delta R \leftarrow R^{\langle i \rangle} - Rtest^{\langle j \rangle}$

    for $n1 \in -ncells .. ncells$

      for $n2 \in -ncells .. ncells$

        for $n3 \in -1 .. 1$

          $Rijn \leftarrow \left| \Delta R - H \cdot \begin{pmatrix} n1 \\ n2 \\ n3 \end{pmatrix} \right|$

          $U \leftarrow U + 2 \cdot \left(\frac{qc \cdot qT_j}{Rijn} - \frac{qt_i \cdot qT_j \cdot \text{erf}(\alpha \cdot Rijn)}{Rijn} + \frac{qvh_i \cdot qT_j \cdot \text{erf}(\gamma \cdot Rijn)}{Rijn} \right)$ if $Rijn < rcut$

for $i \in 1 .. NT$

  for $j \in 1 .. NT$

    $\Delta R \leftarrow Rtest^{\langle i \rangle} - Rtest^{\langle j \rangle}$

    for $n1 \in -ncells .. ncells$

      for $n2 \in -ncells .. ncells$

        for $n3 \in -1 .. 1$

          $Rijn \leftarrow \left| \Delta R - H \cdot \begin{pmatrix} n1 \\ n2 \\ n3 \end{pmatrix} \right|$

          $U \leftarrow U + \frac{qT_i \cdot qT_j \cdot \text{erfc}(\alpha \cdot Rijn)}{Rijn}$ if $Rijn < rcut \wedge Rijn > 0$

$\frac{U}{2} \cdot volt \cdot F$

$$\text{Creal} := \left| \begin{array}{l} \text{for } i \in 1 .. NP \\ \quad \text{for } j \in 1 .. NP \\ \quad\quad C_{i,j} \leftarrow \frac{2 \cdot \gamma ij}{\sqrt{\pi}} \cdot \delta(i,j) \\ \quad\quad \text{for } n1 \in -ncells .. ncells \\ \quad\quad\quad \text{for } n2 \in -ncells .. ncells \\ \quad\quad\quad\quad \text{for } n3 \in -1 .. 1 \\ \quad\quad\quad\quad\quad Rijn \leftarrow \left| R^{\langle i \rangle} - R^{\langle j \rangle} - H \cdot \begin{pmatrix} n1 \\ n2 \\ n3 \end{pmatrix} \right| \\ \quad\quad\quad\quad\quad C_{i,j} \leftarrow C_{i,j} + \frac{\text{erf}(\gamma ij \cdot Rijn)}{Rijn} - \frac{\text{erf}(\alpha \cdot Rijn)}{Rijn} \quad \text{if } Rijn < rcut \wedge Rijn > 0 \\ C \end{array} \right.$$

$$\text{C'real} := \left| \begin{array}{l} \text{for } i \in 1 .. NP \\ \quad \text{for } j \in 1 .. NP \\ \quad\quad C'_{i,j} \leftarrow \frac{2 \cdot \gamma}{\sqrt{\pi}} \cdot \delta(i,j) \\ \quad\quad \text{for } n1 \in -ncells .. ncells \\ \quad\quad\quad \text{for } n2 \in -ncells .. ncells \\ \quad\quad\quad\quad \text{for } n3 \in -1 .. 1 \\ \quad\quad\quad\quad\quad Rijn \leftarrow \left| R^{\langle i \rangle} - R^{\langle j \rangle} - H \cdot \begin{pmatrix} n1 \\ n2 \\ n3 \end{pmatrix} \right| \\ \quad\quad\quad\quad\quad C'_{i,j} \leftarrow C'_{i,j} + \frac{\text{erf}(\gamma \cdot Rijn)}{Rijn} - \frac{\text{erf}(\alpha \cdot Rijn)}{Rijn} \quad \text{if } Rijn < rcut \wedge Rijn > 0 \\ C' \end{array} \right.$$

$$\phi\text{xreal}(zt, m) := \left| \begin{array}{l} Rtest \leftarrow RT(zt, m) \\ \text{for } i \in 1 .. NP \\ \quad \phi x_i \leftarrow 0 \\ \quad \text{for } j \in 1 .. NT \\ \quad\quad \text{for } n1 \in -ncells .. ncells \\ \quad\quad\quad \text{for } n2 \in -ncells .. ncells \\ \quad\quad\quad\quad \text{for } n3 \in -1 .. 1 \\ \quad\quad\quad\quad\quad Rijn \leftarrow \left| R^{\langle i \rangle} - Rtest^{\langle j \rangle} - H \cdot \begin{pmatrix} n1 \\ n2 \\ n3 \end{pmatrix} \right| \\ \quad\quad\quad\quad\quad \phi x_i \leftarrow \phi x_i + \frac{qT_j \cdot (\text{erf}(\gamma \cdot Rijn) - \text{erf}(\alpha \cdot Rijn))}{Rijn} \quad \text{if } Rijn < rcut \wedge Rijn > 0 \\ \phi x \end{array} \right.$$

$$\phi\text{real}(qvh) := (\text{Creal} \cdot qvh + \text{C'real} \cdot qcvec) \cdot volt$$

vdW energy (kJ/mol)

$$cfe := \begin{pmatrix} 5 & 0.843 & 0.843 \\ 1.35 & 1.303 & 1.303 \\ 2.89 & 3.302 & 3.302 \end{pmatrix}$$

```
UvdW(zt, m) := | Rtest ← RT(zt, m)
               | U ← 0
               | for i ∈ 1 .. NP
               |   for j ∈ 1 .. NT
               |     ΔR ← R^⟨i⟩ − Rtest^⟨j⟩
               |     for n1 ∈ −(ncells + 2) .. (ncells + 2)
               |       for n2 ∈ −(ncells + 2) .. (ncells + 2)
               |         for n3 ∈ −1 .. 1
               |           Rijn ← |ΔR − H · (n1, n2, n3)ᵀ|
               |           U ← U − cfe_{1,j} · [1 − [1 − exp[−cfe_{2,j} · (Rijn − cfe_{3,j})]]]^2  if Rijn < rcut
               | U
```

functions that determine recip-lattice-sum bounds

$$Lz := H_{3,3} \qquad nzup := \mathrm{floor}\left(hcut \cdot \frac{Lz}{2 \cdot \pi}\right)$$

$$nLxy2(nmax) := \begin{pmatrix} nmax \\ 0 \\ 0 \end{pmatrix} \cdot \left[H^{-1}{}^{T} \cdot H^{-1} \cdot \begin{pmatrix} nmax \\ 0 \\ 0 \end{pmatrix} \right]$$

$$nz1 := 1 .. nzup + 1$$

$$nmax := 1$$

$$maxn_{nz1} := \mathrm{ceil}\left[\mathrm{root}\left[\left(\frac{hcut}{2 \cdot \pi}\right)^2 - \left(\frac{nz1 - 1}{Lz}\right)^2 - nLxy2(nmax), nmax \right] \right]$$

$$nup(nz) := maxn_{nz+1}$$

$$n2lowr(nz) := \mathrm{if}\left(nz = 0, 0, -maxn_{nz+1}\right)$$

$$n1lowr(nz, n2) := \mathrm{if}\left(nz = 0 \wedge n2 = 0, 1, -maxn_{nz+1}\right)$$

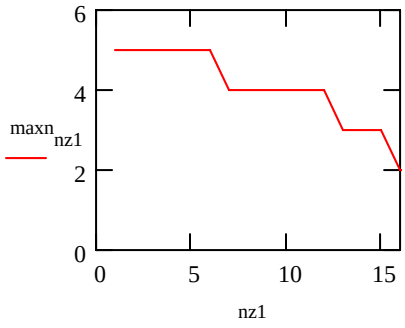

Reciprocal-space Energy and C matrices including α self terms

$$\text{Urecip}(qvh, zt, m) :=$$

$Rt \leftarrow RT(zt, m)$

$qt \leftarrow qvh + qc$

$cell \leftarrow 2\cdot\pi\cdot i\cdot H^{-1}$

$H2 \leftarrow \left(\frac{\pi}{\alpha}\right)^2 \cdot H^{-1}{}^{T} \cdot H^{-1}$

$b2cut \leftarrow \left(\frac{hcut}{2\cdot\alpha}\right)^2$

$U \leftarrow -\frac{\alpha}{\sqrt{\pi}}\cdot(qt\cdot qt + qT\cdot qT)$

$C1 \leftarrow \frac{\pi}{|H|\cdot\alpha^2}$

for $nz \in 0 .. nzup$

  for $n2 \in n2lowr(nz) .. nup(nz)$

    for $n1 \in n1lowr(nz, n2) .. nup(nz)$

      $nvec \leftarrow \begin{pmatrix} n1 \\ n2 \\ nz \end{pmatrix}$

      $b2 \leftarrow nvec\cdot(H2\cdot nvec)$

      if $b2 < b2cut$

        $hi \leftarrow cell\cdot nvec$

        $S \leftarrow \sum_{i=1}^{NP} \left(qt_i \cdot \exp\left(hi\cdot R^{\langle i \rangle}\right)\right) + \sum_{i=1}^{NT} \left(qT_i \cdot \exp\left(hi\cdot Rt^{\langle i \rangle}\right)\right)$

        $U \leftarrow U + C1\cdot\frac{\exp(-b2)}{b2}\cdot S\cdot\overline{S}$

$U\cdot volt\cdot F$

Crecip :=

cell ← $2\cdot\pi\cdot i\cdot H^{-1}$

H2 ← $\left(\frac{\pi}{\alpha}\right)^{2}\cdot H^{-1^{T}}\cdot H^{-1}$

b2cut ← $\left(\frac{hcut}{2\cdot\alpha}\right)^{2}$

C1 ← $\frac{\pi}{|H|\cdot\alpha^{2}}$

for i ∈ 1 .. NP

  for j ∈ 1 .. NP

    $C_{i,j}$ ← $\frac{-2\cdot\alpha}{\sqrt{\pi}}\cdot\delta(i,j)$

for nz ∈ 0 .. nzup

  for n2 ∈ n2lowr(nz) .. nup(nz)

    for n1 ∈ n1lowr(nz, n2) .. nup(nz)

      nvec ← $\begin{pmatrix} n1 \\ n2 \\ nz \end{pmatrix}$

      b2 ← nvec·(H2·nvec)

      if b2 < b2cut

        hi ← cell·nvec

        dSdq ← $\exp\left(R^{T}\cdot hi\right)$

        C ← C + C1·$\frac{\exp(-b2)}{b2}\cdot 2\cdot Re\left(dSdq\cdot\left(\overline{dSdq}\right)^{T}\right)$

C

$\phi xrecip(zt, m) :=$

$Rt \leftarrow RT(zt, m)$

$cell \leftarrow 2 \cdot \pi \cdot i \cdot H^{-1}$

$H2 \leftarrow \left(\frac{\pi}{\alpha}\right)^2 \cdot H^{-1^T} \cdot H^{-1}$

$b2cut \leftarrow \left(\frac{hcut}{2 \cdot \alpha}\right)^2$

$C1 \leftarrow \frac{\pi}{|H| \cdot \alpha^2}$

for $i \in 1 .. NP$

$\phi x_i \leftarrow 0$

for $nz \in 0 .. nzup$

for $n2 \in n2lowr(nz) .. nup(nz)$

for $n1 \in n1lowr(nz, n2) .. nup(nz)$

$nvec \leftarrow \begin{pmatrix} n1 \\ n2 \\ nz \end{pmatrix}$

$b2 \leftarrow nvec \cdot (H2 \cdot nvec)$

if $b2 < b2cut$

$hi \leftarrow cell \cdot nvec$

$S \leftarrow \sum_{i=1}^{NT} \left(qT_i \cdot \exp\left(hi \cdot Rt^{\langle i \rangle}\right)\right)$

$dSdq \leftarrow \exp\left(R^T \cdot hi\right)$

$\phi x \leftarrow \phi x + C1 \cdot \frac{\exp(-b2)}{b2} \cdot 2 \cdot Re\left(dSdq \cdot \bar{S}\right)$

ϕx

$\phi recip(qvh) := Crecip \cdot (qvh + qc) \cdot volt$ $\phi ext(zt, m) := (\phi xreal(zt, m) + \phi xrecip(zt, m)) \cdot volt$

Charge equilibration solution to valence charges

$C := Creal + Crecip$ $Cstar := C'real + Crecip$ $uc(z) := 1 - \Phi(z)$

$Dmat(qvh) :=$

$ns \leftarrow \sum_i uc\left(qvh_i\right)$

for $j \in 1 .. NP$

$c_j \leftarrow \frac{1}{ns} \cdot \sum_i \left(uc\left(qvh_i\right) \cdot C_{i,j}\right)$

for $i \in 1 .. NP$

for $j \in 1 .. NP$

$D_{i,j} \leftarrow uc\left(qvh_i\right) \cdot \left(C_{i,j} - c_j + 1 - \delta(i,j)\right) + \delta(i,j)$

D

$$\text{Dstar}(qvh) := \left| \begin{array}{l} ns \leftarrow \sum_i uc(qvh_i) \\ \text{for } j \in 1..NP \\ \quad c'_j \leftarrow \frac{1}{ns} \cdot \sum_i \left(uc(qvh_i) \cdot Cstar_{i,j} \right) \\ \text{for } i \in 1..NP \\ \quad \text{for } j \in 1..NP \\ \quad\quad D'_{i,j} \leftarrow uc(qvh_i) \cdot \left(Cstar_{i,j} - c'_j + 1 \right) \\ D' \end{array} \right.$$

$$g(qvh, zt, m) := \left| \begin{array}{l} \phi x \leftarrow \phi ext(zt, m) \\ \text{for } j \in 1..NP \\ \quad offset_j \leftarrow \begin{cases} 0.5 \cdot \Delta V & \text{if } j = \frac{NP+1}{2} \\ \Delta V \cdot floor\left(\frac{2 \cdot j - 1}{NP} \right) & \text{otherwise} \end{cases} \\ ns \leftarrow \sum_i uc(qvh_i) \\ f1 \leftarrow \frac{1}{ns} \cdot \sum_i \left(uc(qvh_i) \cdot offset_i \right) \\ f2 \leftarrow \frac{1}{ns} \cdot \sum_i \left(uc(qvh_i) \cdot \phi x_i \right) \\ \text{for } j \in 1..NP \\ \quad gg_j \leftarrow uc(qvh_j) \cdot \left(f1 - offset_j + f2 - \phi x_j + totQ \cdot volt \right) \\ \frac{gg}{volt} \end{array} \right.$$

$$qv(zt, m) := \left| \begin{array}{l} \text{for } j \in 1..NP \\ \quad qv1_j \leftarrow -1 \\ ntight \leftarrow 0 \\ \delta ntight \leftarrow 1 \\ \text{while } \delta ntight > 0 \\ \quad \left| \begin{array}{l} qv1 \leftarrow Dmat(qv1)^{-1} \cdot (g(qv1, zt, m) - Dstar(qv1) \cdot qcvec) \\ \delta ntight \leftarrow NP - \sum_{j=1}^{NP} uc(qv1_j) - ntight \\ ntight \leftarrow ntight + \delta ntight \end{array} \right. \\ qv1 \end{array} \right.$$

Solution for the isolated cluster

$$\text{giso}(qvh) := \left| \begin{array}{l} \text{for } j \in 1 .. NP \\ \quad \text{offset}_j \leftarrow \begin{cases} 0.5 \cdot \Delta V & \text{if } j = \dfrac{NP+1}{2} \\ \Delta V \cdot \text{floor}\left(\dfrac{2 \cdot j - 1}{NP}\right) & \text{otherwise} \end{cases} \\ ns \leftarrow \sum_i uc\left(qvh_i\right) \\ f \leftarrow \dfrac{1}{ns} \cdot \sum_i \left(uc\left(qvh_i\right) \cdot \text{offset}_i\right) \\ \text{for } j \in 1 .. NP \\ \quad gg_j \leftarrow uc\left(qvh_j\right) \cdot \left(f - \text{offset}_j + totQ \cdot volt\right) \\ \dfrac{gg}{volt} \end{array} \right.$$

$$\text{qviso} := \left| \begin{array}{l} \text{for } j \in 1 .. NP \\ \quad qv1_j \leftarrow -1 \\ ntight \leftarrow 0 \\ \delta ntight \leftarrow 1 \\ \text{while } \delta ntight > 0 \\ \quad \left| \begin{array}{l} qv1 \leftarrow Dmat(qv1)^{-1} \cdot (\text{giso}(qv1) - Dstar(qv1) \cdot qcvec) \\ \delta ntight \leftarrow NP - \sum_{j=1}^{NP} uc\left(qv1_j\right) - ntight \\ ntight \leftarrow ntight + \delta ntight \end{array} \right. \\ qv1 \end{array} \right.$$

plot solution to layer charges (per atom) and voltages

Route

$qiso := qviso + qc$ $\quad qtot(zt, m) := qv(zt, m) + qc$ $\quad z := \left(R^T\right)^{\langle 3 \rangle}$ $\quad zs := 2$ $\quad m := 1$

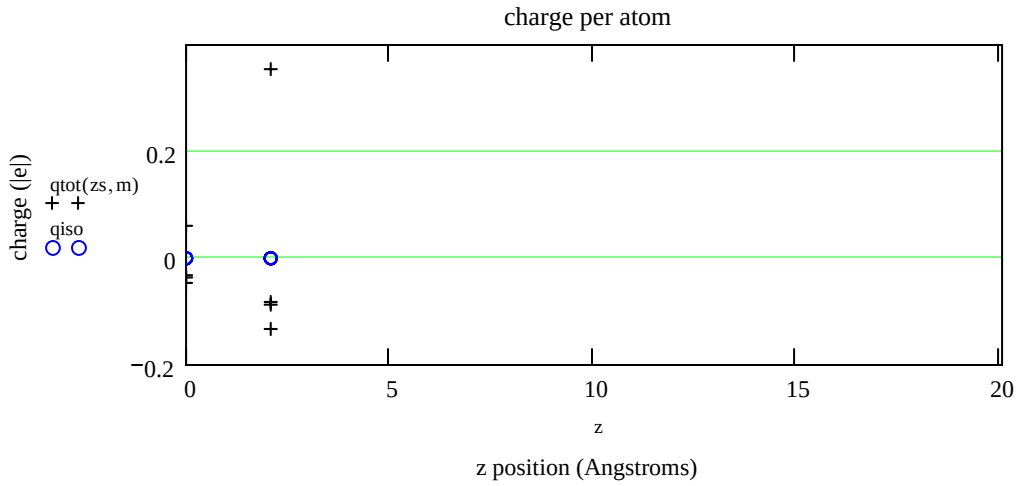

Electrostatic potential (volt)

$\phi tot(qvh, zt, m) := \phi real(qvh) + \phi recip(qvh) + \phi ext(zt, m)$

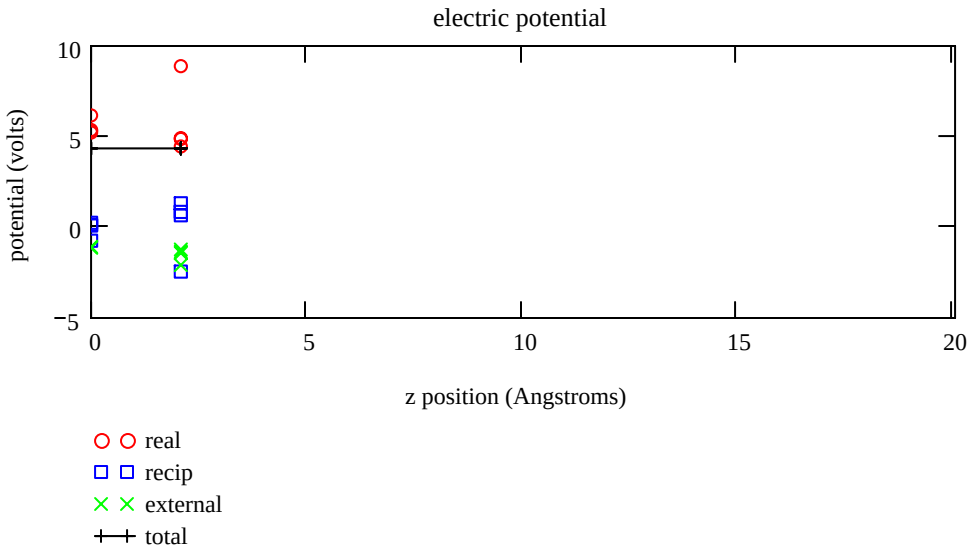

Total Coulombic plus vdW energy (kJ/mol)

nroutes := 9 im := 1 .. nroutes

$$U_{zero_{im}} := \left| \begin{array}{l} qvh \leftarrow qv\left(\frac{gap}{2}, im\right) \\ Urecip\left(qvh, \frac{gap}{2}, im\right) + Ureal\left(qvh, \frac{gap}{2}, im\right) + UvdW\left(\frac{gap}{2}, im\right) \end{array} \right.$$

Utot(qvh, zt, m) := Urecip(qvh, zt, m) + Ureal(qvh, zt, m) + UvdW(zt, m)

nofp := 30 np := 1 .. nofp

$$Utot(qv(zs, m), zs, m) - U_{zero_m} = -53.166$$

$$zt := \left| \begin{array}{l} out_1 \leftarrow 1.1 \\ prefc \leftarrow \frac{\frac{gap}{2} - out_1}{\sum_{j=2}^{nofp} j^2} \\ \text{for } i \in 2 .. nofp \\ \quad out_i \leftarrow out_{i-1} + prefc \cdot i^2 \\ out \end{array} \right.$$

$$U_{np,im} := Utot\left(qv\left(zt_{np}, im\right), zt_{np}, im\right) - U_{zero_{im}}$$

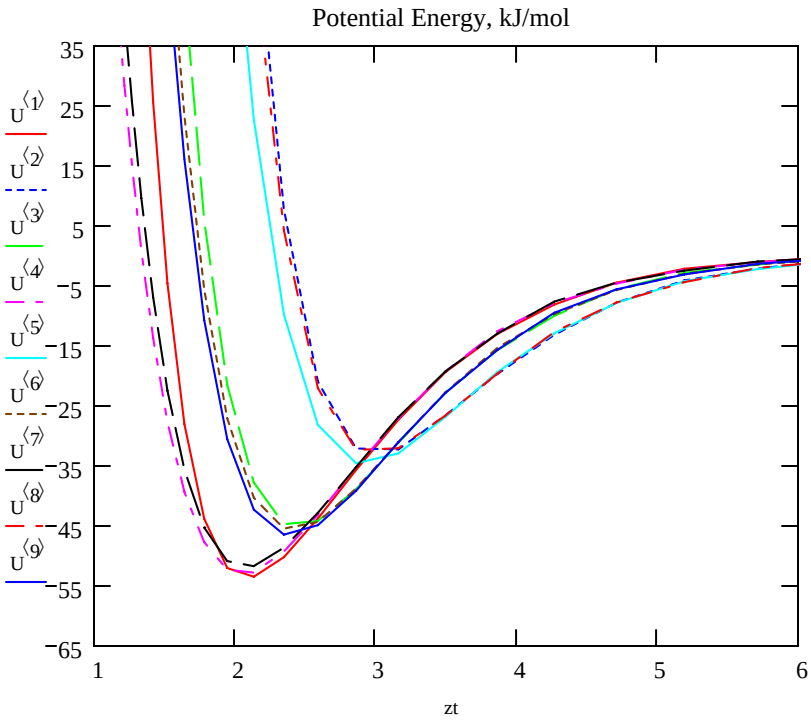

Routes are as follows

1	top - hup
2	top - hdwn
3	top - hpl
4	bridge - hup
5	bridge - hdwn
6	bridge - hpl
7	hollow - hup
8	hollow - hdwn
9	hollow - hpl